TUM School of Natural Sciences

Anharmonic Dynamics and Their Influence on the Optoelectronic Properties of Halide Perovskites

Xiangzhou Zhu

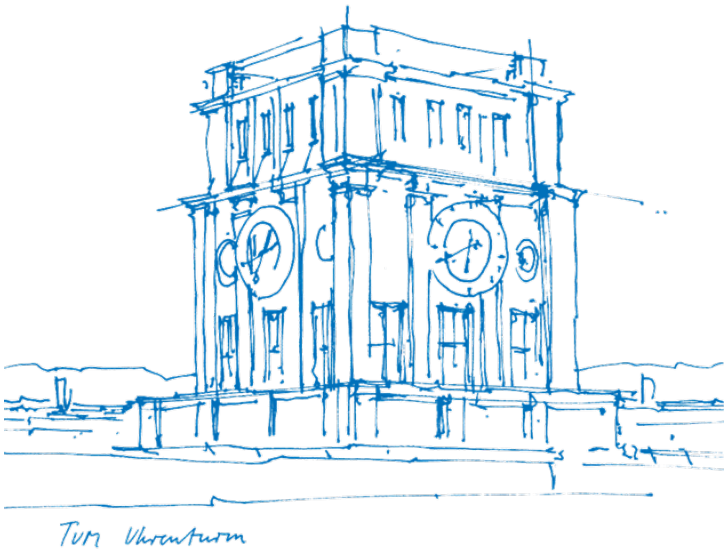

Anharmonic Dynamics and Their Influence on the Optoelectronic Properties of Halide Perovskites

Xiangzhou Zhu

Technische Universität München
TUM School of Natural Sciences

Anharmonic Dynamics and Their Influence on the Optoelectronic Properties of Halide Perovskites

Xiangzhou Zhu

Vollständiger Abdruck der von der TUM School of Natural Sciences der Technischen Universität München zur Erlangung eines

Doktors der Naturwissenschaften (Dr. rer. nat.)

genehmigten Dissertation.

Vorsitz:

Prof. Jonathan J. Finley, Ph.D.

Prüfer der Dissertation:

1. Prof. Dr. David Egger
2. Prof. Dr. Frank Ortmann

Die Dissertation wurde am 29.04.2024 bei der Technischen Universität München eingereicht und durch die TUM School of Natural Sciences am 10.06.2024 angenommen.

Acknowledgments

First and foremost, I would like to express my deep appreciation to my supervisor, Prof. David A. Egger. I want to thank his support and great patience throughout my PhD journey, both academically and personally. I would also like to thank my mentor, Dr. Bernhard Kretz, for all the discussions and advice.

Moreover, I must thank all the members of the TheoFEM group for always being friendly and helpful. I learned a lot from the scientific discussion with them and enjoyed the time we spent having lunch or other social activities together. Special thanks go to Sebastián Caicedo-Dávila, who shared the office with me, for the valuable discussions we had and for sharing his insights on both scientific and broader topics. I am also sincerely thankful to Stefan Seidl who kindly navigate me to enjoy the local culture during weekends.

My gratitude goes to my collaborators as well, whose contributions and expertise have been invaluable in the research presented in this thesis. First, I want to thank Jonas D. Ziegler, Mateusz Dyksik, Prof. Alexey Chernikov, and Prof. Paulina Plochocka for the experimental work and discussions on 2D perovskites. Second, I want to thank Prof. Omer Yaffe and his group members for their reflectance measurements of $CsPbBr_3$. Similarly, I thank Dr. Franziska Hegner for her collaboration on the ternary nitrides. Furthermore, I want to extend my appreciation to Christian Gehrmann and Sebastián for our fruitful collaboration on the transversal motion of halide perovskites. In particular, I want to thank Stefan for his collaboration on the band gaps of $CsPbBr_3$, which is shown in Section 3.2.

Lastly, my thanks to the Gauss Centre for Supercomputing e.V. for providing computing time through the John von Neumann Institute for Computing on the GCS Supercomputer JUWELS at Jülich Supercomputing Centre, which enabled much of this work.

Abstract

Halide perovskites (HaPs) have emerged as a promising optoelectronic material distinguished by their remarkable properties. Unlike conventional inorganic semiconductors, HaPs exhibit unique anharmonic fluctuations with a soft lattice, closely connected to their favorable optoelectronic properties. However, a comprehensive understanding of their structural dynamics and the profound implications remains elusive. This thesis is dedicated to unraveling the fundamental physical mechanisms and their broader consequences on material functionality.

Employing state-of-the-art computational methods, we probe the anharmonic dynamics and their impact on the electronic properties of $CsPbBr_3$, chosen as a prototypical HaPs. Molecular dynamics (MD) based on density functional theory (DFT) are used to investigate the full anharmonic dynamics. Compared to the results from stochastic Monte Carlo (MC) calculations, the effect of anharmonicity on optoelectronic properties is quantified. To go beyond the inadequate harmonic picture, we developed augmented Monte Carlo methods with imaginary soft phonons taken into account.

Our investigation first characterizes the anharmonic dynamics by analyzing local fluctuations. Specifically, we find that motions of neighboring Cs-Br atoms interlock within a nominal cubic unit cell. This manifests in the most likely Cs-Br distance being shorter than what is inferred from an ideal cubic structure. Furthermore, we quantify the effective potential associated with certain atomic motions at two temperatures. Building on this foundational understanding, we explore the dynamical influence on the material's band gap. Through comparing different levels of theory with experiments, we find that anharmonic fluctuations are a key effect in the electronic structure of these materials. In particular, we demonstrate that mildly changing band gaps across phase transitions cannot be explained by harmonic phonons thermally perturbing an average crystal structure. Further examination leads us to identify overdamped phonon modes, which are highlighted behind the connection of microscopic structural information and the macroscopic functional properties. We show that the separation of dynamic fluctuations into two time scales is intrinsic to the overdamped dynamics and originates from strong phonon-phonon interactions in $CsPbBr_3$. Since the phonon picture breaks down, an independent-phonon-based method cannot capture the band gap behavior of this material.

In conclusion, our findings offer a comprehensive perspective on the optoelectronic properties of halide perovskites, underscoring the critical role of anharmonic dynamics. The elucidation of overdamped behaviors provides a deeper understanding of the material's intrinsic properties, challenging conventional models. This work not only contributes to the theoretical framework of anharmonic systems but also has the potential to inform future developments of photovoltaic materials.

List of Publications

The research presented in this work was done in the research group Theory of Functional Energy Materials, Technical University of Munich. Parts of the results have been addressed in the following publications:

1. Zhu, X., & Egger, D. A., Role of overdamped dynamics in halide perovskites, *arXiv:2406.05201* (2024)
2. Hegner, F. S., Cohen, A., Rudel, S. S., Kronawitter, S., Grumet, M., Zhu, X., Roman, K., Houben, L., Jiang, C.-M., Schnick, W. W., Kieslich G., Yaffe, O., Sharp, I. D., & Egger, D. A., *Adv. Energy Mater., 2303059* (2024)
3. Seidl, S.A.*, Zhu, X.*, Reuveni, G., Aharon, S., Gehrmann, C., Caicedo-Dávila, S., Yaffe, O. & Egger, D.A., *Phys. Rev. Mater. 7, L092401* (2023) (*equal contributions)
4. Ziegler, J.D., Lin, K.Q., Meisinger, B., Zhu, X., Kober-Czerny, M., Nayak, P.K., Vona, C., Taniguchi, T., Watanabe, K., Draxl, C. and Snaith, H.J., *ACS Photonics, 9 (11), 3609-3616* (2022)
5. Zhu, X.; Caicedo-Dávila, S.; Gehrmann, C.; Egger, D. A., *ACS Appl. Mater. Interfaces, 14 (20), 22973-22981* (2022)
6. Gehrmann, C.; Caicedo-Dávila, S.; Zhu, X.; Egger, D. A., *Adv. Sci. 9, 220076* (2022)
7. Dyksik, M., Duim, H., Zhu, X., Yang, Z., Gen, M., Kohama, Y., Adjokatse, S., Maude, D.K., Loi, M.A., Egger, D.A. and Baranowski, M., *ACS Energy Lett., 5 (11), 3609-3616* (2020)
8. Ziegler, J.D., Zipfel, J., Meisinger, B., Menahem, M., Zhu, X., Taniguchi, T., Watanabe, K., Yaffe, O., Egger, D.A. and Chernikov, A., *Nano Lett., 20 (9), 6674-6681* (2020)

Contents

1 Introduction

Energy consumption is critical for modern civilization. The global energy requirement may increase 50% by 2050 [1] due to population growth and industrial development. This increasing demand for energy leads to more and more concern of the depletion of fossil fuels and climate change. Today, the global average surface temperature is already approaching 1.2 °C above pre-industrial levels, which leads to potential climate risks [2]. In this context, developing renewable energy sources has thus become urgently needed. Among them, solar energy is considered a leading candidate for an alternative energy source, which has grown rapidly in recent years. According to the International Energy Agency's (IEA) report in 2023 [3], the world could have manufacturing photovoltaics (PV) capacity for more than 1200 GW per year by 2030, a huge increase from 385 MW in 2000. To reach the roadmap of "Net Zero by 2050" [4], solar PV should generate over 23 000 TWh by 2050, equivalent to about 90% of all electricity produced in the world in 2020.

The large demand for accessible solar energy calls for advancements in high-efficiency and low-cost solar cell materials. Silicon-based solar cells have been the predominant PV technology occupying the largest share of the market for decades [5]. Mainly made from crystalline silicon, the efficiencies of these cells have been gradually improved, with efficiencies now averaging around 15-20% for commercial products and 26.8 % in the lab [6]. However, several limitations make it difficult to further scale up for commercial production. On one hand, silicon solar cells are approaching the efficiency limits. On the other hand, the complex vacuum-based manufacturing processes at high temperatures make it hard to produce and generate a large amount of waste [7].

Thus, new types of PV materials have been explored for solar cell production in recent years. Halide perovskites (HaPs) have demonstrated the potential to be used in next-generation solar cells due to their inexpensive fabrication and optimal photoelectric properties. These materials are characterized by the general formula ABX_3, where 'A' is a monovalent cation (organic or inorganic), 'B' a divalent metal, and 'X' a monovalent halogen. Perovskite solar cells offer industry advantages such as lower production costs, lightweight design, and a simple fabrication process with low-temperature solution processing. [8]. Moreover, perovskite solar cells have shown remarkable progress in efficiency [9]. Within one decade, the energy conversion efficiency increased from 4% in 2009 [10] to more than 20% [11]. Now, the best perovskite solar cells have reached 26% [11] in the lab, approaching the performance levels attained by single-crystalline silicon solar cells.

Additionally, perovskites entail broad tunable bandgaps by compositional engineering, which makes them suitable for applications in multi-junction (tandem) solar cells (TSCs) [12], a technology where layers of different materials are used to absorb different parts of

the solar spectrum. Thereby, the solar cell can achieve higher efficiencies even breaking the Shockley–Queisser (S–Q) efficiency limit (33%) [13] of single-junction cells. These rapid advancements highlight the potential of perovskite to lead a paradigm shift in solar cell technology for the next generation. The significant progress in HaP solar cells stems from several key optoelectronic features: sharp absorption edge and high light absorption that allows for thin films, exceptional defect tolerance that enables low-temperature synthesis, and high charge carrier mobility with fewer recombination losses [14, 15].

The functional properties of materials are deeply rooted in their structure. These properties are usually calculated based on the averaged atomic structures determined by traditional crystallography, which represent the periodic symmetry in solid materials. For example, the X-ray diffraction (XRD) spectra measure time- and space-averaged structures, capturing the average atomic positions over the volume sampled and the duration of the exposure [16]. However, unlike the more rigid lattice structures seen in conventional inorganic semiconductors, HaPs exhibit a softer lattice, allowing for more significant atomic movements and even deviation from the averaged structure at finite temperatures [17]. This flexibility in structure leads to a series of distinctive behaviors in properties: the local disorder potentials give rise to sharp optical absorption edges [18], the octahedral rotation influences the band gap [17], the dynamic disorder significantly affects charge carrier dynamics [19].

Such observations in the literature demonstrate that the structural attributes of HaPs are closely linked to their optoelectronic performance. Therefore, it is crucial to consider the effect of structural dynamics at finite temperatures. Typically, solid materials are analyzed using the harmonic approximation, which expands the potential energy up to second-order terms (see section 2.4.1) and employs the perturbative method (see section 2.5.1) to deal with electron-phonon coupling. On the contrary, halide perovskites are characterized by significant anharmonic vibrational fluctuations, where the atomic motions deviate from simple harmonic behavior. Understanding the impact of these special dynamics is therefore important for improving their performance for advanced solar cell applications.

However, a gap still remains between the understanding of the physical model for anharmonic dynamics and the optoelectronic properties within these materials. Three challenges emerge in the study of the relevant topics:

The first challenge is to understand and quantify the dynamic effects, specifically the anharmonic vibrational fluctuations within HaPs. Accurately modeling these dynamics is crucial but presents a significant challenge due to their complicated nature. Variety of concepts are used to describe the dynamics effects, such as "dynamic disorder" [19], "local distortion" [20], "octahedral tilting" [21], "anharmonicity" [22], and "overdamped" [23]. Without clarifying the relationship of different languages, a unified perspective to understand the dynamics in this system is still missing.

The second challenge lies in computing the impact of these dynamic effects on the electronic properties of HaPs. Both of the high-order terms in electron-phonon interactions [24] and phonon-phonon interactions (or anharmonicity) [22] are likely critical for electronic structures in finite temperature. As a result, the well-established perturbative method

based on second-order electron-phonon coupling or harmonic approximation of phonon usually does not work well in these systems.

The third challenge, on top of the other two, is to develop a robust conceptual framework that bridges the intricate dynamics effects with the related electronic properties. This involves not only a deep understanding of both the dynamic and electronic aspects but also the ability to synthesize these understandings into a coherent, comprehensive model. Such a framework is essential for predicting material behavior and guiding the design of next-generation optoelectronic devices.

These challenges form the cornerstone of this thesis, which aims to contribute to the understanding of the structure–property relationship of HaPs in the field of optoelectronics. Focusing on a prototypical HaP, $CsPbBr_3$, this work seeks to unravel the complex interplay between structural dynamics and optoelectronic functionality, shedding new light on a material that stands at the forefront of modern material science.

In addressing the outlined challenges, this thesis employs a combination of advanced computational methods to study the anharmonic dynamics and their influence on the optoelectronic properties of $CsPbBr_3$. The primary method used is molecular dynamics (MD) simulations based on density functional theory (DFT). The advantage of this approach is that it includes the full order of anharmonicity intrinsically, which evaluates the instantaneous forces and energy using DFT. It enables the investigation of local structural fluctuations and anharmonic dynamics in real time. By simulating the atomic movements and the time correlations within the system, MD provides insight into the dynamic disorder and local structures that characterize these materials. Combining the MD structures with DFT band gap calculation, we can study the finite temperature electronic properties considering anharmonicity.

While MD is a powerful tool to provide us with a large amount of information about the anharmonic system, it is difficult to interpret. The stochastic Monte Carlo (MC) method is another framework to study the band gap and electron-phonon interactions. Since it is based on the phonon model, it allows us to disentangle the contribution of each term. However, the application of standard MC is limited to harmonic systems because of the harmonic approximation employed during phonon calculations. In this work, we discuss the possible ways to augment MC with anharmonic effects. A new method to treat the imaginary phonon modes in harmonic approximation is proposed.

The thesis is organized as follows: Chapter 1 provides an overview of the demand for solar cells to fulfill the renewable energy requirement, the favorable properties of perovskites in optoelectronics, and the challenges in understanding their anharmonic vibrational dynamics and optoelectronic properties. Chapter 2 introduces the theory and computational methods used in the thesis, including DFT, MD, lattice dynamics, and electron-phonon interaction. Chapter 3.1 presents an in-depth analysis of the anharmonic vibrational dynamics observed in $CsPbBr_3$, exploring the implications of local distortions and octahedral tilting. Chapter 3.2 examines the impact of anharmonic dynamics on the band gap behavior of $CsPbBr_3$ at different temperatures and phases. Chapter 3.3 further explores the findings from the previous chapters from the viewpoint of overdamped dynamics to develop a comprehensive understanding of how anharmonic dynamics influence the op-

toelectronic properties of HaPs. Chapter 4 summarizes the key findings of the thesis and discusses the implications for future research.

In summary, the thesis offers a multi-faceted perspective on the complex interplay between structural dynamics and electronic structures, especially the band gaps, in HaPs, constructing a coherent conceptual framework to understand the microscopic structural behavior as well as the macroscopic experimental observables.

2 Theory

2.1 Born-Oppenheimer approximation

One of the most foundational equations in solid-state physics is the many-body Schrödinger equation, which includes the dynamics of both electrons and nuclei within a material, offering insights into its fundamental properties

$$\hat{H}\Psi_s(\{\mathbf{r}\},\{\mathbf{R}\}) = E_s\Psi_s(\{\mathbf{r}\},\{\mathbf{R}\}), \tag{2.1}$$

where the many-body wave function $\Psi_s(\{\mathbf{r}\},\{\mathbf{R}\})$ depends on electronic $\{\mathbf{r}\}$ and nuclear $\{\mathbf{R}\}$ coordinates.

A complete Hamiltonian contains the kinetic energy operator of the electrons (nuclei) $\hat{T}_e$ ($\hat{T}_N$), potential operators of the electron (nuclei) $\hat{V}_{ee}$ ($\hat{V}_{NN}$), and interaction between electron and nuclei $\hat{V}_{eN}$ [25],

$$\begin{aligned}\hat{H} &= \hat{T}_e + \hat{V}_{eN} + \hat{V}_{ee} + \hat{T}_N + \hat{V}_{NN} \\ &= -\frac{\hbar^2}{2m_e}\sum_i \nabla_i^2 - \sum_{i,I}\frac{Z_I e^2}{|\mathbf{r}_i - \mathbf{R}_I|} + \frac{1}{2}\sum_{i\neq j}\frac{e^2}{|\mathbf{r}_i - \mathbf{r}_j|} \\ &- \sum_I \frac{\hbar^2}{2M_I}\nabla_I^2 + \frac{1}{2}\sum_{I\neq J}\frac{Z_I Z_J e^2}{|\mathbf{R}_I - \mathbf{R}_J|},\end{aligned} \tag{2.2}$$

where M_I (m_e) and Z_I denote the nuclei (electron) mass and charge.

Although this Hamiltonian contains all the information for the system at equilibrium, it becomes too complicated to be solved as the number of particles increases. *Born–Oppenheimer (BO) approximation* [26] is widely used to simplify the problem. This approximation is based on the fact that nuclei are much heavier than electrons, leading to much slower nuclear motion compared to electronic motion. Thus, the nuclear kinetic part $\hat{T}_N$ can be ignored, and the nuclei coordinates are fixed. The nuclear potential term is now a constant E_{NN} and can be ignored as well. As a result, we are able to separate the electronic part of Hamiltonian and assume we know the exact solution of the corresponding Schoŕdinger equation,

$$\hat{H}_e\psi_i = (\hat{T}_e + \hat{V}_{eN} + \hat{V}_{ee})\psi_i = E_i(\{\mathbf{R}\})\psi_i(\{\mathbf{r}\};\{\mathbf{R}\}), \tag{2.3}$$

where $\psi_i(\{\mathbf{r}\};\{\mathbf{R}\})$ defines the complete set of electron wave functions at each nuclear coordinate $\{\mathbf{R}\}$. The full solution of the nuclei and electrons system $\Psi_s(\{\mathbf{r}\},\{\mathbf{R}\})$ can be written as an expansion of the electronic complete set $\{\psi_i\}$[25, 27]

$$\Psi_s(\{\mathbf{r}\},\{\mathbf{R}\}) = \sum_i \chi_{si}(\{\mathbf{R}\})\psi_i(\{\mathbf{r}\};\{\mathbf{R}\}), \tag{2.4}$$

and the nuclear wave functions $\chi_{si}(\{\mathbf{R}\})$ can be viewed as expansion coefficients.

Then we can insert Eq. (2.4) into Eq. (2.1), multiply on the left by ψ_j^*, and integrate over electronic coordinates $\{\mathbf{r}\}$. Considering the chain rule, one is able to obtain an equation for $\chi_{si}(\{\mathbf{R}\})$,

$$\left(-\sum_I \frac{\hbar^2}{2M_I}\nabla_I^2 + E_j(\{\mathbf{R}\})\right)\chi_{sj} + \sum_i C_{ji}\chi_{si} = E_s\chi_{sj}, \tag{2.5}$$

where

$$C_{ji} = -\sum_I \frac{\hbar^2}{2M_I}\int d\mathbf{r}\left(\psi_j^*\nabla_I^2\psi_i + 2\psi_j^*\nabla_I\psi_i\nabla_I\right). \tag{2.6}$$

The Born-Oppenheimer approximation allows us to ignore the off-diagonal C_{ji} terms ($j \neq i$), which means electrons stay in the same state as nuclei move. As to the diagonal case, the second term in Eq. (2.6) is zero as well, given the requirement for normalization. As a result, only one diagonal term is left

$$C_{jj} = -\sum_I \frac{\hbar^2}{2M_I}\int d\mathbf{r}\psi_j^*\nabla_I^2\psi_j. \tag{2.7}$$

Now the nuclear wave function χ_{sj} for each electronic state j is fully decoupled and described by the following equation

$$\left(-\sum_I \frac{\hbar^2}{2M_I}\nabla_I^2 + E_j(\{\mathbf{R}\}) + \sum_i C_{jj}\right)\chi_{sj} = E_s\chi_{sj}. \tag{2.8}$$

This nuclear schoṙdinger equation is still complicated. However, since the nuclei are much heavier compared to electrons, they can be viewed as a point particle and described by classical Hamiltonian

$$\hat{H}^{class} = \sum_I \frac{\mathrm{P}^2}{2M_I} + U(\mathbf{R}_1, ...\mathbf{R}_M), \tag{2.9}$$

where the function $U(\mathbf{R}_1, ...\mathbf{R}_M)$ is called potential energy surface, specifically, a hypersurface of all nuclear coordinates $\mathbf{R}_1, ...\mathbf{R}_M$. Notice it includes the energy of both electrons and nuclei. Thus, the dynamics of atoms would be described with a Newton equation.

$$M_I\frac{d^2\mathbf{R}_I}{dt^2} = -\frac{\partial U}{\partial\mathbf{R}_I} = F_I, \tag{2.10}$$

which indicates that the equilibrium structure ($F = 0$) has the lowest total energy.

The Born-Oppenheimer approximation has proven incredibly successful in explaining and predicting a wide range of material properties. However, it's worth noting that ignoring off-diagonal terms in Eq. (2.6) is only justified when the energy gap between the ground and excited electronic states is larger than the energy scale of the nuclear motion [28].

2.2 Density functional theory (DFT)

After employing the Born-Oppenheimer approximation to decouple electronic and nuclear motions, the next step is to solve Eq. (2.3) to study the electronic properties. Density functional theory (DFT) is one of the most successful methods for studying materials from first principles by providing a way to systematically map the many-body problem onto a single electron problem [29]. It offers a practical approach to solving the Schrödinger equation for electrons in the static potential of nuclei.

2.2.1 Formalism and Mathematical Foundations

Hohenberg-Kohn Theorems

DFT is grounded in the Hohenberg-Kohn theorems, which establish the formalism of using electron density rather than wavefunction to describe the system. In 1964, Hohenberg and Kohn proved that the ground state of a many-electron system is uniquely determined by its electron density $n(\vec{r})$ [30] so that any property of a system of many interacting particles can be viewed as a functional of the ground state density.

Before we introduce the Hohenberg-Kohn theorem (H-K), we define the density as follows:

$$\begin{aligned} n(\mathbf{r}) &= \int d\mathbf{r}_1 d\mathbf{r}_2 \dots d\mathbf{r}_N \psi^*(\mathbf{r}_1, \mathbf{r}_2, \dots, \mathbf{r}_N) \sum_{i=1}^{N} \delta(\mathbf{r} - \mathbf{r}_i) \psi(\mathbf{r}_1, \mathbf{r}_2, \dots, \mathbf{r}_N) \\ &= \langle \psi | \sum_{i=1}^{N} \delta(\mathbf{r} - \mathbf{r}_i) | \psi \rangle, \end{aligned} \tag{2.11}$$

where $\psi(\mathbf{r}; \mathbf{R})$ represents the electronic wavefunction, which, for a given set of nuclear coordinates $\mathbf{R}$, uniquely determines the electron density $n(\mathbf{r})$. For a specific set of nuclear positions $\{\mathbf{R}\}$ and corresponding external potential $\hat{V}_{eN}$, the wave function $\psi(\{\mathbf{r}\})$ is uniquely determined. Consequently, it follows that $\hat{V}_{eN}$ uniquely determines $n(\mathbf{r})$: $\hat{V}_{eN} \rightarrow \psi \rightarrow n(\mathbf{r})$. While this chain of reasoning may seem straightforward, the H-K theorem asserts that the inverse is also true, specifically in the ground state

- **Theorem 1**: The external potential $\hat{V}_{eN}$ is a unique functional of the ground state electron density $n_0(\mathbf{r})$.

As long as $\hat{V}_{eN}$ is determined, the whole Hamiltonian is determined. Therefore, all properties of the system can be fully described by the ground state density $n_0(\mathbf{r})$, offering a groundbreaking perspective on the relationship between electron density and the external potential in quantum systems.

Furthermore, the H-K theorem introduces a variational principle for the electron density.

- **Theorem 2**: The functional that delivers the ground-state energy of the system gives the lowest energy if and only if the input density is the true ground-state density.

It means the functional $E[n]$ alone is sufficient to determine the exact ground state energy and density and provides a practical method to calculate the ground state properties by minimizing the energy with respect to the electron density.

Expanding on this formulation, if we denote the kinetic energy by $\hat{T}$ and the electron-electron Coulomb interaction energy by $\hat{V}ee$ as in Eq (2.3), the total energy can be written as:

$$E = \langle\psi|\hat{T} + \hat{V}_{eN} + \hat{V}_{ee}|\psi\rangle. \tag{2.12}$$

Using Eq (2.11), the energy functional can be expressed in terms of electron density

$$E[n] = \int d\mathbf{r} n(\mathbf{r}) V_{ext}(\mathbf{r}) + \langle\psi[n]|\hat{T} + \hat{V_{ee}}|\psi[n]\rangle \tag{2.13}$$

where $V_{ext}(\mathbf{r}) = -\sum_I Z_I/|\mathbf{r} - \mathbf{R}_I|$ represents the external potential. H-K theorem 2 can be written as $E[n_0] \leq E[n]$, indicating that the energy functional attains its minimum value for the true ground-state electron density $n_0(\mathbf{r})$.

Kohn–Sham equations

The H-K theorem puts the ground state electron density $n_0(\mathbf{r})$ as a central object, allowing us to replace the complex many-body wavefunction with a functional relationship. However, the theorem itself does not provide a specific methodology for constructing this functional. The expression in Eq (2.13) shows that while the first term explicitly depends on the electron density, the exact forms of the kinetic and Coulomb energy functionals remain unknown, presenting challenges for solving the many-body problem in practice.

To address this challenge, Kohn and Sham proposed a solution in 1965 [31], transfroming the original many-body problem into an independent-particle problem. They assumed the existence of an independent particle system sharing the same ground state density as the original interacting system. This simplification allows for solving the independent system with numerical methods, thereby enabling the determination of the ground state density and energy of the original system efficiently.

The key idea of the Kohn-Sham (K-S) approach is to construct a set of Schrödinger-like equations (named as Kohn-Sham equations) for these non-interacting electrons. These equations describe the movement of electrons in an effective potential as following:

$$\left(-\frac{\hbar^2}{2m}\nabla^2 + V_{eff}(\mathbf{r})\right)\phi_i(\mathbf{r}) = \epsilon_i\phi_i(\mathbf{r}), \tag{2.14}$$

where $V_{eff}(\mathbf{r})$ is the effective potential experienced by an electron, $\phi_i(\mathbf{r})$ represents the ith Kohn-Sham orbital, and ϵ_i denotes the energy of that orbital.

The electron density is then derived from the sum of the squares of these orbitals:

$$n(\mathbf{r}) = \sum_{i=1}^{N} |\phi_i(\mathbf{r})|^2. \tag{2.15}$$

This transformation enables the explicit calculation of the total energy of the system as

$$\begin{aligned} E_{KS}[n] &= \int d\mathbf{r} n(\mathbf{r}) V_{ext}(\mathbf{r}) - \frac{\hbar^2}{2m} \sum_{i=1}^{N} \int d\mathbf{r} \phi_i^*(\mathbf{r}) \nabla^2 \phi_i(\mathbf{r}) + \frac{1}{2} \iint d\mathbf{r} d\mathbf{r}' \frac{n(\mathbf{r}) n(\mathbf{r}')}{|\mathbf{r} - \mathbf{r}'|} + E_{XC}[n] \\ &= \int d\mathbf{r} n(\mathbf{r}) V_{ext}(\mathbf{r}) + T_s[n] + E_H[n] + E_{XC}[n], \end{aligned} \tag{2.16}$$

where the first term is due to the external potential, which we have seen in Eq (2.13). The second and third terms represent the kinetic energy of K-S orbitals and the Hartree potential, which can be seen as the self-interaction energy of the density $n(\mathbf{r})$ treated as a classical charge density. The explicit formulations of these three components are known. The last term is called *exchange–correlation energy*, which in principle, encapsulates all the difficult many-body effects. The main challenge is to accurately describe the exchange-correlation energy $E_{XC}[n]$,

According to H-K theorems, the ground state density function n_0 minimizes the total energy, leading to the condition

$$\left. \frac{\delta E_{XC}[n]}{\delta n} \right|_{n_0} = 0, \tag{2.17}$$

Using the Lagrange multiplier method, this variational equation leads to a single-particle Schoŕdinger-like equation mentioned in Eq. (2.14),

$$\left(-\frac{\hbar^2}{2m} \nabla^2 + V_{ext}(\mathbf{r}) + \int d\mathbf{r}' \frac{n(\mathbf{r}')}{|\mathbf{r} - \mathbf{r}'|} + V_{XC}(\mathbf{r}) \right) \phi_i(\mathbf{r}) = \epsilon_i \phi_i(\mathbf{r}), \tag{2.18}$$

where the exchange-correlation potential is defined as $V_{xc}(\mathbf{r}) = \left. \frac{\delta E_{xc}[n]}{\delta n} \right|_{n(\mathbf{r})}$. If the exact form of E_{XC} were known, the ground state energy and density for the many-body electron problem could be precisely solved. However, the exact form of the exchange-correlation energy functional $E_{XC}[n]$ remains unknown, prompting the development of various approximations such as the Local Density Approximation (LDA) [32], Generalized Gradient Approximation (GGA) [33], and hybrid functionals [34, 35, 36]. These approximations attempt to capture the essence of many-body interactions within a manageable computational scheme, marking a continuous area of research within the field of density functional theory.

2.2.2 Computational schemes

Self-consistent field calculations

The next question will be how to solve the K-S equation in practice. In Eq (2.14), we see that in order to solve for $\phi(\mathbf{r})$, V_{eff} is required. However, the V_{eff} depends on density n, which is a function of ϕ_i following Eq. (2.15).

To solve this circular dependency problem, an iterative approach called *self-consistent field (SCF)* is employed. The procedure is the following: we start by constructing a guess of the electron density, for example, adding up the densities of completely isolated atoms.

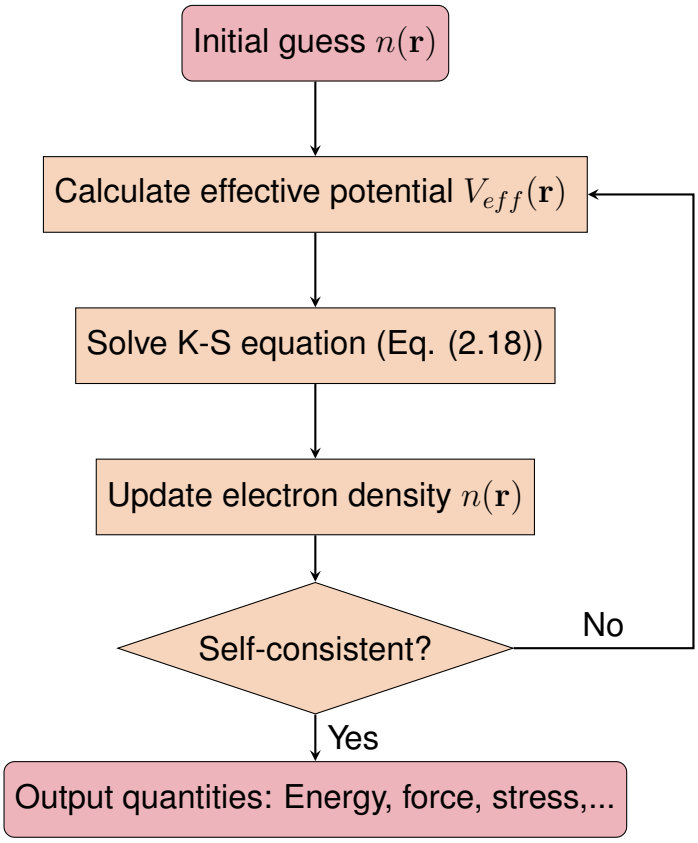

Figure 2.1 Schematic representation of self-consistent loop for the solution of the Kohn–Sham equations.[25]

From this density, we obtain initial estimates of the effective potentials. Then we can solve the K-S equation with that potential and obtain a new density. Unless we input the final ground-state density from the beginning, we will never obtain the same density. Therefore, the new density will be the input for the next iteration, and the process will be repeated until the new density matches the old density within a desired tolerance. A flow chart illustrates the whole process (Fig. 2.1).

It is worth noting that the SCF method is a general method that can extend beyond DFT, for example, the Hartree-Fock (HF) theory [37, 38] or other methods involving variational problems [39].

Hellmann–Feynman theorem

As discussed in section 2.1, both the equilibrium structure and the lattice dynamics require the calculation of forces on atoms. In the context of DFT, it is common to employ *Hellmann-Feynman theorem* [40, 41] to compute the forces. Introduced independently by Hellmann in 1933 and Feynman in 1939, this theorem relates the forces acting on atoms to the electronic structure of the system.

The essence of the Hellmann–Feynman theorem is captured by the following equation

$$\frac{\mathrm{d}E_\lambda}{\mathrm{d}\lambda} = \left\langle \psi_\lambda \left| \frac{\mathrm{d}\hat{H}_\lambda}{\mathrm{d}\lambda} \right| \psi_\lambda \right\rangle, \tag{2.19}$$

which asserts that the derivative of the energy E_λ with respect to a parameter λ (here the position of an atom) can be determined by the expectation value of the derivative of the Hamiltonian with respect to that parameter.

If we apply this to the K-S Hamiltonian in Eq. (2.18), the force on the atom I can be calculated as [29]

$$\mathbf{F}_I = \int d\mathbf{r} n(\mathbf{r}) Z_I \frac{\mathbf{r} - \mathbf{R}_I}{|\mathbf{r} - \mathbf{R}_I|^3} - \sum_{J \neq I} Z_I Z_J \frac{\mathbf{R}_J - \mathbf{R}_I}{|\mathbf{R}_J - \mathbf{R}_I|^3}. \tag{2.20}$$

This equation provides a formalism to directly calculate force using electronic density $n(\mathbf{r})$, which could be easily obtained in DFT framework. In practice, this formalism set the foundation in DFT for optimizing the geometry, searching for the lowest energy structure, and understanding the dynamics in the system.

2.3 Molecular dynamics

2.3.1 Foundations

Molecular dynamics (MD) is a method to simulate the movements of atoms and molecules over time, which allows direct observation of dynamic processes at the atomic scale. Within the Born-Oppenheimer approximation, MD is simplified to a two-step process: First, the forces on atoms are computed by solving a static problem with fixed nuclear positions. The computation of these forces can employ a variety of approaches ranging from empirical potentials to ab initio method or even a machine learning force field [42]. Second, we solve the Newton equation, as seen in Eq. (2.10), using the forces calculated in the first step. Then we move the nuclei according to the principles of classical mechanics. This process is often called *Born-Oppenheimer molecular dynamics*. This work will focus on this approach and use DFT to calculate forces.

Verlet algorithm

In practice, the numerical integration of Newton's equation with discrete time steps is a fundamental step. Among the various algorithms developed for this purpose, the *Verlet algorithm* [43] stands out for its simplicity, stability, efficiency, and preservation of time-reversal symmetry.

The Verlet algorithm computes the positions of particles at a subsequent time step without directly calculating the velocities. This is achieved through a straightforward formula:

$$\mathbf{R}_I(t + \Delta t) = 2\mathbf{R}_I(t) - \mathbf{R}_I(t - \Delta t) + \frac{(\Delta t)^2}{M_I}\mathbf{F}_I(t), \tag{2.21}$$

where the nuclear positions $\mathbf{R}_I$ at time $t + \Delta t$ is calculated from the position at t and $t - \Delta t$. $F_I(t)$ and M_I are the mass and force acting on the particle I at time t.

The Verlet algorithm takes advantage of time reversal symmetry to reduce the error from a discrete time step. The position vector can be Taylor expanded in two time directions,

$$\begin{aligned} \mathbf{x}(t+\Delta t) &= \mathbf{x}(t) + \dot{\mathbf{x}}(t)t + \frac{1}{2}\ddot{\mathbf{x}}t^2 + \frac{1}{6}\dddot{\mathbf{x}}t^3 + \mathcal{O}\left(\Delta t^4\right), \\ \mathbf{x}(t-\Delta t) &= \mathbf{x}(t) - \dot{\mathbf{x}}(t)t + \frac{1}{2}\ddot{\mathbf{x}}t^2 - \frac{1}{6}\dddot{\mathbf{x}}t^3 + \mathcal{O}\left(\Delta t^4\right). \end{aligned} \tag{2.22}$$

Adding these expansions cancels out the first and third-order derivative terms, leading to:

$$\mathbf{x}(t+\Delta t) = 2\mathbf{x}(t) - \mathbf{x}(t-\Delta t) + \ddot{\mathbf{x}}t^2 + \mathcal{O}\left(\Delta t^4\right). \tag{2.23}$$

Thus, we obtain the accuracy of $\mathcal{O}\left(\Delta t^4\right)$ with a calculation up to second order.

A more commonly used approach is the *velocity Verlet algorithm*, where we explicitly calculate velocity. This method keeps track of one position vector $\mathbf{R}_I(t)$ and one velocity vector $\mathbf{v}_I(t)$, rather than two position vectors at two subsequent time steps

$$\mathbf{R}_I(t+\Delta t) = \mathbf{R}_I(t) + \mathbf{v}_I(t)\Delta t + \frac{\mathbf{F}_I(t)}{2M_I}(\Delta t)^2, \tag{2.24}$$

$$\mathbf{v}_I(t+\Delta t) = \mathbf{v}_I(t) + \frac{\mathbf{F}_I(t) + \mathbf{F}_I(t+\Delta t)}{2M_I}\Delta t. \tag{2.25}$$

In this way, the velocity Verlet algorithm provides additional information about the system's kinetic properties.

Nose-Hoover Thermostat

The conservation of energy inherent in the Verlet algorithm makes it ideally suited for microcanonical (*NVE*) ensemble simulations, where the number of particles N, the volume V, and the energy E are kept constant. However, many physical processes occur under conditions with constant temperature where we have to deal with the canonical (*NVT*) ensemble, with constant particle number N, volume V, and temperature T. The *Nose-Hoover thermostat* [44, 45] is a method that allows us to simulate canonical ensemble deterministically by introducing a virtual degree of freedom s for heat bath.

For a system with N atoms, the Nose Lagrangian could be written as [46]

$$\mathcal{L}_{\text{Nose}} = \sum_{i=1}^{N} \frac{m_i}{2} s^2 \dot{\mathbf{R}}_i^2 - U(\{\mathbf{R}\}) + \frac{Q}{2}\dot{s}^2 - g k_B T \ln s. \tag{2.26}$$

m_i denotes the mass of the i-th atom, $U(\{\mathbf{R}\})$ represents the potential energy, g is the total degree of freedom, and Q is the "thermal inertia" controlling the heat exchange rate between the system and the heat bath. In practice, the parameter Q has to be carefully chosen so that it is not too small for decoupling in ionic movement or too large for long simulation time.

The momenta conjugate to R_i and s are determined from the Lagrangian as

$$\begin{aligned} \mathbf{P}_i &\equiv \frac{\partial \mathcal{L}}{\partial \dot{\mathbf{R}}_i} = \mathrm{m}_i s^2 \dot{\mathbf{R}}_i \\ \mathrm{p}_s &\equiv \frac{\partial \mathcal{L}}{\partial \dot{s}} = \mathrm{Q}\dot{s}. \end{aligned} \tag{2.27}$$

It leads to the Nose Hamiltonian as

$$\mathcal{H}_{\text{Nose}} = \sum_{i=1}^{N} \frac{\mathbf{P}_i^2}{2m_i s^2} + U(\{\mathbf{R}\}) + \frac{p_s^2}{2Q} + g k_B T \ln s. \tag{2.28}$$

This Hamiltonian would generate a canonical distribution of the variables $\mathbf{R'}_i$ and $\mathbf{P'}_i$, which are defined as $\mathbf{R'}_i = \mathbf{R}_i$ and $\mathbf{P'}_i = \mathbf{P}_i/s$, respectively. We can interpret the variables with prime as the physical, observable variables and variables without prime as the virtual variables. It can be demonstrated by considering the microcanonical ensemble partition function for the entire system

$$\begin{aligned} \mathcal{Z}_{\text{Nose}} &= \frac{1}{N!} \int dp_s ds d\mathbf{P} d\mathbf{R} \delta \left(E - \mathcal{H}_{\text{Nose}} \right) \\ &= \frac{1}{g k_{\mathrm{B}} T N!} \int dp_s d\mathbf{P}' d\mathbf{R}' \exp\left(-\frac{3N+1}{g k_{\mathrm{B}} T} \left[H\left(\mathbf{P}', \mathbf{R}'\right) + p_s^2/2Q - E \right] \right) \\ &= \frac{\exp(E/k_{\mathrm{B}}T)}{(3N+1) k_{\mathrm{B}} T N!} \int dp_s \exp\left(-\frac{p_s^2}{2Q k_{\mathrm{B}} T} \right) \int d\mathbf{P}' d\mathbf{R}' \exp\left(-\frac{H\left(\mathbf{P}', \mathbf{R}'\right)}{kT} \right), \end{aligned} \tag{2.29}$$

where we consider the number of degrees of freedom, $g = 3N + 1$, and $H(\mathbf{P}', \mathbf{R}')$ represents the Hamiltonian for the physical variables

$$H(\mathbf{P}', \mathbf{R}') = \sum_i \frac{\mathbf{P}_i'^2}{2m_i} + U(\{\mathbf{R}'\}). \tag{2.30}$$

Now we demonstrate that $\mathcal{Z}_{\text{Nose}}$ can be written in the form of a canonical ensemble partition function for $H\left(\mathbf{P}', \mathbf{R}'\right)$ with a scaling constant C, illustrating the equivalence of the Nose-Hoover ensemble to the canonical ensemble

$$\mathcal{Z}_{\text{Nose}} = \frac{C}{N!} \int d\mathbf{P}' d\mathbf{R}' \exp\left(-\frac{H\left(\mathbf{P}', \mathbf{R}'\right)}{kT} \right). \tag{2.31}$$

However, upon closer examination of the real variables $\mathbf{P}'$ and $\mathbf{R}'$, we will notice that the time t is also scaled as $t' = t/s$. This scaling introduces variable time intervals, which complicates the use of these variables for practical simulations, so it is preferable

to work with the equation of motion in virtual variables. They can be derived from the Nose Hamiltonian $\mathrm{H_{Nose}}$ as follows

$$\begin{aligned}
\frac{\mathrm{d}\mathbf{R}'_i}{\mathrm{dt}'} &= \mathbf{P}'_i/\mathrm{m}_i \\
\frac{\mathrm{d}\mathbf{P}'_i}{\mathrm{dt}'} &= -\frac{\partial U\left(\{\mathbf{R}'\}\right)}{\partial \mathbf{R}'_i} - \left(s' p'_s/Q\right)\mathbf{P}'_i \\
\frac{\mathrm{ds}'}{\mathrm{dt}'} &= s'^2 \mathrm{p}'_s/\mathrm{Q} \\
\frac{\mathrm{d}\left(s'\mathrm{p}'_s/\mathrm{Q}\right)}{\mathrm{dt}'} &= \left(\sum_i \mathbf{P}'^2_i/m_i - g k_\mathrm{B} T\right)/Q.
\end{aligned} \tag{2.32}$$

where the virtual variable $s' = s$.

Hoover used a modified equation to simplify the procedure

$$\mathrm{H_{Nose\text{-}Hoover}} = \sum_i \frac{\mathbf{P}_i^2}{2\ \mathrm{m}_i} + U\left(\{\mathbf{R}\}\right) + \frac{\xi^2 \mathrm{Q}}{2} + L k_\mathrm{B} T \ln s \tag{2.33}$$

where the thermodynamic friction coefficient is defined as $\xi = s' p'_s/Q$ and $L = 3N$ denotes the total degree of freedom. The corresponding equation of motion is

$$\begin{aligned}
\dot{\mathbf{R}}_i &= \mathbf{P}_i/\mathrm{m}_i \\
\dot{\mathbf{P}}_i &= -\frac{\partial U\left(\{\mathbf{R}\}\right)}{\partial \mathbf{R}_i} - \xi \mathbf{P}_i \\
\dot{\xi} &= \left(\sum_\mathbf{i} \mathbf{P}_i^2/\mathrm{m}_i - L k_\mathrm{B} T\right)/\mathrm{Q} \\
\dot{s}/s &= \frac{\mathrm{d}\ln s}{\mathrm{d}t} = \xi.
\end{aligned} \tag{2.34}$$

Other than the deterministic method like the Nose-Hoover thermostat, there are stochastic methods like the Anderson thermostat [47] and Langevin thermostat, where the coupling to a thermal bath is considered by adding stochastic collisions on atoms. We will employ the Nose-Hoover thermostat in the rest of this thesis.

2.3.2 Data analysis in Molecular Dynamics Simulations

MD is a powerful technique that offers all the atomic positions and velocities at every time step throughout the simulated trajectory. On the one hand, it provides a large amount of data that enables deep insights into the dynamic behavior of the material. On the other hand, it is challenging to decipher relevant information from the extensive datasets generated. To address this challenge, we explore two primary data analysis methods: statistical analysis and correlation function analysis.

Statistical methods offer a straightforward way to interpret vast amounts of data by providing statistics such as averages or distributions, which can reveal underlying behaviors

in the system. These methods are particularly useful for identifying equilibrium properties and deviations from expected behaviors.

Correlation function methods focus on the temporal or spatial relationships between particles. By examining the correlation of a quantity over time or distance, these methods can uncover transport, diffusion, and spectral functions related to experimental measurements.

Together, these approaches provide a toolkit for extracting meaningful insights from MD simulations, enabling the translation of raw data into a coherent understanding of material dynamics and properties.

Pair distribution function (PDF)

Pair distribution function (PDF) or radial distribution function (RDF) $g(r)$ is a quantity that measures the probability of finding another particle at a distance r from a given reference particle, as illustrated in Fig. 2.2. Since each particle has a unique local environment, the PDF is calculated in a statistical way by considering a large number of reference particles. It offers insight into local order with the distribution of interatomic distances and detects specific structural motifs like defects or disorder [48]. The PDF is particularly useful for characterizing materials without long-range order, such as amorphous solids, glasses, and liquids.

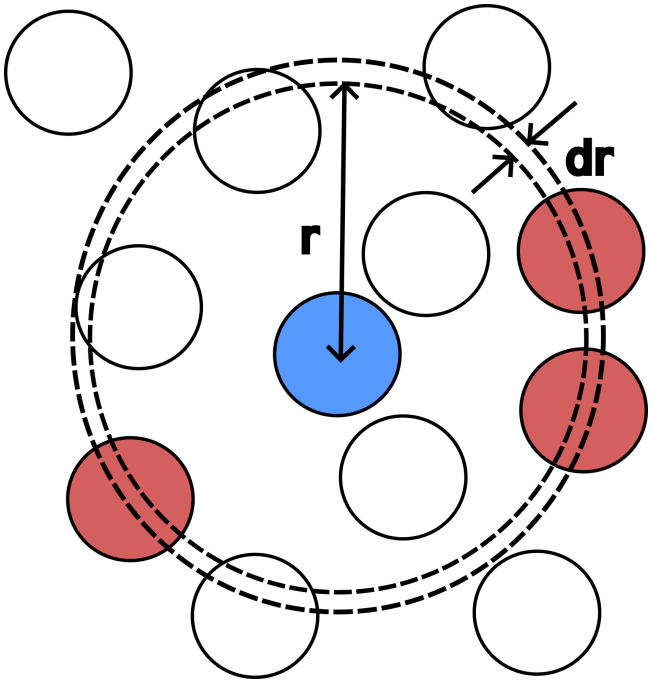

Figure 2.2 Schematic illustration of the radial distribution function. The blue circle in the center represents the reference particle, while the red circles are the particles considered at a distance r.

In theoretical studies [49], PDF is often viewed as a two-point correlation function, derived from the n-particle density function $\rho^{(n)}(\mathbf{r_1}, \ldots, \mathbf{r_n})$. For a system with N parti-

cles in a canonical ensemble (N,V,T) and subjected to the interaction between particles $U(\mathbf{r_1}, \ldots, \mathbf{r_N})$, the corresponding partition function is expressed as

$$Z_{NVT} = \int d\mathbf{r}^N \exp(-\beta U(\mathbf{r_1}, ..., \mathbf{r_N})). \tag{2.35}$$

The probability of the configuration $\{\mathbf{r}_1, \ldots, \mathbf{r}_N\}$ is defined as

$$P^{(N)}\left(\mathbf{r}_1, \ldots, \mathbf{r}_N\right) \mathrm{d}\mathbf{r}_1 \cdots \mathrm{d}\mathbf{r}_N = \frac{\mathrm{e}^{-\beta U_N}}{Z_N VT}\, \mathrm{d}\mathbf{r}_1 \cdots \mathrm{d}\mathbf{r}_N. \tag{2.36}$$

Thus, the n-particle density function can be written as

$$\rho^{(n)}(\mathbf{r}_1, \ldots, \mathbf{r}_n) = \frac{1}{(N-n)!} \left(\prod_{i=n+1}^{N} \int \mathrm{d}^3\mathbf{r}_i \right) \sum_{\pi \in S_N} P^{(N)} \left(\mathbf{r}_{\pi(1)}, \ldots, \mathbf{r}_{\pi(N)} \right), \tag{2.37}$$

where we sum over the N-particles permutation S_N and integrate out the remained coordinates $\mathbf{r}_{n+1}, \ldots, \mathbf{r}_N$.

To obtain a dimensionless function, the n-point correlation function $g^{(n)}$ is defined by factoring out the non-interacting contribution ρ^n [49]

$$\rho^{(n)}(\mathbf{r}_1, \ldots, \mathbf{r}_n) = \rho^n g^{(n)}(\mathbf{r}_1, \ldots, \mathbf{r}_n) \tag{2.38}$$

As a result, the pair distribution function $g(\mathbf{r}_1, \mathbf{r}_2)$ with $n = 2$ is

$$g\left(\mathbf{r}_1, \mathbf{r}_2\right) = \frac{N(N-1)}{\rho^2 Z_{NVT}} \int \mathrm{dr}_3 \mathrm{dr}_4 \ldots \mathrm{d}\mathbf{r}_N \exp\left(-\beta U\left(\mathbf{r}_1, \ldots \mathbf{r}_N\right)\right). \tag{2.39}$$

In the case of a solid with fully harmonic potential, where U includes only up to second-order terms, the PDF peaks are expected to exhibit a Gaussian distribution as discussed in the next part.

An equivalent expression that is commonly used when analyzing computer simulation is [46]

$$g(r) = \rho^{-2} \langle \sum_i \sum_{j \neq i} \delta(\mathbf{r}_i) \delta(\mathbf{r}_j - \mathbf{r}) \rangle = \frac{V}{N^2} \langle \sum_i \sum_{j \neq i} \delta(\mathbf{r} - \mathbf{r}_{ij}) \rangle. \tag{2.40}$$

In the context of MD, $g(r)$ is determined by computing the histogram of distances between atoms pairs across simulation trajectories. Furthermore, it is possible to examine PDF of two specific atom species in simulation, which provides a great way to analyze how atomic motions couple with each other.

Besides computational methods, the PDF can also be determined from experiments such as X-ray or neutron diffraction[50]. The relationship between the structure factor $S(q)$ and the PDF $g(r)$ is given by

$$S(q) = 1 + \frac{4\pi\rho}{q} \int dr\, \sin(qr)[g(r) - 1], \tag{2.41}$$

which enables a comparison between theoretical models and experimental observations.

Analysis of atomic distribution

Atomic distribution analysis is an intuitive method to visualize the dynamics of atoms within MD simulations. In this work, we calculate atomic distributions by collecting atom positions from MD snapshots, subtracting the positions in the ideal crystal structure at 0 K, and presenting this data in histogram form. Also, the translational and space group symmetries are applied to make full use of available data in the MD trajectory. This method provides a straightforward description of the atomic motion around the ideal position, which is especially useful for materials with soft lattices.

The movement of an atom within an isotropic harmonic potential can be described by the potential energy function $U(r) = Ar^2$. According to the principles of statistical mechanics, the probability of the atom being found at a position defined by coordinates (x, y, z) follows a Boltzmann distribution, which is given by

$$p(x, y, z) = \frac{1}{Z} \exp\left(-\frac{U(r)}{k_{\mathrm{B}}T}\right) = \frac{1}{Z} \exp\left(-\frac{A(x^2 + y^2 + z^2)}{k_{\mathrm{B}}T}\right), \tag{2.42}$$

where Z is the normalization constant, also known as the partition function, defined as $Z = \sum_r \exp\left(-\frac{U(r)}{k_{\mathrm{B}}T}\right)$. The probability distribution $p(x, y, z)$ indicates the likelihood of finding the atom at a specific position while the ideal structure is set at $r = 0$. It shows that a harmonic potential will lead to a Gaussian-shape probability function, reflecting the impact of the central limit theorem on thermal fluctuations. Therefore, by fitting the atomic distribution obtained from MD simulations to the Gaussian-shaped probability function, one can assess the validity of the harmonic approximation for describing the atomic movements. If the material of interest exhibits anharmonic behavior, characterized by potential energy terms of higher order than quadratic, the fitting to a Gaussian distribution might show deviations, suggesting that a simple harmonic model cannot fully capture the material's atomic dynamics.

When analyzing the distribution of atomic movements, it is essential to consider the dimensionality of the data representation. While atoms inherently move in a three-dimensional (3D) space, simplifying this complexity into lower-dimensional distributions, such as one-dimensional (1D) plots, requires careful interpretation. One common approach is plotting the 1D distribution of atomic displacements as a function of the displacement distance r. This method involves transforming the 3D Cartesian coordinates (x, y, z) of atomic displacements into a radial distance r in spherical coordinates.

The transformation to spherical coordinates can be written as

$$\begin{aligned} x &= r\ \sin\theta\ \cos\phi \\ y &= r\ \sin\theta\ \sin\phi \\ z &= r\ \cos\theta. \end{aligned} \tag{2.43}$$

The probability in spherical coordinates is

$$p_s(r, \theta, \phi) = \frac{1}{Z} \exp\left(-\frac{Ar^2}{k_{\mathrm{B}}T}\right). \tag{2.44}$$

The 1D radial probably can be derived by integrating out the angular part in $p_s(r, \theta, \phi)$

$$p_s(r) = \int d\phi \; d\theta \; r^2 \sin\theta \; p_s(r, \theta, \phi) = \frac{4\pi}{Z} r^2 \exp\left(-\frac{Ar^2}{k_{\mathrm{B}}T}\right). \tag{2.45}$$

Notice that the probability of a 3D isotropic harmonic potential now has r^2 factor in addition to the Gaussian function. Similarly, for a 2D analysis, the probability density would incorporate a linear r factor to reflect the area element in polar coordinates.

In many cases, atoms occupy sites without full rotational symmetry, often due to specific bonding directions. Consider a situation where one direction aligns along a bond axis and the other two directions lie perpendicular to this bond, as depicted in a schematic diagram in Figure 2.3. In this scenario, the harmonic potential is described by $U = Ax^2 + B(y^2 + z^2)$, characterized by two distinct parameters A and B, with isotropy confined to the y-z plane perpendicular to the bond direction. To analyze the probability distribution in this case, one can separately fit the atomic distribution along the bonding direction x and within the perpendicular plane y-z.

As mentioned, the presence of anharmonic dynamics often leads to a deviation from Gaussian behavior in the atomic distributions of anharmonic materials. However, in cases where the potential minima do not align with the positions of the ideal structure, the distribution may still be approximated by a Gaussian function with a nonzero mean ($\mu \neq 0$). If we assume that the potential minimum is at (0,0,μ), the probability in Cartesian coordinate can be represented as

$$p(x, y, z) = \frac{1}{Z} \exp\left(-\frac{A(x^2 + y^2 + (z - \mu)^2)}{k_{\mathrm{B}}T}\right), \tag{2.46}$$

and in the spherical coordinate

$$p_s(r, \theta, \phi) = \frac{1}{Z} \exp\left(-\frac{A(r^2 + \mu^2 - 2\mu r \cos\theta)}{k_{\mathrm{B}}T}\right). \tag{2.47}$$

Again, the 1D radial probability in this case is obtained by integrating out two angular coordinates θ and ϕ

$$p_s(r) = \frac{2\pi k_{\mathrm{B}}T}{A\mu} r \left[\exp\left(\frac{-A(r - \mu)^2}{2k_{\mathrm{B}}T}\right) - \exp\left(\frac{-A(r + \mu)^2}{2k_{\mathrm{B}}T}\right)\right] \tag{2.48}$$

This adjusted model provides a useful foundation for interpreting the atoms without isotropic symmetry, producing more complex spatial atomic distributions.

Boltzmann inversion method

The last section showed that a harmonic potential will lead to a Gaussian atomic distribution. In fact, many anharmonic systems could experience a more complex potential energy landscape. The Boltzmann inversion method is a technique to calculate the effective potential energy using the statistical distribution of atomic displacements, which is

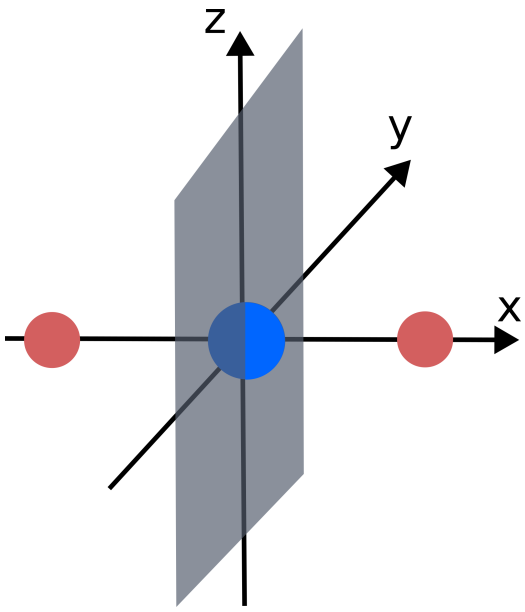

Figure 2.3 Schematic illustration of an atom (blue) bonding with the two nearby atoms (red). The three axes are not asymmetric with bonding direction along the x-axis.

particularly useful in anharmonic materials [17]. This method is based on the principle that the spatial distribution of one particle follows Boltzmann statistics.

If we take the logarithm on both sides of Eq. (2.42), we can derive the expression for a potential from the probability distribution p,

$$U_T(\mathbf{r}) = -k_\mathrm{B}T \ \ln p(\mathbf{r}) + U_0, \tag{2.49}$$

where U_T is the potential energy at a specific temperature T, while U_0 is a reference energy level that can be set arbitrarily for convenience. As a result, we obtain an effective potential energy for one specific atom in the system. It should be noticed that from the perspective of the equilibrium property in a canonical ensemble, this energy should be understood as free energy.

In this work, we are interested in anharmonic materials characterized by imaginary phonon modes. It indicates that the potential energy deviates significantly from simple parabolic wells, which often exhibit potential minima away from the equilibrium positions. By applying the Boltzmann inversion to these materials along directions associated with imaginary phonon modes, one can extract the dynamic potential or effective energy landscape incorporating these anharmonic effects. Therefore, this technique is a powerful tool for probing the complex dynamics of anharmonic materials. Moreover, implementing the Boltzmann inversion method across various temperatures allows for the analysis of the effective energy landscape across phases. It provides insight into the stability, phase transitions, and the role of anharmonic vibrations of the material.

Velocity autocorrelation function

Experimentally-measured observables are often related to correlation functions [51]. With MD simulations, we can generate the time-dependent physical quantities, offering the convenience of studying correlation functions. Therefore, correlation functions are often employed to connect macroscopic physical properties with microscopic variables when analyzing the MD simulations. This connection is particularly valuable in the study of anharmonic materials, since the atomic vibration in MD is not constrained to harmonic approximation. In this context, the *velocity autocorrelation function* (VACF) emerges as an important tool for studying the microscopic dynamics of materials. Notably, by performing a mass-weighted Fourier transform of the VACF, one can obtain the *vibrational density of states* (VDOS), a critical measure for characterizing vibrational modes across the frequency spectrum. This analytical pathway offers a deeper comprehension of the vibrational mechanisms beyond the harmonic approximation.

The *velocity autocorrelation function* (VACF), $\mathcal{C}(\Delta t)$, quantifies how an atom's velocity at one moment correlates with its velocity at a later time and is defined as [51, 52]

$$\mathcal{C}(\Delta t) = \frac{\langle v(t)v(t+\Delta t)\rangle}{\langle |v(t)|^2\rangle}, \tag{2.50}$$

where the brackets $\langle \ldots \rangle$ denote an average over all possible initial time t. Thus we can rewrite Eq. (2.50) in the explicit form

$$\mathcal{C}(t) = \lim_{T\to\infty} \frac{\int_0^T v(t')v(t+t')dt'}{\int_0^T v^2(t')dt'}. \tag{2.51}$$

Considering the movement of an atom j within the l-th unit cell, its displacement, $u_{jl}(t)$, can be written in normal mode coordinates of wave vector $\mathbf{k}$ and mode ν

$$u_{jl}(t) = \frac{1}{(Nm_j)^{1/2}} \sum_{\mathbf{k},\nu} Q_{\mathbf{k}\nu}(t)\mathbf{e}^j_{\mathbf{k}\nu} \exp(i\mathbf{k}\cdot\mathbf{r}^0_{jl}), \tag{2.52}$$

where m_j is the mass of atom j, N is the total number of unit cells and $\mathbf{r}^0_{jl}$ denotes the equilibrium position. Here, the normal mode coordinates $Q_{\mathbf{k}\nu}$ include the effect of both the normal mode amplitude and the time dependence. The displacement vector $\mathbf{e}_{\mathbf{k}\nu}$ denotes the direction in which each atom moves, representing the eigenvector of the phonon mode. Each component of this 3N-dimension vector is associated with one Cartesian coordinate of an atom. It is also normalized according to the following condition

$$\sum_j |\mathbf{e}^j_{\mathbf{k}\nu}|^2 = 1. \tag{2.53}$$

The detailed derivation will be discussed in the next section.

Thus the velocity of atoms can be derived from the time derivative of their displacements

$$v_{jl}(t) = \dot{u}_{jl}(t) = \frac{-i}{(Nm_j)^{1/2}} \sum_{\mathbf{k},\nu} \omega_{\mathbf{k}\nu} Q_{\mathbf{k}\nu}(t)\mathbf{e}^j_{\mathbf{k}\nu} \exp(i\mathbf{k}\cdot\mathbf{r}^0_{jl}), \tag{2.54}$$

where $\omega_{\mathbf{k}\nu}$ denotes the angular frequency of the phonon mode.

Now we focus on the key quantity in VACF in terms of atomic velocities, $\langle|\dot{u}_{jl}(t)\cdot\dot{u}_{jl}(0)|\rangle$. By multiplying with m_j and summing over all atoms j, we arrive at the following expression

$$\sum_j m_j\langle|\dot{u}_{jl}(t)\cdot\dot{u}_{jl}(0)|\rangle = \frac{1}{N}\sum_{\mathbf{k},\nu}\omega_{\mathbf{k}\nu}^2\langle Q_{\mathbf{k}\nu}(t)Q_{-\mathbf{k}\nu}(0)\rangle, \tag{2.55}$$

where in classical limit the correlation function of Q on right hand side is given by

$$\langle Q_{\mathbf{k}\nu}(t)Q_{-\mathbf{k}\nu}(0)\rangle = \frac{k_{\mathrm{B}}T}{\omega_{\mathbf{k}\nu}^2}\cos(\omega_{\mathbf{k}\nu}t), \tag{2.56}$$

Consequently, the sum over all atomic velocities becomes

$$\sum_j m_j\langle|\dot{u}_{jl}(t)\cdot\dot{u}_{jl}(0)|\rangle = \frac{k_{\mathrm{k_B}}T}{N}\sum_{\mathbf{k},\nu}\cos(\omega_{\mathbf{k}\nu}t) = \frac{k_{\mathrm{k_B}}T}{N}\int d\omega g(\omega)\cos(\omega_{\mathbf{k}\nu}t), \tag{2.57}$$

where the VDOS $g(\omega)$ is defined as

$$g(\omega) = \sum_{\mathbf{k},\nu}\delta(\omega-\omega_{\mathbf{k}\nu}) \tag{2.58}$$

Thus, we demonstrate that the Fourier transformation of mass-weighted VACF is equal to VDOS.

In practice, it is not necessary to calculate the Fourier transformation after calculating the VACF. Using the so-called *Wiener-Khintchine* theorem [51], it can be derived from Fourier transformation off velocity directly. *Wiener-Khintchine* theorem states that the power spectrum of the autocorrelation function $Z(\omega)$ can be expressed as the square of the magnitude of the Fourier transform of the initial time-dependent function

$$Z(\omega) = |a(\omega)|^2, \tag{2.59}$$

where $a(\omega)$ is the Fourier transformation of initial time-dependent quantity $x(t)$:

$$a(\omega) = \int x(t)\exp(-i\omega t)dt \tag{2.60}$$

Moreover, the mean-squared displacement (MSD)

$$\mathrm{msd}(\Delta t) = \langle(\mathbf{r}(t+\Delta t)-\mathbf{r}(t))^2\rangle \tag{2.61}$$

could also be expressed in terms of VACF[52] as

$$\mathrm{msd}(\Delta t) = \left\langle\left(\int_t^{\Delta t}dt'\mathbf{v}(t')\right)^2\right\rangle = 2\int_t^{\Delta t}dt'\int_t^{t'}dt''\langle\mathbf{v}(t')\cdot\mathbf{v}(t'')\rangle, \tag{2.62}$$

which indicates that the analysis of the velocity correlation function provides also insights into the diffusion of the material.

2.4 Lattice dynamics

As mentioned in Section 2.1, the Born-Oppenheimer approximation allows for the decoupling of electronic and nuclear movements, simplifying the study of materials by focusing on the electronic behavior in a static lattice framework. In this approach, the electronic properties of materials are calculated on the averaged structure as in traditional crystallography [51]. However, temperature-induced displacements from equilibrium positions may have profound impacts on a material's properties, affecting thermal behaviors [53, 54, 55], carrier transport phenomena [56, 57], and even superconductivity [58, 59]. Incorporating lattice dynamics into the study of materials is crucial for understanding these temperature-dependent effects.

2.4.1 Harmonic approximation

We start with the Hamiltonian of ions in Eq. (2.9). The atomic displacements of atom j in l-th unit cell can be defined as

$$\mathbf{R}_{jl} = \mathbf{r}^0_{jl} + \mathbf{u}_{jl} = \mathbf{R}_l + \boldsymbol{\tau}_j + \mathbf{u}_{jl}, \tag{2.63}$$

where $\mathbf{r}^0_{jl}$ is the equilibrium position, $\mathbf{R}_l$ is a lattice vector and $\boldsymbol{\tau}_j$ is the atom position in the unit cell.

To explore the potential energy U via Newton's equation (Eq. (2.10)), we perform a Taylor expansion around the equilibrium positions with their displacement $\mathbf{u}$

$$\begin{aligned} U(\{\mathbf{u}\}) = U_0 + \sum_i \sum_l \sum_\alpha \Phi^\alpha_{i,l} u^\alpha_{il} + \frac{1}{2!} \sum_{ij} \sum_{lm} \sum_{\alpha\beta} \Phi^{\alpha\beta}_{ij,lm} u^\alpha_{il} u^\beta_{jm} \\ + \frac{1}{3!} \sum_{ijk} \sum_{lmn} \sum_{\alpha\beta\gamma} \Phi^{\alpha\beta\gamma}_{ijk,lmn} u^\alpha_{il} u^\beta_{jm} u^\gamma_{kn} + \dots, \end{aligned} \tag{2.64}$$

where α, β and γ are indices of Cartesian coordinates and U_0 is the lattice potential at equilibrium positions. The tensor Φ are derivatives of the potential energy with respect to displacements called *force constants*. The n$^{\text{th}}$ force constant corresponds to n-body interactions:

$$\begin{aligned} \Phi^\alpha_{i,l} &= \left.\frac{\partial U}{\partial u^\alpha_{il}}\right|_{u=0} = 0, \\ \Phi^{\alpha\beta}_{ij,lm} &= \left.\frac{\partial^2 U}{\partial u^\alpha_{il} \partial u^\beta_{jm}}\right|_{u=0}, \\ \Phi^{\alpha\beta\gamma}_{ijk,lmn} &= \left.\frac{\partial^3 U}{\partial u^\alpha_{il} \partial u^\beta_{jm} \partial u^\gamma_{kn}}\right|_{u=0}. \end{aligned} \tag{2.65}$$

The first order force constant is zero for expansion around the equilibrium position. In harmonic approximation, we neglect higher-order terms beyond the second, focusing on pairwise interactions through second-order force constants.

Thus, the harmonic potential energy can be written in the matrix form

$$U^{harm} = \frac{1}{2} \sum_{ij,lm} \mathbf{u}_{il}^{\mathrm{T}} \cdot \mathbf{\Phi}_{ij,lm} \cdot \mathbf{u}_{jm}, \tag{2.66}$$

where $\mathbf{\Phi}_{ij,lm}$ is a 3×3 matrix encapsulating the second-order force constants

The equation of motion for an atom i in the l-th unit cell under harmonic potential can be written as

$$m_i \ddot{\mathbf{u}}_{il}(t) = \mathbf{F}_{il} = -\frac{\partial U^{harm}}{\partial \mathbf{u}_{il}} = -\sum_{jm} \mathbf{\Phi}_{ij,lm} \cdot \mathbf{u}_{jm}(t). \tag{2.67}$$

This equation can be solved with the plane wave ansatz

$$\mathbf{u}_{il}(t) = \sum_{\mathbf{k},\nu} \mathbf{A}_{i,\mathbf{k}\nu} \exp\left[i(\mathbf{k} \cdot \mathbf{r}_{il}^0 - \omega_{\mathbf{k}\nu} t)\right], \tag{2.68}$$

where $\mathbf{A}_{i,\mathbf{k}\nu}$ is the amplitude vector, indicating both magnitude and direction of atomic displacement.

By substituting the ansatz into Eq. (2.67), we obtain

$$m_i \omega_{\mathbf{k}\nu}^2 \mathbf{A}_{i,\mathbf{k}\nu} = \sum_{jm} \Phi_{ij,0m} \cdot \mathbf{A}_{j,\mathbf{k}\nu} \exp\left[i\mathbf{k} \cdot (\mathbf{r}_{jm}^0 - \mathbf{r}_{i0}^0)\right], \tag{2.69}$$

where the reference atom is in the unit cell with $l = 0$

We introduce the polarisation vector $e_{\mathbf{k}\nu}$ as seen in Eq. (2.52) and define the dynamical matrix $\mathbf{D}(\mathbf{k})$. Equation (2.69) can be transformed into an eigenvalue problem

$$\omega_{\mathbf{k}\nu}^2 \mathbf{e}_{\mathbf{k}\nu} = \mathbf{D}(\mathbf{k}) \cdot \mathbf{e}_{\mathbf{k}\nu}. \tag{2.70}$$

Considering there are n atoms and 3 Cartesian coordinates, the index ν runs from $1 \cdots 3N$. One can express the equation in vector form, where $\mathbf{e}_{\mathbf{k}\nu}$ is a $3N$ column vector weighted by the square root of mass

$$\mathbf{e}_{\mathbf{k}\nu} = \underbrace{\begin{pmatrix} \sqrt{m_1} A_{1,\mathbf{k}\nu}^x \\ \sqrt{m_1} A_{1,\mathbf{k}\nu}^y \\ \sqrt{m_1} A_{1,\mathbf{k}\nu}^z \\ \sqrt{m_2} A_{2,\mathbf{k}\nu}^x \\ \vdots \\ \sqrt{m_n} A_{n,\mathbf{k}\nu}^z \end{pmatrix}}_{3N \times 1}. \tag{2.71}$$

These eigenvectors are not only normalized, as mentioned in Eq.(2.53), but also orthogonal, i.e.,

$$\mathbf{e}_{\mathbf{k}\nu}^{\mathrm{T}} \mathbf{e}_{\mathbf{k}\nu}^* = \mathbf{e}_{\mathbf{k}\nu}^{\mathrm{T}} \mathbf{e}_{-\mathbf{k}\nu} = 1. \tag{2.72}$$

Thus, the $3N$ eigenvectors construct a complete set of N atoms moving in a 3D space. These independent eigenmodes are named as *normal modes*. In other words, we are

able to transform the system of 3N coupled atoms in Cartesian coordinates to a system of 3n non-coupled atoms in normal mode coordinates as seen in Eq. (2.52). This transformation is not just a mathematical convenience but shows the quantized nature of lattice vibrations.

The dynamical matrix $\mathbf{D}(\mathbf{k})$ in this derivation has $3N \times 3N$ dimension. It is possible to decompose $\mathbf{D}(\mathbf{k})$ to $n \times n$ blocks of 3×3 matrices with the index of three Cartesian coordinates. The elements of this matrix are defined as

$$D_{\alpha\beta}(ij,k) = \frac{1}{\sqrt{m_i m_j}} \sum_m \Phi^{\alpha\beta}_{ij,0m} \exp\left[i\mathbf{k} \cdot \left(\mathbf{r}^0_{jm} - \mathbf{r}^0_{i0}\right)\right]. \tag{2.73}$$

Again, $l = 0$ is taken for reference unit cell. Notice that the dynamical matrix includes information on all the interatomic force constants and the phase factors for atomic movements. Since the dynamical matrix $\mathbf{D}(\mathbf{k})$ is Hermitian, the eigenvalues $\omega^2_{\mathbf{k}\nu}$ are real. Therefore, the $3N$ eigenvalues can be viewed as square of the angular frequencies of the $3N$ independent normal modes.

Now we can write the Hamiltonian of the harmonic system in both Cartesian coordinates and normal mode coordinates. For Cartesian coordinates,

$$\mathcal{H} = \frac{1}{2} \sum_{il} m_i |\dot{\mathbf{u}}_{il}|^2 + \frac{1}{2} \sum_{ij} \sum_{lm} \mathbf{u}^{\mathrm{T}}_{il} \cdot \Phi_{ij,lm} \cdot \mathbf{u}_{lm}. \tag{2.74}$$

By substituting $\mathbf{u}$ and $\dot{\mathbf{u}}$ into this equation, one obtains Hamitonian in normal mode coordinate

$$\mathcal{H} = \frac{1}{2} \sum_{\mathbf{k}\nu} \dot{Q}_{\mathbf{k}\nu} \dot{Q}_{-\mathbf{k}\nu} + \frac{1}{2} \sum_{\mathbf{k}\nu} \omega^2_{\mathbf{k}\nu} Q_{\mathbf{k}\nu} Q_{-\mathbf{k}\nu}. \tag{2.75}$$

In practice, the frequency $\omega_{\mathbf{k}\nu}$ can be computed with the density functional perturbation theorem (DFPT) or the frozen phonon approach. In this work, we adopt the latter, where we make small displacements in the supercell and calculate the forces with the Hellmann-Feynman theorem, as shown in section 2.2.2. The force constants can be approximated as

$$\Phi^{\alpha\beta}_{ij,lm} \approx \frac{F^{\beta}_{jm}(\Delta r^{\alpha}_{il}) - F^{\beta}_{jm}(0)}{\Delta r^{\alpha}_{il}}. \tag{2.76}$$

2.4.2 Phonons

In the harmonic approximation, we have derived the normal modes as independent collective excitations of the lattice within classical mechanics. In fact, the normal modes can be conceptualized as a quasi-particle called *phonon*, which can be further understood in the context of quantum mechanics, where phonon represents the quantized lattice vibration.

The harmonic Hamiltonian previously discussed in Eq. (2.75) can be translated into quantum mechanical operator form as [51]

$$\hat{\mathcal{H}} = \frac{1}{2} \sum_{\mathbf{k}\nu} \left(\hat{P}_{\mathbf{k}\nu} \hat{P}^{\dagger}_{\mathbf{k}\nu} + \omega^2_{\mathbf{k}\nu} \hat{Q}_{\mathbf{k}\nu} \hat{Q}^{\dagger}_{\mathbf{k}\nu}\right), \tag{2.77}$$

where $\hat{Q}_{\mathbf{k}\nu}$ is the normal mode coordinates operator and $\hat{P}_{\mathbf{k}\nu}$ is the corresponding momentum operator.

The creation and annihilation operators allow us to quantize these vibrational modes, which are defined as

$$\begin{aligned}\hat{a}_{\mathbf{k}\nu} &= \frac{1}{\sqrt{2\hbar\omega_{\mathbf{k}\nu}}}\left(\omega_{\mathbf{k}\nu}\hat{Q}_{\mathbf{k}\nu} + i\hat{P}_{\mathbf{k}\nu}\right), \\ \hat{a}^{\dagger}_{\mathbf{k}\nu} &= \frac{1}{\sqrt{2\hbar\omega_{\mathbf{k}\nu}}}\left(\omega_{\mathbf{k}\nu}\hat{Q}^{\dagger}_{\mathbf{k}\nu} - i\hat{P}^{\dagger}_{\mathbf{k}\nu}\right).\end{aligned} \tag{2.78}$$

The normal mode coordinates and the corresponding momenta can then be expressed as combinations of these operators,

$$\begin{aligned}\hat{Q}_{\mathbf{k}\nu} &= \sqrt{\frac{\hbar}{2\omega_{\mathbf{k}\nu}}}(\hat{a}_{\mathbf{k}\nu} + \hat{a}^{\dagger}_{-\mathbf{k}\nu}), \\ \hat{P}_{\mathbf{k}\nu} &= -i\sqrt{\frac{\hbar\omega_{\mathbf{k}\nu}}{2}}(\hat{a}_{\mathbf{k}\nu} - \hat{a}^{\dagger}_{-\mathbf{k}\nu}).\end{aligned} \tag{2.79}$$

Furthermore, the quantum-mechanical description of atomic positions and momenta can be obtained by substituting them into Eq. (2.52)

$$\begin{aligned}\hat{\mathbf{u}}_{il} &= \sqrt{\frac{m_p}{Nm_i}}\sum_{\mathbf{k}\nu}\left[l_{\mathbf{k}\nu}\mathbf{e}^{i}_{\mathbf{k}\nu}\exp(i\mathbf{k}\cdot\mathbf{r}^{0}_{il})(\hat{a}_{\mathbf{k}\nu} + \hat{a}^{\dagger}_{-\mathbf{k}\nu})\right], \\ \hat{\mathbf{p}}_{il} &= \sqrt{\frac{m_p\omega^2_{\mathbf{k}\nu}}{Nm_i}}\sum_{\mathbf{k}\nu}\left[l_{\mathbf{k}\nu}\mathbf{e}^{i}_{\mathbf{k}\nu}\exp(i\mathbf{k}\cdot\mathbf{r}^{0}_{il})(\hat{a}_{\mathbf{k}\nu} - \hat{a}^{\dagger}_{-\mathbf{k}\nu})\right],\end{aligned} \tag{2.80}$$

where m_p represents the proton mass and $l_{\mathbf{k}\nu}$ has the dimension of length, which represents the characteristic length of a phonon mode [60]

$$l_{\mathbf{k}\nu} = \sqrt{\frac{\hbar}{2m_p\omega_{\mathbf{k}\nu}}}. \tag{2.81}$$

By substituting Eq. (2.79) into Eq. (2.77) and use the commutation relations, one can express the Hamiltonian in terms of creation and annihilation operator $[\hat{a}_{\mathbf{k}\nu}, \hat{a}^{\dagger}_{\mathbf{k}'\nu'}] = \delta_{kk'}\delta_{\nu\nu'}$

$$\hat{\mathcal{H}} = \sum_{\mathbf{k}\nu}\hbar\omega_{\mathbf{k}\nu}(\hat{a}^{\dagger}_{\mathbf{k}\nu}\hat{a}_{\mathbf{k}\nu} + \frac{1}{2}). \tag{2.82}$$

Consider a wave function $|\psi\rangle$ as the eigenvector of Hamiltonian $\hat{\mathcal{H}}$,

$$\hat{\mathcal{H}}|\psi\rangle = E|\psi\rangle. \tag{2.83}$$

One can see that $\hat{a}^{\dagger}_{\mathbf{k}\nu}|\psi\rangle$ and $\hat{a}_{\mathbf{k}\nu}|\psi\rangle$ are eigenvectors of $\hat{\mathcal{H}}$ with energies $E + \hbar\omega_{\mathbf{k}\nu}$ and $E - \hbar\omega_{\mathbf{k}\nu}$ respectively. Thus, one can view $\hat{a}^{\dagger}_{\mathbf{k}\nu}$ and $\hat{a}_{\mathbf{k}\nu}$ as creating or annihilating one phonon, the quantum of lattice vibrations.

One can construct the wave function $|n_k\rangle$ on state $k = (\mathbf{k}, \nu)$ containing n_k phonons

$$|n_k\rangle = \frac{(\hat{a}_k^\dagger)^{n_k}}{\sqrt{n_k!}}|0\rangle, \tag{2.84}$$

where $|0\rangle$ represents the ground state. The corresponding eigenvalues are

$$\hat{\mathcal{H}}|n_k\rangle = \hbar\omega_k(\hat{a}_k^\dagger\hat{a}_k + \frac{1}{2})|n_k\rangle = \hbar\omega_k(n_k + \frac{1}{2})|n_k\rangle, \tag{2.85}$$

where $\hat{a}_k^\dagger\hat{a}_k$ is defined as *number operator* since $\hat{a}_k^\dagger\hat{a}_k|n_k\rangle = n_k|n_k\rangle$. Specifically, the ground state of this system still possesses energy $\sum_k \frac{1}{2}\hbar\omega_k$ due to zero-point fluctuations, a fundamental quantum mechanical effect. The number of phonons in the system n_k is a function of temperature T and follows Bose-Einstein distribution, crucial for understanding the thermal behavior of materials

$$n_k = \frac{1}{\exp(\hbar\omega_k/k_\mathrm{B}T) - 1}. \tag{2.86}$$

To study the harmonic vibrational energy at a specific temperature T provides insights into the vibrational behavior of materials. Note that the kinetic and potential energies in a harmonic oscillator are equally partitioned.

$$\langle K\rangle = \langle V\rangle = \frac{1}{2}\sum_k \omega_k^2\langle|\hat{Q}_k|^2\rangle, \tag{2.87}$$

leading to the expression of the total vibrational energy as:

$$\langle E\rangle = \langle K\rangle + \langle V\rangle = \sum_k \omega_k^2\langle|\hat{Q}_k|^2\rangle. \tag{2.88}$$

By substituting Eq. (2.79) into the total energy, one can obtain a temperature-dependent MSD in normal mode coordinates

$$\langle|\hat{Q}_k|^2\rangle = \langle n_k|\hat{Q}_k\hat{Q}_k^\dagger|n_k\rangle = \frac{\hbar}{\omega_k}\left(n(\omega_k, T) + \frac{1}{2}\right) = \frac{\hbar}{2\omega_k}\coth\left(\frac{\hbar\omega_k}{2k_\mathrm{B}T}\right). \tag{2.89}$$

At high temperature, where we take $k_\mathrm{B}T \gg \hbar\omega$ in Eq. (2.86), the normal mode amplitude will transit to a classical behavior

$$\langle|\hat{Q}_k|^2\rangle = \frac{k_\mathrm{B}T}{\omega_k^2}. \tag{2.90}$$

Compared to Eq. (2.87), the vibrational energy for each mode aligns with the equipartition theorem, allocating an energy of $\frac{1}{2}k_\mathrm{B}T$ to each degree of freedom.

2.4.3 Anharmonic effects

Up to this point, our discussion has adhered to the harmonic approximation where potential energy is expanded around equilibrium positions up to second-order terms. Examining the Taylor expansion in Eq. (2.64), we can find that the high-order terms become significant with sufficiently large atomic displacements $\mathbf{u}$. The cubic and higher-order behavior beyond harmonic approximation in this expansion is called the *anharmonic effect*. It plays an important role in plenty of phenomena, including structural phase transitions, temperature dependence of band gaps, thermal expansion, and ultralow thermal conductivity [54]. However, it is important to realize that in computation we have to use different methods to treat different kinds of anharmonicity. Figure 2.4 illustrates schematically the three distinct scenarios in which anharmonic effects come into play.

While purely harmonic materials are theoretical idealizations, anharmonic effects can be considered negligible for many systems. Figure 2.4a shows this general case. As shown in Figure 2.4a, a harmonic potential effectively represents the main behavior near the equilibrium position, despite the higher-order terms leading to a deviation from the quadratic potential at larger displacements. However, this approximation becomes less reliable for systems with significant atomic displacements, such as materials at high temperatures or those undergoing phase transitions, as well as materials with soft lattices.

Additionally, the presence of soft modes can make the equilibrium position unstable resulting in a double well potential profile, as illustrated in Figure 2.4b. The emergence of soft modes can destabilize the equilibrium positions, resulting in a double-well potential. In this case, the second-order coefficient in Taylor expansion of potential energy is negative. The harmonic approximation fails to capture the double-well behavior at all. However, a quadratic potential fit might still offer a rough approximation, which works better at higher temperatures where the potential well depth becomes relatively small compared to the kinetic energy.

Particular attention is required for a special scenario where soft modes interact strongly, as shown in Figure 2.4c, potentially leading to overdamped dynamics. This phenomenon challenges the conventional phonon framework, calling for a more sophisticated approach to accurately model such behaviors.

Phonon-phonon interaction

In the framework of phonon theory, anharmonicity is modeled as phonon interactions. This concept can be illustrated by analyzing the cubic term of the Hamiltonian expressed through phonon creation and annihilation operators, where $k = (\mathbf{k}, \nu)$ serves as a compact notation for phonon states:

$$\begin{aligned}\mathcal{H}^{(3)} &= \frac{1}{3!}\sum_{k_1k_2k_3}\Phi_{k_1k_2k_3}\hat{Q}_{k1}\hat{Q}_{k2}\hat{Q}_{k3} \\ &= (\frac{\hbar}{2})^{3/2}\sum_{k_1k_2k_3}\frac{V^{(3)}_{k_1k_2k_3}}{\sqrt{\omega_{k_1}\omega_{k_2}\omega_{k_3}}}(\hat{a}_{k_1}+\hat{a}^{\dagger}_{-k_1})(\hat{a}_{k_2}+\hat{a}^{\dagger}_{-k_2})(\hat{a}_{k_3}+\hat{a}^{\dagger}_{-k_3}).\end{aligned} \tag{2.91}$$

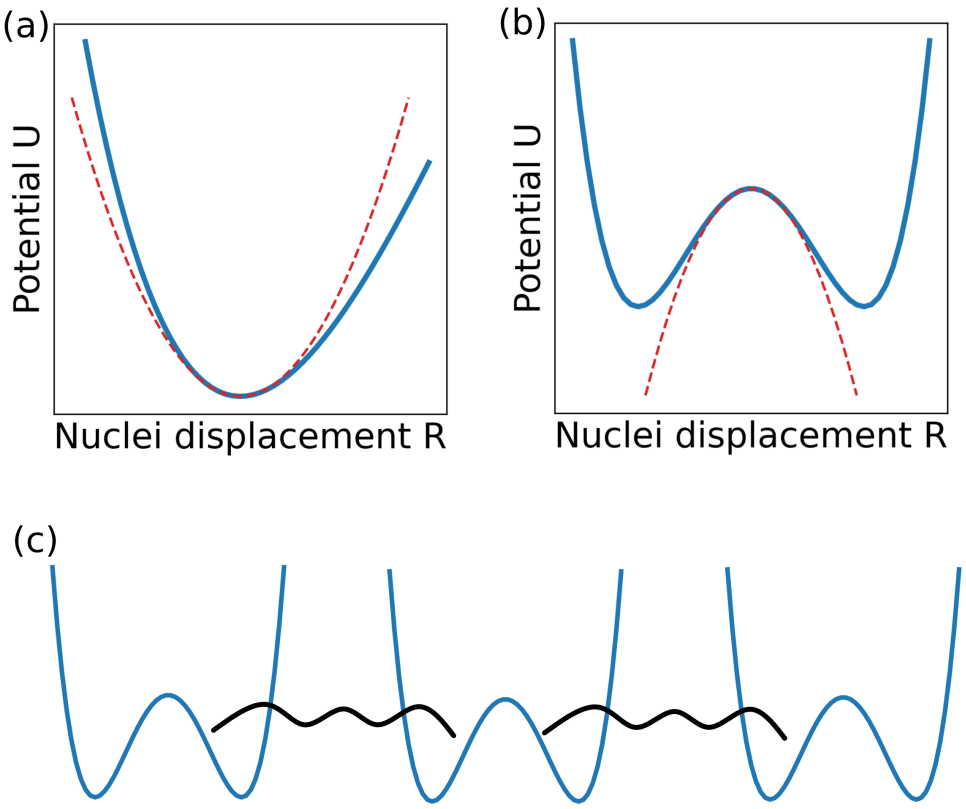

Figure 2.4 Sketches of potentials: (a) Anharmonic potential (solid blue line) can be well captured with harmonic potential around the equilibrium (dashed red line). (b) Anharmonic potential with double well behavior. The potential obtained with harmonic approximation is unstable and leads to imaginary phonon modes. (c) The black curves represent large interactions between phonon modes. This may lead to overdamped dynamics.

Here, $\Phi_{k_1k_2k_3}$ denotes the interaction strength among three phonon modes, and $V^{(3)}_{k_1k_2k_3}$ represents the third-order coupling strength.

This equation results in terms with three creation and annihilation operators and corresponds to the three phonon scattering shown in Fig. 2.5. During the scattering process, the energy and wave vector keep conservation, which can be expressed as

$$\omega_1 + \omega_2 = \omega_3, \tag{2.92}$$

$$\mathbf{k}_1 + \mathbf{k}_2 = \mathbf{k}_3 + \mathbf{G}. \tag{2.93}$$

where ω_i and $\mathbf{k}_i$ denote the frequencies and wave vectors of the phonons, respectively, and $\mathbf{G}$ represents a reciprocal lattice vector. The inclusion of $\mathbf{G}$ accounts for the lattice's periodicity, indicating that the total crystal momentum may not be conserved in interactions involving a non-zero reciprocal lattice vector when $\mathbf{G} \neq 0$. This process plays an important role in heat resistance, known as Umklapp scattering, leading to lower thermal conductivity.

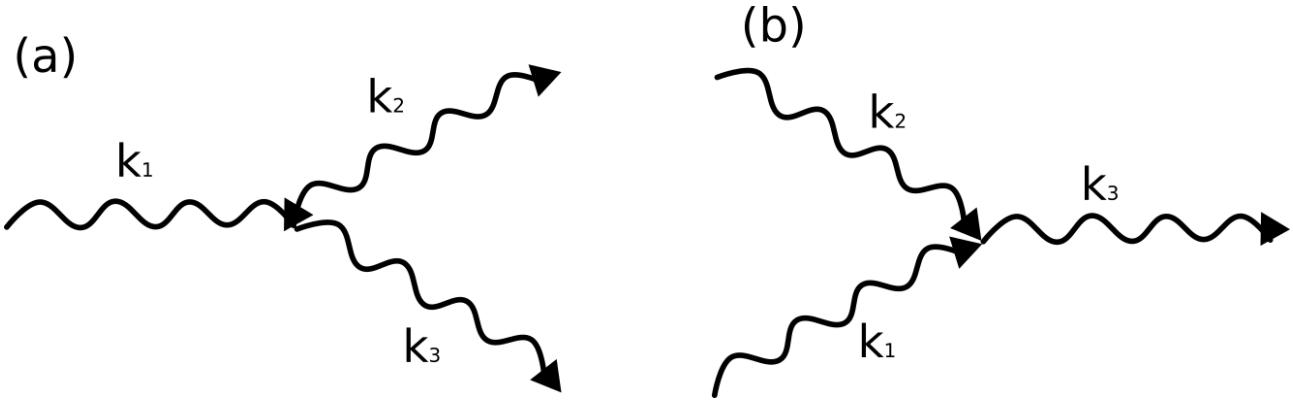

Figure 2.5 Schematic representations of three phonon annihilation (left) and creation (right) processes corresponding to cubic anharmonic interactions.

Furthermore, the phonon-phonon interactions also result in the renormalization of phonon properties. Specifically, it leads to changes in phonon frequency and dampens the phonon modes. Instead of infinite phonon lifetimes as in the harmonic approximation, the anharmonic effect results in finite lifetimes and the broadening of phonon spectral lines. It's worth noting that this renormalization of the phonon properties is also temperature-dependent.

This can be understood with the concept of phonon self-energy and perturbation theory [61]

$$\Sigma(\omega) = \Delta(\omega) + i\Gamma(\omega), \tag{2.94}$$

where the real part $\Delta(\omega)$ is associated with the frequency shift and imaginary part $\Gamma(\omega)$ leads to phonon damping.

According to Cowley [62], the shift in frequency $\Delta_k(\omega)$ calculated with second order cubic anharmonicity (Fig. 2.6a) is

$$\begin{aligned}\Delta_k^{(3)}(\omega) = -\frac{1}{2\hbar^2}\mathcal{P}\sum_{k_1k_2}|\Phi_{k_1k_2k}|^2\Bigg(&\frac{n_1+n_2+1}{\omega_1+\omega_2+\omega}+\frac{n_1+n_2+1}{\omega_1+\omega_2-\omega}\\&+\frac{n_2-n_1}{\omega_1-\omega_2+\omega}+\frac{n_2-n_1}{\omega_1-\omega_2-\omega}\Bigg),\end{aligned} \tag{2.95}$$

where $\mathcal{P}$ represents the principle part and n_k is the occupation number of state k. The first order quartic anharmonicity (Fig. 2.6b) is

$$\Delta_k^{(4)}(\omega) = \frac{1}{2\hbar^2}\sum_{k_1}\Phi_{k,-k,k_1,-k_1}(2n_1+1). \tag{2.96}$$

Since the quartic anharmonicity term only contributes to the frequency shift, the damping part solely has an effect form cubic anharmonicity (Fig. 2.6a). The phonon damping part is expressed with the inverse life time $\Gamma_k(\omega)$

$$\begin{aligned}\Gamma_k(\omega) = \frac{\pi}{\hbar^2}\sum_{k_1k_2}|\Phi_{k_1k_2k}|^2[&(n_1+n_2+1)(\delta(\omega_1+\omega_2-\omega)-\delta(\omega_1+\omega_2+\omega))\\&+(n_2-n_1)(\delta(\omega_1-\omega_2-\omega)-\delta(\omega_1-\omega_2+\omega))].\end{aligned} \tag{2.97}$$

The delta functions correspond to the conservation laws in Eq. (2.92) and 2.93. The renormalized frequency that can be used for fitting to neutron inelastic scattering results can be written as [63]

$$\tilde{\omega}_k^2 = \omega_k^2 + 2\omega_k \Delta_k(\tilde{\omega}_k) \tag{2.98}$$

It should be noted that the above analysis only considers part of the renormalization due to the anharmonic effect. In fact, the effects of thermal expansion would contribute as well, which usually leads to a decrease in frequency as temperature increases. The reason is that the increase in the average distance between atoms will weaken the interatomic interactions.

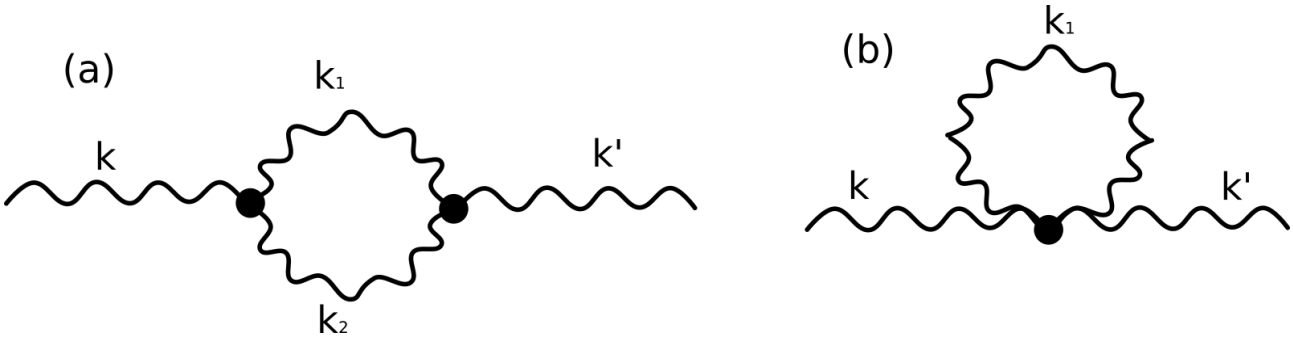

Figure 2.6 Diagrams of the self-energies. (a) The second-order diagram is associated with the cubic term. (b) The first-order diagram is associated with the quartic term.

Overdamped fluctuations

The perturbation theory is widely used for thermal conductivity and heat capacity in anharmonic systems. However, it is not valid for systems with stronger anharmonicity where phonon damping is as large as the frequency. In this case, the phonon-phonon interaction is so large that the phonon picture breaks down, and one can no longer use the quasi-particle based method to calculate thermal or electronic properties. This behavior is called overdamped, which relates to the damped harmonic oscillator (DHO) model. The HaPs were found to exhibit overdamped behavior from both experiments [23] and theory [64].

Here we discuss the overdamped fluctuations starting from the DHO model [65]. The DHO model enables us to describe the motion of a harmonic oscillator subjected to an additional damping force. Since phonons are quanta of vibrational modes, the DHO model can be applied by considering the anharmonic effect (phonon-phonon interaction) as damping. The damping leads to the decay of the oscillator over time, which corresponds to the decrease of phonon life time.

Assuming the phonon mode Q_k oscillates as a damped harmonic oscillator, it follows

$$\frac{d^2 Q_k(t)}{dt^2} + \Gamma_k \frac{dQ_k(t)}{dt} + \omega_k^2 Q_k(t) = 0, \tag{2.99}$$

where Γ_k is the damping coefficient and ω_k is the frequency of undamped harmonic oscillator of mode $k = (\mathbf{k}, \nu)$.

As defined in Eq. (2.50), the autocorrelation function of Q_k can be solved with the initial condition $\frac{dQ_k}{dt}|_{t=0} = 0$ and $Q_k(0) = A$.

In the underdamped case, where $\omega_k > \Gamma_k/2$, it follows that

$$C_Q(t) = Ae^{-\Gamma_k t/2}\left(\cos\omega_k t + \frac{\Gamma_k}{2\Omega}\sin\omega_k t\right), \tag{2.100}$$

where Ω can be seen as the renormalized frequency

$$\Omega = \sqrt{\omega_k^2 - \frac{\Gamma_k^2}{4}}, \tag{2.101}$$

and relaxation time is $\tau = 2/\Gamma_k$.

In the overdamped case, where $\omega_k < \Gamma_k/2$, it follows that

$$\begin{aligned} C_Q(t) &= Ae^{-\Gamma_k t/2}\left(\cosh\omega_k t + \frac{\Gamma_k}{2\Omega}\sinh\omega_k t\right) \\ &= \frac{A}{\tau_L - \tau_S}\left(\tau_L e^{-t/\tau_L} - \tau_S e^{-t/\tau_S}\right), \end{aligned} \tag{2.102}$$

where

$$\begin{aligned} \tau_S &= \frac{\tau}{1+\sqrt{1-(\omega_k\tau)^2}}, \\ \tau_L &= \frac{\tau}{1-\sqrt{1-(\omega_k\tau)^2}}. \end{aligned} \tag{2.103}$$

This shows that in the overdamped case, the lattice fluctuations separate into two time scales, where τ_s and τ_L correspond to the fast (short time-scale) and slow (long time-scale) fluctuation, respectively.

Similarly, one can obtain the velocity autocorrelation function by taking the derivative of $C_Q(t)$ [64],

$$C(t) = \frac{A'}{\tau_L - \tau_S}\left(\frac{1}{\tau_S}e^{-t/\tau_S} - \frac{1}{\tau_L}e^{-t/\tau_L}\right). \tag{2.104}$$

Consider the case $\omega_k \to 0$, we expect $\tau_L >> \tau_S$. Thus, the contribution of slow fluctuations (second term) to velocity autocorrelation is minimal. Since the Fourier transformation of the velocity correlation function is related to VDOS, we can conclude that the contribution of fast fluctuations dominates the VDOS.

2.4.4 Computing methods for phonon renormalization

As mentioned in previous sections, methods such as DFPT or frozen phonon allow us to calculate the phonon frequency $\omega_{\mathbf{k}\nu}$ and phonon dispersion relations within the harmonic approximation. For materials with strong anharmonic effects, various computing methods are established to estimate the phonon frequency shift.

The most straightforward way is to calculate anharmonic terms as self-energy within the many-body perturbation theory of Eq. (2.94). However, perturbation theory is only valid for sufficiently small anharmonic effects and the calculation of higher-order derivatives of the electronic orbitals is challenging. Some methods based on self-consistent phonon (SCPH) theory were developed to include anharmonic effects beyond perturbation theory [66, 67, 68]. Additionally, MD is another nonperturbative approach in investigating phonon anharmonicity, which includes anharmonicity in full order in the simulated trajectories. We will introduce two approaches based on MD used in this thesis.

DynaPhoPy

DynaPhoPy [69] is a method based on normal mode decomposition and projecting velocities onto phonon eigenvectors[70].

Specifically, as discussed in Section 2.3.2, the VACF including anharmonic dynamics can be calculated from MD simulations. Subsequently, the power spectrum of the mass-weighted VACF can be fit to quasiparticle spectral function forms, which enables us to obtain renormalized phonon frequencies and linewidths even for anharmonic materials.

The atomic velocity in Eq. (2.54) can be projected onto a wave vector $\mathbf{k}$

$$v_{j\mathbf{k}} = \sqrt{\frac{m_j}{N}} \sum_l e^{-i\mathbf{k}\cdot\mathbf{r}^0_{jl}} v_{jl}(t). \tag{2.105}$$

And $v_{j\mathbf{k}}$ can be further projected to the phonon mode eigenvector $\mathbf{e}_{\mathbf{k}\nu}$ to obtain the velocity of phonon quasiparticles

$$v_{\mathbf{k}\nu}(t) = \sum_j v_{j\mathbf{k}} \cdot \mathbf{e}^*_{\mathbf{k}\nu}. \tag{2.106}$$

In the end, one can compute the phonon mode power spectrum of $v_{\mathbf{k}s}(t)$ with the auto-correlation function

$$G_{\mathbf{k}\nu}(\omega) = 2\int_{-\infty}^{\infty} \langle v^*_{\mathbf{k}\nu}(0) v_{\mathbf{k}\nu}(\tau)\rangle e^{i\omega\tau} d\tau. \tag{2.107}$$

According to many-body perturbation theory, the retarded one phonon Green's function of mode $k = (\mathbf{k}, \nu)$ is in the form of

$$G_{\mathbf{k}\nu}(\omega) = \frac{1}{\omega^2 - \omega^2_{\mathbf{k}\nu} - 2\omega_{\mathbf{k}\nu}\Sigma_{\mathbf{k}\nu}(\omega)}, \tag{2.108}$$

where $\Sigma_{\mathbf{k}\nu}(\omega)$ is the phonon self energy defined in Eq. (2.94). The Green's function is connected to the velocity autocorrelation function in Eq. (2.107), since the classical expression of one-phonon Green's function can be written as

$$G(k,t) = -\frac{1}{k_{\mathrm{B}}T}\langle v^*_k(0) v_k(t)\rangle \theta(t), \tag{2.109}$$

so in the frequency domain we have

$$G(k,\omega) = \frac{1}{i\omega k_{\mathrm{B}}T}\langle v^*_k v_k\rangle, \tag{2.110}$$

which can be compared to Eq. (2.107). This allows us to approximate phonon quasiparticle spectra from one-phonon Green's functions with MD simulations that does not rely on perturbation theory.

When the renormalization effect is small enough, the phonon mode power spectrum can be fit to a Lorentzian function form [71],

$$G_{\mathbf{k}\nu}(\omega) = \frac{\left\langle |v_{\mathbf{k}\nu}(t)| \right\rangle^2}{\frac{1}{2}\gamma_{\mathbf{k}\nu}\pi\left(1 + \frac{\omega - \tilde{\omega}_{\mathbf{k}\nu}}{\frac{1}{2}\gamma_{\mathbf{k}\nu}}\right)}, \tag{2.111}$$

where $\tilde{\omega}_{\mathbf{k}\nu}$ is the renormalized phonon and $\gamma_{\mathbf{k}\nu}$ is the phonon linewidth.

Temperature Dependent Effective Potentials (TDEP)

TDEP [72, 73, 74] is a method to extract the effective interatomic force constants that best describe a model Hamiltonian by least squares fitting of sampled forces. Since the sampled structure can be obtained by MD simulation (or with stochastic sampling discussed in Section 2.5.3) of a specific temperature, the effective phonon properties are naturally temperature dependent. In practice, the fitting process is largely simplified by considering the symmetry of the force constants.

Consider a supercell with N_a atoms, in harmonic approximation the 2nd-order force constant $\mathbf{\Phi}$ follows (as Eq. (2.67))

$$\vec{f} = -\mathbf{\Phi}\vec{u}, \tag{2.112}$$

where the forces $\vec{f}$ and atomic displacements $\vec{u}$ are $3N_a \times 1$ vectors. The force constant is a $3N_a \times 3N_a$ tensor, but it can be reshaped into a $(3N_a)^2 \times 1$ vector $\vec{\Phi}_v$ allowing us to express the equation as

$$\vec{f} = -(\vec{I} \otimes \vec{u}^T)\vec{\Phi}_v, \tag{2.113}$$

where $\otimes$ is the Kronecker product.

We calculate N_s sampled supercells and obtain $3N_sN_a$ atomic displacements and forces. Then, we can obtain the following overdetermined equation for the effective force constant

$$\underbrace{\begin{pmatrix} \vec{f}_1 \\ \vdots \\ \vec{f}_{N_c} \end{pmatrix}}_{3N_aN_c \times 1} = -\underbrace{\begin{pmatrix} \vec{I} \otimes \vec{u}_1^T \\ \vdots \\ \vec{I} \otimes \vec{u}_{N_s}^T \end{pmatrix}}_{3N_aN_s \times (3N_s)^2} \underbrace{\vec{\Phi}_v}_{(3N_a)^2 \times 1} \tag{2.114}$$

To simplify the problem with symmetry, one can express the force constants via irreducible components

$$\underbrace{\vec{\Phi}_v}_{(3N_a)^2 \times 1} = \underbrace{\vec{C}}_{(3N_a)^2 \times N_x} \underbrace{\vec{x}}_{N_x \times 1} \tag{2.115}$$

This process reduces the number of values to be determined from $(3N_a)^2$ to N_x. Eq. (2.114) can be written as

$$\begin{aligned}\vec{f} &= -(\vec{I} \otimes \vec{u}^T)\vec{C}\vec{x} \\ &= - \underbrace{\vec{A}}_{3N_aN_s \times N_x} \underbrace{\vec{x}}_{N_x \times 1}\end{aligned} \tag{2.116}$$

where $\vec{x}$ contains N_x irreducible components while the coefficient matrix $\vec{A}$ is a function of all the displacements in the supercell.

The $\vec{x}$ is solved as a least squares problem, in which we minimize the difference in forces between DFT forces $\vec{f}^{MD}$ and model Hamiltonian forces $\vec{f}^{H}$

$$\min_{\vec{x}} \Delta\vec{f} = \left|\vec{f}^{MD} - \vec{f}^{H}\right|^2. \tag{2.117}$$

In this way, we obtain the best possible second-order Hamiltonian that can fit the Born-Oppenheimer potential energy surface at finite temperatures.

The higher-order force constants are determined in succession and become smaller and smaller.

$$\vec{A}^{(3)}\vec{x}^{(3)} = \vec{f} - \vec{A}^{(2)}\vec{x}^{(2)}, \tag{2.118}$$

$$\vec{A}^{(4)}\vec{x}^{(4)} = \vec{f} - \vec{A}^{(2)}\vec{x}^{(2)} - \vec{A}^{(3)}\vec{x}^{(3)}. \tag{2.119}$$

The renormalized phonon properties will be solved as discussed in previous sections but from the model Hamiltonian.

2.4.5 Structural phase transitions

A *structural phase transition* refers to changes in the crystal structure of a material due to external conditions such as temperature, pressure, or an external field. For instance, at high temperatures, atoms could have enough kinetic energy to overcome barriers and move to new equilibrium positions. Pressure or external fields, on the other hand, can force atoms closer together or further apart, leading to a structural changes as well. A typical structural phase transition observed in many perovskites is the transition from orthogonal phase to tetragonal phase, then to cubic phase as temperature increases (Fig. 3.1).

Types of structural phase transitions

Based on the dynamic behavior of the high-temperature phase, the structural phase transitions can be classified into two types: *order-disorder phase transition* and *displacive phase transition* [75, 51].

The order-disorder phase transition is characterized by atoms hopping between sites that deviates from the high symmetry sites. On the other hand, displacive transitions are characterized by atoms continuously moving from their initial positions towards new positions,

a process often considered as second-order phase transitions. These transitions are theoretically described by Landau theory, associated with a unique phonon mode termed as the soft mode. It's important to recognize that usually the phase transition of real-world materials cannot be distinctly classified as either order-disorder or displacive phase transition. Typically, it exhibits the characteristics of both order-disorder and displacive mechanisms.

Dove proposed a simple double-well model [51] to display order-disorder and displacive transition in two limit cases. Consider a 1D chain of atoms described by the Hamiltonian

$$H = \frac{m}{2}\sum_j x_j^2 + \frac{J}{4}\sum_{j,j'}(x_j - x_{j'})^2 + \sum_j V(x_j), \tag{2.120}$$

where the first term is kinetic energy, and the second term represents the harmonic interaction of nearby atoms with the coupling strength of J. The last term $V(x_j)$ represents the onsite potential for each atom, given by a double-well potential:

$$V(x_j) = -\frac{1}{2}ax_j^2 + \frac{1}{4}bx_j^4. \tag{2.121}$$

The behavior of phase transitions is influenced by the interplay between the strength of two parameters: The depth of the double-well is $V_0 = a^2/4b$, and the coupling strength J which determines the transition temperature. There are two extreme cases for the model:

- For $V_0 \gg J$, the atoms tend to stay near the potential well minima at $\pm(a/b)^{1/2}$ regardless of temperature. The transition in this scenario is the order-disorder type, where the thermal effects allows atoms to hop between equivalent lattice sites.
- For $V_0 \ll J$, the depth of the potential well becomes relatively insignificant compared with the large thermal vibrations. As a result, the transition would be a displacive transition.

Since we assume a double-well potential in the beginning, it naturally indicates that both cases are rooted in anharmonic interactions. Additionally, an intermediate scenario emerges when the height of potential barrier is comparable to the thermal energy ($k_{\mathrm{B}}T$). This situation may lead to overdamped dynamics (Section 2.4.3), where the phonon picture breaks down.

Based on the wavevector of the phonon modes involved in the transition, one can classify the structural phase transition into *zone center (ferroelectric) phase transitions* and *zone boundary (antiferroelectric) phase transition* [51].

The zone center phase transitions involve phonon modes at the center of the Brillouin zone ($q = 0$), so the size of unit cell does not change. In general, the atomic displacements associated with these modes can break the center of symmetry in unit cell and generate net dipole moment, so it is also called ferroelectric phase transition. One typical example is the perovskite material $BaTiO_3$.

On contrary, the zone boundary phase transitions involve phonon modes at the edge of the Brillouin zone. As a result, the atomic displacements will double the unit cell of low temperature phase. The phase transition from tetragonal to cubic phase seen in Fig. 3.1 belongs to this type. We will focus on this type of phase transition in this article.

Soft-mode theory

Soft-mode theory is a useful tool to understand the nature of displacive phase transitions. Typically, phonon modes are associated with positive frequencies, indicating stable atomic vibrations within the lattice structure. The *soft mode* is a particular phonon mode whose characteristic frequency ω_s reduces to zero as approaching the transition temperature $T \to T_c$, as if the mode is getting "sofften", indicating a decrease in the restoring force for that particular vibrational mode. At this temperature, the crystal is unstable against the corresponding distortion and undergoes a structural phase transition to a low symmetry phase. In essence, the soft mode (at high temperature phase) acts as an indicator to the phase transition, manifesting as a "frozen" distortion that bridges the high-temperature phase with the emerging low-symmetry phase.

The study of soft modes is crucial for understanding the properties of materials since it includes critical dynamical information. In particular, the study of coupling between the soft mode and various physical properties, such as electronic, magnetic or even other vibrational characteristics, offers the microscopic information for changes in those physical properties at finite temperatures [51, 76]. In fact, the soft mode theory of phase transitions was originally developed to explain the origins and mechanisms of ferroelectric phase transitions [77] and soon confirmed by several experimental works [78]. In ferroelectric materials, the soft mode is related to the polarization of the material, and its behavior near the critical temperature can lead to significant changes in the dielectric properties.

As discussed in the last section, the soft mode phase transition is driven by anharmonic interactions. However, the occurrence of soft modes does not require the presence of strong anharmonic interaction. Rather, the emergence of a soft mode is contingent upon the presence of an imaginary harmonic frequency, corresponding to the structural instability of the material in its high-temperature phase.

The soft mode behavior can be derived through Green's function and perturbation theory [79], but it is beyond the scope of this thesis. Here, we use a simplified model to obtain a qualitative understanding of soft modes [51, 80]. We add a mean-field fourth-order anharmonic term to the harmonic crystal Hamiltonian in Eq. (2.75) and obtain an effective quadratic potential in the form,

$$\begin{aligned}\mathcal{H}_{\text{eff}} = &\frac{1}{2}\sum_{\mathbf{k}\nu}\dot{Q}_{\mathbf{k}\nu}\dot{Q}_{-\mathbf{k}\nu} + \frac{1}{2}\sum_{\mathbf{k}\nu}\omega^2_{\mathbf{k}\nu}Q_{\mathbf{k}\nu}Q_{-\mathbf{k}\nu} \\ &+ \frac{1}{4}\sum_{\mathbf{k}\nu}\sum_{\mathbf{p}\mu}V^{(4)}_{\mathbf{k}\nu,-\mathbf{k}\nu,\mathbf{p}\mu,-\mathbf{p}\mu}Q_{\mathbf{k}\nu}Q_{-\mathbf{k}\nu}\langle Q_{\mathbf{p}\mu}Q_{-\mathbf{p}\mu}\rangle,\end{aligned} \tag{2.122}$$

where the usual fourth-order term has been replaced by its thermal averages:

$$Q_{\mathbf{p}\mu}Q_{-\mathbf{p}\mu} \to \langle Q_{\mathbf{p}\mu}Q_{-\mathbf{p}\mu}\rangle. \tag{2.123}$$

One can substitute the thermal amplitude in Eq. (2.90) and obtain the effective Hamiltonian

$$\begin{aligned}\mathcal{H}_{\text{eff}} &= \frac{1}{2}\sum_{\mathbf{k}\nu}\dot{Q}_{\mathbf{k}\nu}\dot{Q}_{-\mathbf{k}\nu} + \frac{1}{2}\sum_{\mathbf{k}\nu}\omega_{\mathbf{k}\nu}^2 Q_{\mathbf{k}\nu}Q_{-\mathbf{k}\nu} \\ &+ \frac{k_{\mathrm{B}}T}{4}\sum_{\mathbf{k}\nu}\sum_{\mathbf{p}\mu}V^{(4)}_{\mathbf{k}\nu,-\mathbf{k}\nu,\mathbf{p}\mu,-\mathbf{p}\mu}Q_{\mathbf{k}\nu}Q_{-\mathbf{k}\nu}/\omega_{\mathbf{p}\mu}^2 \\ &= \frac{1}{2}\sum_{\mathbf{k}\nu}\dot{Q}_{\mathbf{k}\nu}\dot{Q}_{-\mathbf{k}\nu} + \frac{1}{2}\sum_{\mathbf{k}\nu}\tilde{\omega}_{\mathbf{k}\nu}^2 Q_{\mathbf{k}\nu}Q_{-\mathbf{k}\nu},\end{aligned} \tag{2.124}$$

where the renormalized frequencies $\tilde{\omega}$ are defined as

$$\tilde{\omega}_{\mathbf{k}\nu}^2 = \omega_{\mathbf{k}\nu}^2 + \frac{k_{\mathrm{B}}T}{4}\sum_{\mathbf{k}\nu}\sum_{\mathbf{p}\mu}V^{(4)}_{\mathbf{k}\nu,-\mathbf{k}\nu,\mathbf{p}\mu,-\mathbf{p}\mu}/\omega_{\mathbf{p}\mu}^2. \tag{2.125}$$

As a result, for the phonon mode at wave vector $\mathbf{k}$, branch ν, the renormalized frequency with fourth-order anharmonic interaction can be written in the following form

$$\tilde{\omega}^2 = \omega_0^2 + \alpha T. \tag{2.126}$$

Consider an imaginary mode with frequency ω_0, the structure is unstable against the specific phonon mode at 0 K (dashed line in Fig. 2.7). On contrary, in the case of high temperature, the second term in Eq. (2.126) will be large enough to stabilize the system (solid line in Fig. 2.7). At the point $\tilde{\omega} = 0$, the system goes through a phase transition with a transition temperature

$$T_c = -\omega_0^2/\alpha. \tag{2.127}$$

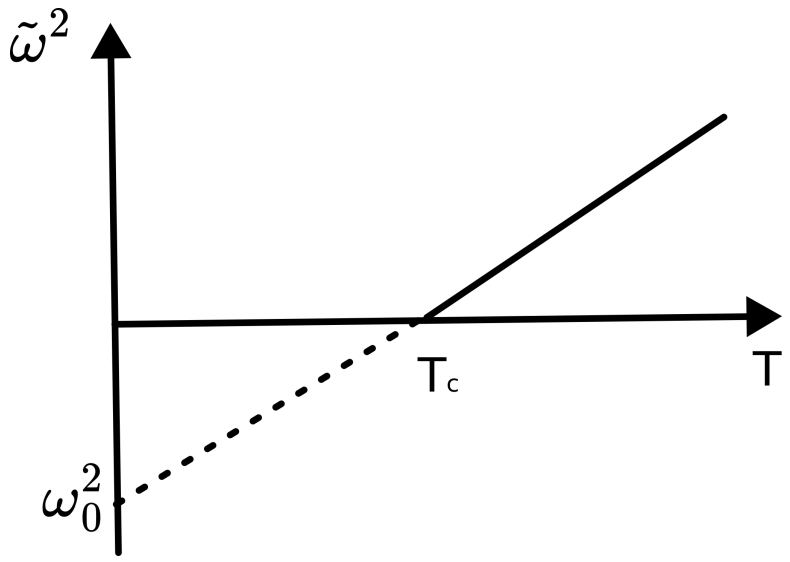

Figure 2.7 Schematic representation of the temperature dependence of the square of the frequency of a soft mode [51]. The dashed line shows that the frequency becomes imaginary below T_c

Notice that soft modes still exist below the transition temperature, where their frequency increases as the temperature further decreases. They could split into two or more modes due to the lifting of degeneracy associated with the break of symmetry in low temperature phases.

2.5 Electron-phonon interactions

Electron-phonon interactions (EPIs) are a fundamental phenomenon in condensed matter physics and materials science. They are relevant for various phenomena, including conventional superconductivity, the carrier mobility, thermalization of hot carriers and the temperature dependence of optical spectra [60, 81].

In this article, we are interested in the band structures of anharmonic materials at finite temperatures. The starting point of most methods introduced here is the so-called *semi-classical Franck-Condon approximation*, which can be derived from the Franck-Condon theory [82]. Within the adiabatic approximation, one can write the quantum mechanical expectation value of electronic excitation energies at temperature T [81, 83]:

$$\varepsilon(T) = \frac{1}{Z}\sum_{k}\langle\chi_k(\mathbf{R})|\varepsilon(\mathbf{R})|\chi_k(\mathbf{R})\rangle e^{-E_k/k_BT} \tag{2.128}$$

where $\varepsilon(T)$ denotes the temperature-dependent electronic excitation energy, offering insight into how electronic properties evolve with temperature. $|\chi_k(\mathbf{R})\rangle$ is the nuclear wavefunction corresponding to the state k, and R represents the nuclear coordinates. E_k is the energy of the kth quantum state, contributing to the partition function $Z = \sum_k e^{-E_k/k_BT}$, which normalizes the contribution of each state by accounting for their Boltzmann weight at temperature T.

One way to categorize the first-principles methods is by how they expand the potential in terms of displacements. There are two main types of approaches:

The first kind of approach considers an expansion of displacements as shown in Eq. (2.129) [81]. The second-order coupling coefficient $a^{(2)}_{\mathbf{q}\nu;\mathbf{q}\nu}$ is either obtained from many-body perturbation theory with electron-phonon matrix elements given in a formalism of DFPT method [60, 84] or directly evaluated for the observable with *finite difference* method [81].

$$\varepsilon_{n\mathbf{k}}(T) = \varepsilon_{n\mathbf{k}}(0) + \frac{1}{N_q}\sum_{\mathbf{q}\nu}\frac{\partial a^{(2)}_{\mathbf{q}\nu;\mathbf{q}\nu}}{\omega_{\mathbf{q}\nu}}\left(n_{\mathbf{q}\nu}(T) + \frac{1}{2}\right), \tag{2.129}$$

where $n_{q\nu}$ is the Bose-Einstein factors as in Eq. (2.86).

The second method considers higher-order terms in the expansion. The band structure is obtained by ensemble averaging the samplings of the distorted structures in phase space. The sampling can be obtained in different ways, for example, from phonon modes using stochastic Monte Carlo (MC) sampling, from trajectory simulation using MD sampling [22] or so-called "Zacharias-Giustino (ZG) displacements" using special displacement method [85].

$$\varepsilon_{n\mathbf{k}}(T) = \frac{1}{M}\sum_{i=1}^{M}\varepsilon_{n\mathbf{k}}(\{\mathbf{u_i}\}). \tag{2.130}$$

2.5.1 Perturbative method and electron-phonon matrix

We consider the following perturbative Hamiltonian describing a coupled electron-phonon system [60]

$$\begin{aligned}\hat{H} = &\sum_{n\mathbf{k}} \varepsilon_{n\mathbf{k}} \hat{c}^{\dagger}_{n\mathbf{k}} \hat{c}_{n\mathbf{k}} + \sum_{\mathbf{q}\nu} \hbar\omega_{\mathbf{q}\nu} \left(\hat{a}^{\dagger}_{\mathbf{q}\nu} \hat{a}_{\mathbf{q}\nu} + \frac{1}{2} \right) \\ &+ \frac{1}{N_p} \sum_{\mathbf{k},\mathbf{q}} \sum_{mn\nu} g^{SE}_{mn\nu}(\mathbf{k},\mathbf{q}) \hat{c}^{\dagger}_{m\mathbf{k}+\mathbf{q}} \hat{c}_{n\mathbf{k}} \left(\hat{a}_{\mathbf{q}\nu} + \hat{a}^{\dagger}_{-\mathbf{q}\nu} \right) \\ &+ \frac{1}{N_p} \sum_{\mathbf{k},\mathbf{q},\mathbf{q}'} \sum_{mn\nu\nu'} g^{DW}_{mn\nu\nu'}(\mathbf{k},\mathbf{q},\mathbf{q}') \hat{c}^{\dagger}_{m\mathbf{k}+\mathbf{q}+\mathbf{q}'} \hat{c}_{n\mathbf{k}} \left(\hat{a}_{\mathbf{q}\nu} + \hat{a}^{\dagger}_{-\mathbf{q}\nu} \right) \left(\hat{a}_{\mathbf{q}'\nu'} + \hat{a}^{\dagger}_{-\mathbf{q}'\nu'} \right).\end{aligned} \tag{2.131}$$

Here, $\varepsilon_{n\mathbf{k}}$ is the single-particle eigenvalue of an electron with crystal momentum $\mathbf{k}$ in the band n, $\omega_{\mathbf{q}\nu}$ is the frequency of a lattice vibration with crystal momentum q in the branch ν. $\hat{c}^{\dagger}_{n\mathbf{k}}/\hat{c}_{n\mathbf{k}}(\hat{a}^{\dagger}_{\mathbf{q}\nu}/\hat{a}_{\mathbf{q}\nu})$ represents the electron (phonon) creation/annihilation operators. The first line describes independent electrons and phonons in second quantization formalism. The second line describes the EPIs to first order of atomic displacement while the third line is EPIs to second order. The electron-phonon matrix elements $g^{SE}_{mn\nu}(\mathbf{k},\mathbf{q})$ (self-energy (SE) term or Fan term) and $g^{DW}_{mn\nu\nu'}(\mathbf{k},\mathbf{q},\mathbf{q}')$ (Debye- Waller (DW) term) measure the strength of the coupling between the electron and the phonon subsystem, which are difficult to evaluate.

In the context of DFT, one can express the basic electron-phonon matrix element with Kohm-Sham eigenfunction $\psi_{n\mathbf{k}}$ and Kohn-Sham potential V_{KS}

$$g^{SE}_{mn\nu}(\mathbf{k},\mathbf{q}) = \left\langle \psi_{m\mathbf{k}+\mathbf{q}} \left| \frac{\partial V_{KS}}{\partial u_{\mathbf{q}\nu}} \right| \psi_{n\mathbf{k}} \right\rangle, \tag{2.132}$$

and

$$g^{DW}_{mn\nu\nu'}(\mathbf{k},\mathbf{q},\mathbf{q}') = \frac{1}{2} \left\langle \psi_{m\mathbf{k}+\mathbf{q}+\mathbf{q}'} \left| \frac{\partial^2 V_{KS}}{\partial u_{\mathbf{q}\nu} \partial u_{\mathbf{q}'\nu'}} \right| \psi_{n\mathbf{k}} \right\rangle. \tag{2.133}$$

It is possible to evaluate the derivatives of Kohn-Sham potentials using the finite displacement method with a supercell [81]

$$\frac{\partial V_{KS}}{\partial u_{\mathbf{q}\nu}} = \frac{V_{KS}(\delta u_{\mathbf{q}\nu}) - V(0)}{\delta u_{\mathbf{q}\nu}}, \tag{2.134}$$

where the displacement $\partial u_{\mathbf{q}\nu}$ refers to a small change in the position of atoms along the phonon mode direction, facilitating the calculation of the potential's sensitivity to such changes. $V_{KS}(\delta u_{\mathbf{q}\nu})$ and $V(0)$ are the Kohn-Sham potentials with and without the displacement, respectively. Alternatively, DFPT method allows for the computation of these derivatives without a supercell and reduce computational effort for large systems with complex symmetry.

By treating the SE part of Hamiltonian in Eq. (2.131) with second order perturbation theory and DW part within first order perturbation theory, one can write the second-order coupling coefficient $a^{(2)}_{\mathbf{q}\nu;\mathbf{q}\nu}$ as [86]

$$a^{(2)}_{\mathbf{q}\nu;\mathbf{q}\nu} = \frac{1}{2} \left(\mathcal{F}_{\mathbf{q}\nu} u^{*}_{\mathbf{q}\nu} u_{\mathbf{q}\nu} + \mathcal{D}_{\mathbf{q}\nu} u^{*}_{\mathbf{q}\nu} u_{\mathbf{q}\nu} \right), \tag{2.135}$$

where corresponds to $\mathcal{F}$ ($\mathcal{D}$) Fan (DW) contributions. At this point, the only approximations we have used are the adiabatic and the harmonic approximations.

However, the DW term that involves second-order variations of Kohn-Sham potential is difficult to calculate in practice. Allen and Heine [87, 88] introduced rigid-ion approximation to calculate the DW matrix elements with first-order variations.

Also, the DFPT calculation involves an integral over the Brillouin zone. It is difficult to converge and needs a very fine grid, sometimes as much as 10^6 wavevectors [60, 84]. This prohibitive task is usually overcome by Wannier interpolation in practice, which calculates EPI matrix in Wannier representation [60].

Given that this formalism is restricted to the harmonic approximation and overlooks the contributions of higher-order terms in electron-phonon coupling, it fails to account for the temperature-dependent phenomena observed in perovskites [24].

2.5.2 Finite difference method

One can obtain the electronic eigenenergies in the form of Eq. (2.129) without considering perturbation theory as well. We start from expanding the electronic eigenenergies $\varepsilon(\mathbf{Q})$ in nuclear positions in normal mode coordinates (phonon amplitude) $\{Q_{\mathbf{q}\nu}\}$ up to the quadratic term [81]

$$\varepsilon_{n\mathbf{k}}(\mathbf{Q}) = \varepsilon_{n\mathbf{k}}(0) + \sum_{\mathbf{q}\nu} \frac{\partial \varepsilon_{n\mathbf{k}}}{\partial Q_{\mathbf{q}\nu}} Q_{\mathbf{q}\nu} + \frac{1}{2} \sum_{\mathbf{q}\nu} \sum_{\mathbf{q}\nu} \frac{\partial^2 \varepsilon_{n\mathbf{k}}}{\partial Q_{\mathbf{q}\nu} Q_{\mathbf{q}'\nu'}} Q_{\mathbf{q}\nu} Q_{\mathbf{q}'\nu'} + \dots \tag{2.136}$$

For a harmonic phonon mode, the vibrational expectation value of the $Q_{\mathbf{q}\nu}$ will vanish

$$\langle Q_{\mathbf{q}\nu} \rangle = 0, \tag{2.137}$$

and since the phonon vibrational modes are independent, only terms with $q = q'$ and $\nu = \nu'$ are left. They have been calculated in Eq. (2.89)

$$\langle Q_{\mathbf{q}\nu} Q_{\mathbf{q}\nu} \rangle = \frac{\hbar}{\omega} \left(n(\omega_{\mathbf{q}\nu}, T) + \frac{1}{2} \right). \tag{2.138}$$

Thus, one can express the electronic eigenenergies in the form like Eq. (2.129)

$$\varepsilon_{n\mathbf{k}}(T) = \varepsilon_{n\mathbf{k}}(0) + \sum_{\mathbf{q}\nu} \frac{\hbar}{2\omega_{\mathbf{q}\nu}} \frac{\partial^2 \varepsilon_{n\mathbf{k}}}{\partial Q_{\mathbf{q}\nu}^2} \left(n_{\mathbf{q}\nu}(T) + \frac{1}{2} \right), \tag{2.139}$$

where the second-order derivative can be evaluated with a finite difference method

$$\frac{\partial^2 \varepsilon_{n\mathbf{k}}}{\partial Q_{\mathbf{q}\nu}^2} \approx \frac{\varepsilon(\delta Q_{\mathbf{q}\nu}) + \varepsilon(-\delta Q_{\mathbf{q}\nu}) - 2\varepsilon(0)}{\delta Q_{\mathbf{q}\nu}^2}. \tag{2.140}$$

The summation in Eq. (2.139) runs over the phonon branch ν and wavevector $\mathbf{q}$, so each term we summed corresponds to a phonon mode with frequency $\omega_{\mathbf{q}\nu}$. To further

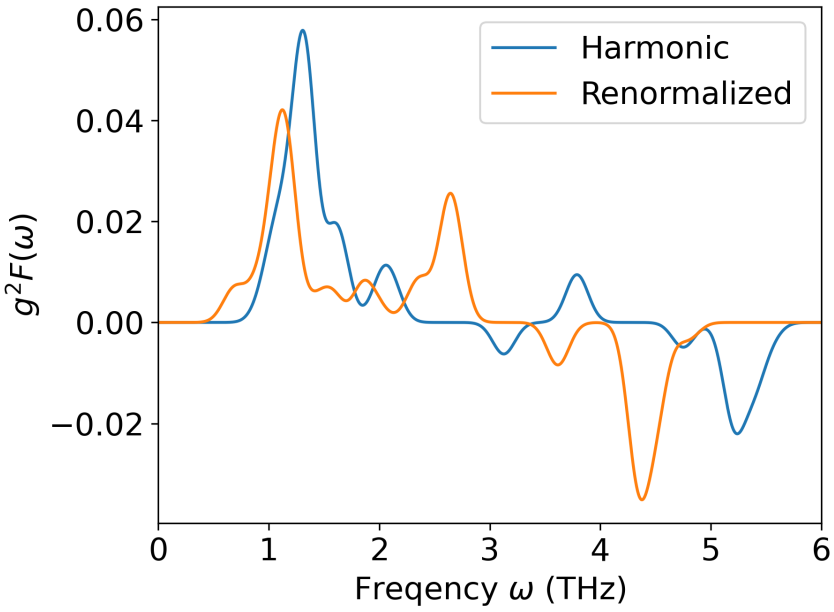

Figure 2.8 Gap spectral functions $g^2F(\omega)$ of cubic phase $CsPbBr_3$ calculated using harmonic phonon (blue) and renormalized phonon (orange).

investigate the contribution of each phonon mode, one can plot them as a function of frequency and obtain the so-called *gap spectral function* $g^2F(\omega)$ [89].

This method is based on harmonic approximation and cannot deal with phonons with imaginary frequency. However, one can use phonon renormalization to generalize it to anharmonic cases. Fig. 2.8 shows the relevant gap spectral functions of cubic phase $CsPbBr_3$.

Even if one includes part of the anharmonic effect for phonon, this method does not consider full electron-phonon coupling, which has shown to be essential for correct temperature effects [24].

2.5.3 Stochastic Monte Carlo methods

Standard Monte Carlo method

Unlike the previous two methods, the Monte Carlo (MC) method can go beyond the quadratic terms in electron-phonon interactions.

Within the harmonic approximation, the nuclear wave function $|\chi_k(\mathbf{R})\rangle$ in Eq. (2.128) can be expressed as a product of independent quantum harmonic oscillators in normal mode coordinates $\chi_n = \prod_\nu \phi_{n_{\mathbf{q}\nu}}(Q_{\mathbf{q}\nu})$, with [83]

$$\phi_n(x_i) = \left(\frac{\omega_{\mathbf{q}\nu}}{\pi}\right)^{1/4} \frac{1}{\sqrt{2^n n!}} \exp\left(-\frac{\omega_{\mathbf{q}\nu} Q_{\mathbf{q}\nu}^2}{2}\right) H_n\left(\sqrt{\omega_{\mathbf{q}\nu}} Q_{\mathbf{q}\nu}\right), \tag{2.141}$$

where the quantum number n represents the occupations of each vibrational quantum state following Bose-Einstein distribution and H_n is the Hermite polynomial of order n.

Using Mehler's formula, one can derive the following expression for the probability distribution that we then substituted in Eq. (2.128):

$$P(Q_{\mathbf{q}\nu}) = \frac{1}{Z}\sum_{n=0}^{\infty} e^{-\frac{E_n}{k_B T}} |\phi_n(Q_{\mathbf{q}\nu})|^2 = \frac{1}{\sqrt{2\pi\langle Q^2_{\mathbf{q}\nu}\rangle_T}} \exp\left(-\frac{Q^2_{\mathbf{q}\nu}}{2\langle Q^2_{\mathbf{q}\nu}\rangle_T}\right), \tag{2.142}$$

where $\langle Q^2_{\mathbf{q}\nu}\rangle_T$ is the mean square displacement of normal mode, as given in Eq. (2.89). It reflects the average amplitude of atomic displacements due to thermal vibrations at temperature T.

As a result, Eq. (2.128) can be written as a high dimensional integral over all phonon modes

$$\varepsilon_{n\mathbf{k}}(T) = \int \prod_{\mathbf{q}\nu} dQ_{\mathbf{q}\nu} \frac{1}{\sqrt{2\pi\langle Q^2_{\mathbf{q}\nu}\rangle_T}} \exp\left(-\frac{Q^2_{\mathbf{q}\nu}}{2\langle Q^2_{\mathbf{q}\nu}\rangle_T}\right) \varepsilon_{n\mathbf{k}}(\mathbf{Q}). \tag{2.143}$$

Although the approach is based on the harmonic approximation, it does not presuppose any specific relationship between electronic observables and nuclear configurations.

Now, we will evaluate the integral with a Monte Carlo importance sampling method. We generate sampling structures with phonon eigenmodes following the probability distribution $P(Q_{\mathbf{q}\nu})$ in Eq. (2.142) and take an average of the electronic energies from the sampling. Thus, the computation of $\varepsilon_{n\mathbf{k}}(T)$ is in the form similar to Eq. (2.130),

$$\varepsilon_{n\mathbf{k}}(T) = \frac{1}{M}\sum_{i=1}^{M} \varepsilon_{n\mathbf{k}}(\{\mathbf{Q}\}_i) \quad \text{where} \quad \{\mathbf{Q}\}_i \sim P(Q_{\mathbf{q}\nu}). \tag{2.144}$$

Since the distribution is a Gaussian function, one can use the standard Box-Muller transform to map it on uniform distributions in practice. We substitute Eq. (2.89) and (2.90) respectively, so that the displacements of atom i will be generated quantum mechanically with

$$\mathbf{u}_i = \sum_{\nu} \sqrt{\frac{\hbar(2n_\nu + 1)}{2m_i\omega_\nu}} \mathbf{e}^i_\nu \sqrt{-2\ln U_1}\cos(2\pi U_2), \tag{2.145}$$

or for classical limit

$$\mathbf{u}_i = \sum_{\nu} \sqrt{\frac{k_B T}{m_i\omega^2_\nu}} \mathbf{e}^i_\nu \sqrt{-2\ln U_1}\cos(2\pi U_2), \tag{2.146}$$

where U_1 and U_2 are random numbers with uniform distributed between $[0, 1]$ and $\mathbf{e}^i_\nu$ is the displacement vector defined in Eq. (2.71). Here, we only consider the $q = 0$ wavevector with a large enough supercell.

The whole process from Eq. (2.141) to Eq. (2.144) is based on quantum mechanics employing the harmonic approximation and semiclassical Franck-Condon approximation (even do not have to be adiabatic). However, for the sake of intuitive understanding, we can directly view the Eq. (2.144) through the lens of classical statistical mechanics. Specifically, it can be seen as a process of sampling through the canonical ensemble of

all phonon normal modes. Each mode is sampled as a normal distribution around zero with a variance of $\langle Q^2 \rangle_T \sim k_B T$, which is precisely a Boltzmann distribution.

So far, the Monte Carlo method is based on harmonic approximation. It is technically infeasible for the current formalism to deal with phonon mode with imaginary frequency, which could lead to imaginary displacements in Eq. (2.145) and (2.146). As mentioned in the finite difference method (section 2.5.2), we can use the renormalized phonon as a starting point to avoid this problem.

This way, we account for the anharmonic effect due to phonon-phonon interaction with an effective harmonic phonon. It could capture essential thermal effects for systems like $SrTiO_3$ [90]. However, this method still cannot deal with strong anharmonicity, for instance, overdamped dynamics in halide perovskites, which breaks down the phonon picture. A technique is needed to treat the higher-order terms in potential energy (Eq. (2.64)).

Augmenting Monte Carlo method

To go beyond limitations of the harmonic potential framework described in the last section, we developed a new way of treating the imaginary frequency, which is the consequence of the soft phonon mode with the double-well feature. The basic idea is to sample the normal mode using a non-Gaussian probability, calculated by solving the Schrödinger equation with a frozen phonon potential.

Similar to the procedure in the previous work of Skelton et al. [91], we first use the frozen-phonon method to calculate the potential well for the imaginary mode. Specifically, we distort the atoms in supercell along the phonon eigenmodes in Eq. (2.70). We calculate each distorted structure using DFT and obtain the potential energy $U(Q)$.

Then, this static potential energy can be fit to a polynomial function up to the 14th order as the thick black line shown in Fig. 3.30a. We solve the time-independent 1D Schrödinger equation in normal mode coordinates Q numerically

$$-\frac{\hbar^2}{2m_p}\frac{d^2\psi_i(Q)}{dQ^2} + U(Q)\psi_i(Q) = E_i\psi_i(Q), \tag{2.147}$$

where m_p is the proton mass, and ψ_i is the wavefunction of the i-th quantum state with energy level E_i (horizontal lines in Fig. 3.30a).

The probability distribution of the specific phonon mode can be evaluated similarly to Eq. (2.142),

$$P_i^{img}(Q) = \frac{1}{Z}\sum_{i=0}^{\infty} e^{-\frac{E_i}{k_B T}}|\psi_i(Q)|^2. \tag{2.148}$$

With this probability distribution, one can generate displacements on the top of the standard Monte-Carlo method described above. In other words, we can include the atomic displacements from all the phonon modes with augmenting the Monte-Carlo method. The imaginary phonon modes will be treated by the process above (Eq. (2.148)) while the real phonon modes with the standard Monte Carlo (Eq. (2.142)). Thus, the electronic energies can be calculated with Eq. (2.144) again.

Although we include the higher-order terms in potential energy, we still assume that the interaction between phonon modes is small. It can be understood by expanding the potential energy in terms of the normal mode coordinates. Since we always calculate potential well separately and solve Schoŕdinger equation in 1D, it means that we have ignored the cross anharmonic terms,

$$\begin{aligned} V(\mathbf{Q}) = &\sum_i a_i^{(2)} Q_i^2 && \text{(harmonic terms)} \\ &+ \sum_i a_i^{(3)} Q_i^3 + a_i^{(4)} Q_i^4 + \dots && \text{(higher-order anharmonic terms)} \\ &+ \sum_{ij} b_{ij}^{(4)} Q_i^2 Q_j^2 + \dots && \text{(cross anharmonic terms)} \end{aligned} \tag{2.149}$$

where $a_i^{(n)}$ and $b_{ij}^{(n)}$ are the parameter of n-th order terms.

To include the cross terms, it is possible to calculate the potential energy as a function of more coordinates and solve the Schoŕdinger equation in higher dimensions for the corresponding probability distribution.

2.5.4 Molecular dynamics methods

We have shown that the stochastic Monte Carlo methods can be viewed as a sampling of the canonical ensemble of independent phonon mode, and it can be augmented by generalizing the form of the potential well from quadratic to higher-order terms. However, the interaction between phonon modes could substantially impact the dynamics and the electronic properties, especially for overdamped systems.

Including full anharmonicity for phonons and full higher-order terms for electron-phonon interaction is a challenge. One way to include all those terms is to leave the many-body approach and phonon picture. By introducing the Born-Oppenheimer approximation, we treat ionic motion classically through MD (Section 2.3). Then, it is possible to employ the ergodic hypothesis and evaluate the ensemble average with the time average of a long enough simulated trajectory

$$\langle \varepsilon_{n\mathbf{k}} \rangle_{ensembe} = \langle \varepsilon_{n\mathbf{k}} \rangle_{time} \tag{2.150}$$

As a result, Eq. (2.130) can be written as

$$\varepsilon_{n\mathbf{k}}(T) = \frac{1}{M} \sum_{i=1}^{M} \varepsilon_{n\mathbf{k}}(t_i) \tag{2.151}$$

In this article, since we use the first-principle MD that treats nuclear motion classically, it only delivers the classical Boltzmann statistics. The zero-point motion effect is missing, so it is only valid in high temperatures. However, the Debye temperature of HaPs (102K for $CsPbBr_3$ [92]) is usually much lower than the temperature range we are interested in this thesis. One can use computationally demanding path integral molecular dynamics (PIMD) to include nuclear quantum effects and deliver Bose-Einstein statistics.

Different from the methods based on phonons, the evaluation of electronic energy directly by molecular dynamics is difficult to interpret. However, by comparing different levels of theories, we can quantify the contribution of each term in potential energy Eq. (2.149). For example, the anharmonic effect can be evaluated by comparing the MD that includes the anharmonic effect and the standard MC based on harmonic approximation, as illustrated in Fig. 2.9.

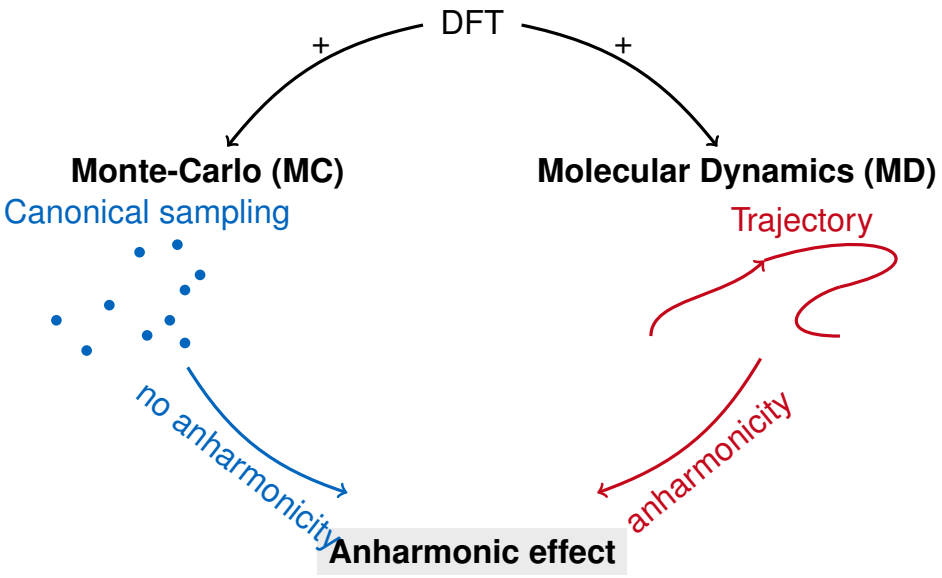

Figure 2.9 Schematic illustration of comparing two methods to quantify anharmonic effect

3 Results and Discussion

3.1 Anharmonic Dynamics in Halide Perovskites

3.1.1 Introduction to structural properties of halide perovskites

Perovskites are a class of compounds with the general chemical formula ABX_3, similar in structure to the mineral $CaTiO_3$. This category of compounds is named after the mineralogist Lev Perovski. HaPs are perovskites where the atom 'X' is a halogen ion (I^-, Cl^-, Br^-). One can view the structure as a cubic array with the monovalent cation A located in the center of corner-sharing BX_6 octahedra. Considering the compatibility of ionic sizes, the stability of perovskite structures is often predicted with Goldschmidt's tolerance factor [93]

$$t = \frac{R_A + R_X}{\sqrt{2(R_B + R_X)}}, \tag{3.1}$$

where R_i is the atomic radius of element i. The tolerance factor assesses how well the cation A can fit into the cavity of BX_6 framework [94]. Typically, a tolerance factor in the range of 0.8 to 1.0 is considered to form stable perovskite structures, while $t > 0.9$ indicates a cubic perovskite structure and $t < 0.9$ may lead to BX_6 octahedral tilting. With the help of the tolerance factor, various halide perovskite compositions have been investigated in the literature. The A-site can be either organic molecular ions as $CH_3NH_3^+$ (MA), $HC(NH_2)_2^+$ (FA), or inorganic atomic ion Cs^+, while the B-site is a divalent metal that can be Pb^{2+}, Sn^{2+}, or Ge^{2+}.

Beyond the classical three-dimensional (3D) HaPs with ABX_3 perovskite structures, a fascinating variety of perovskite-related structures has been discovered. F or example, double perovskites with two different metal cations [95], 2D perovskites characterized by their layered structure with organic cations separating inorganic perovskite layers [96], and mixed-halide perovskites with further control of composition [97, 98]. These investigations into the broader perovskite family open up new possibilities for enhanced stability and tunability.

As discussed in the introduction section, halide perovskites exhibit unusual lattice vibrational characteristics compared to canonical inorganic semiconductors (e.g., Si or GaAs), which motivates a variety of interesting scientific questions for the research community. The dynamic symmetry breaking [99, 100, 17] observed in halide perovskites (HaPs) at high-temperature phases is a critical aspect of their structural behavior [15]. Many HaPs display a high-symmetry average structure at or above room temperature [101, 102, 103]. However, several studies have revealed that the actual, instantaneous atomic geometry

often significantly deviates from this idealized, averaged structure [104, 105, 106]. These local and dynamic structural variations are closely related to octahedral tilting instabilities originated from the structural phase transition. Various structural fluctuations phenomena involving different atom species were studied in the literature: octahedral distortions associated with notable Cs movements [107], two-dimensional overdamped fluctuations of halides [23], octahedral tilting instability enhanced by metal lone-pairs [108], dynamic coupling between A-site and X-site [109, 110], as well as substantial transversal displacements of the halides [111]. This characteristic of a finite-temperature atomic structure that is locally and dynamically disordered yet maintains long-range order, emerges as a fundamental feature across a broad range of HaP materials.

The complicated structural behavior of HaPs sets the stage for understanding their anharmonic vibrational characteristics. The deviation of actual atomic geometries from averaged structures indicates the complex potential surface and interplay of forces within the lattice. This dynamic disorder, manifesting in phenomena like octahedral distortions and overdamped fluctuations, is intrinsically linked to anharmonicity. To figure out the connection between the observed structural instabilities and anharmonic vibrations is crucial for understanding the finite temperatures behaviours in the system.

In this work, we use the $CsPbBr_3$ as a prototypical model system for the broader class of halide perovskite semiconductors. On one hand, it is well-studied in experiments and shares critical properties as other hybrid halide perovskites [112, 100, 113, 23, 114]. On the other hand, it allows a more efficient simulation with fewer atoms. As shown in Fig. 3.1, $CsPbBr_3$ has two phase transitions at 361 K and 403 K, from orthorhombic to tetragonal then to cubic phase [115, 112, 22].

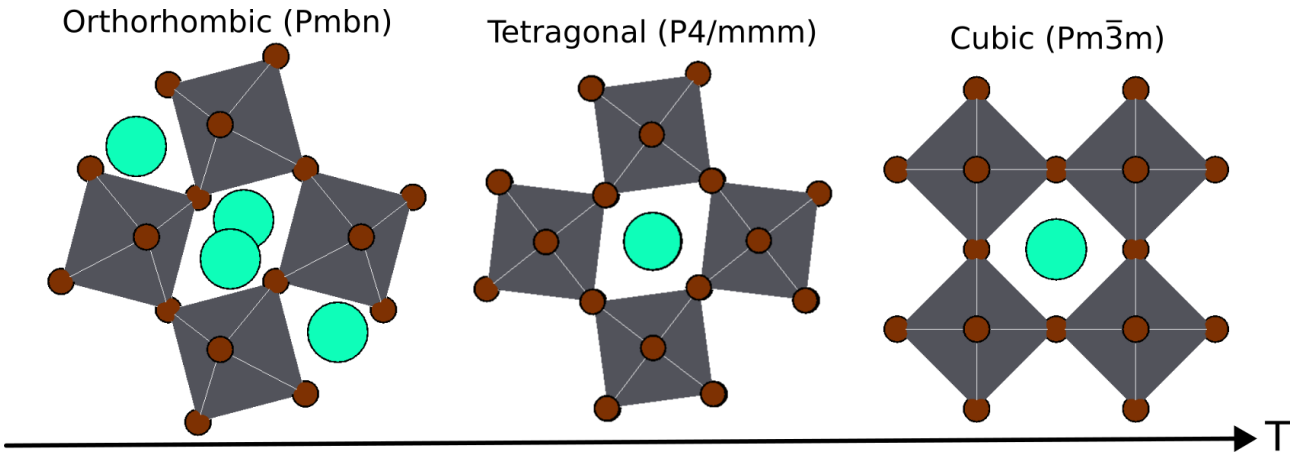

Figure 3.1 Structural phase transition upon heating from orthorhombic, tetragonal, and to cubic phase for $CsPbBr_3$.

3.1.2 Dynamic Instantaneous Structure

As discussed in the previous work of the author [17], it is a challenge for both experimental and theoretical approaches to gain a detailed understanding of the mechanisms driving the physical properties of halide perovskites. Experimentally, the difficulty lies in detect-

ing the process of dynamic symmetry breaking, which means to observe instantaneous rather than average structural properties. This requires techniques sensitive to both temporal and spatial fluctuations. Theoretically, it is is challenging to develop an insight into the finite-temperature dynamics of HaPs, including modeling the temperature-dependent vibrational coupling behavior. This complexity is partly due to the limitations of the harmonic phonon model, which treats the potential up to quadratic terms as discussed in 2.4.2.

To overcome these challenges, we applied MD based on DFT using the Vienna Ab-initio Simulation Package (VASP) [116], using a $4 \times 4 \times 4$ cubic supercell with 320 atoms. The MD simulation was conducted in an NVT ensemble, using the Nosé-Hoover thermostat and applying a time step of 6 femtoseconds to regulate the temperature. At each time step, the DFT calculations were conducted using the projector-augmented wave (PAW) potential [117]. The exchange-correlation functional was addressed using the Perdew-Burke-Ernzerhof (PBE) variant of the generalized-gradient approximation [33], augmented by dispersive interaction modifications based on the Tkatchenko-Scheffler method [118]. This approach is particularly crucial to accurately describe the structural and dynamical characteristics of HaPs [119]. Our computational framework included a plane-wave kinetic energy cutoff set at 300 eV with a single k-point, and an energy convergence criterion of 10^{-6} eV. For the MD simulations, an initial equilibration time more than 2.5 ps was implemented, followed by long production run of nearly 40 ps at a temperature of 425 K and 525 K.

The MD simulation provide detailed insights into the spatial and temporal evolution of local atomic structure as it occurs in cubic phase $CsPbBr_3$. First of all, the displacements of Br and Cs atoms are examined separately. Using the ideal cubic structure as a reference, occurrences of these atomic displacements are captured in 2D histograms across the planes illustrated in the top panels of Figure 3.2 a–c. As explained in Section 2.3.2, we assume that atomic movements in the system are constrained within a effective potential well that average over all the interactions around. Then one would expect the displacement distribution functions to resemble Gaussian distribution peaked at a zero displacement (the ideal lattice position) in harmonic approximation. However, the actual displacement histograms in Figure 3.2 reveal deviations from this harmonic model, suggesting the presence of anharmonic effects or local structural disorder within the $CsPbBr_3$ lattice.

The displacement distribution for Cs atoms, depicted in Figure 3.2a, is centered around zero displacement but deviates from a Gaussian distribution, showing six side peaks. These side peaks indicate the Cs movements towards the face centers of the cubic cell. Note that two peaks along the x-axis are overlapped with the central peak in the figure, so they are not shown. To further investigate the distribution, we plot it as a function of displacement distance $r = \sqrt{x^2 + y^2 + z^2}$ in 1D radial coordinate and assume both the central and side distribution can be approximated by Gaussian distributions. The Gaussian distribution in this coordinate has been discussed in Eq. (2.45) and (2.48). As illustrated in Figure 3.3, using two Gaussian distributions can model the histogram of the central and six side peaks (which appear as one due to cubic symmetry) very well. By the comparison of these two Gaussian distributions, we can see that Cs atoms spend

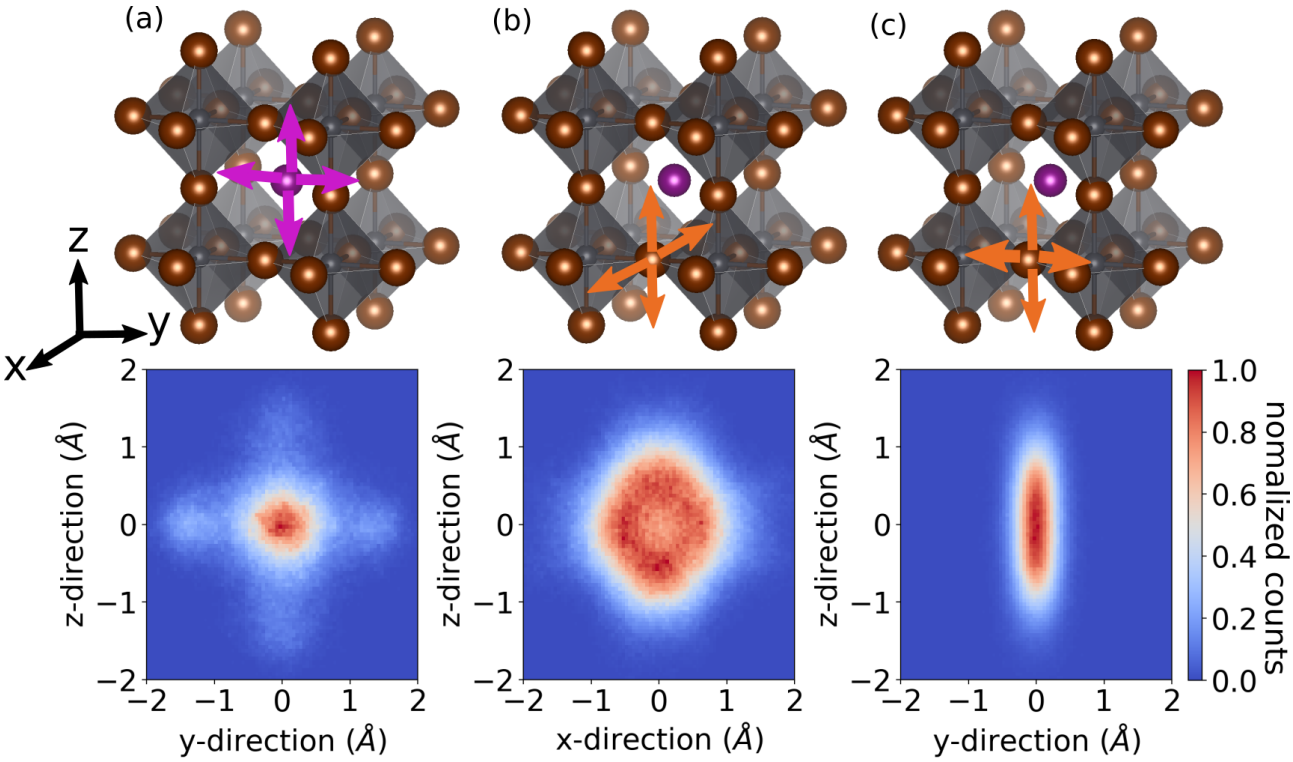

Figure 3.2 The top panels show the schematic representations of atomic displacements studied: (a) Cs displacements on yz-plane, (b) Br displacements on xz-plane, (c) Br displacements on the yz-plane. The bottom panels show the 2D histograms of the corresponding atomic displacements calculated from MD simulation at T = 425 K, where the ideal cubic lattice is used as the reference. Reprinted with permission from Ref. [17]. *Copyright © 2022, American Chemical Society.*

approximately 30% of their time in non-zero positions. In fact, the Cs displacements at side peaks form local structures similar to the orthorhombic phase.

Moreover, the correlation of the nearby Cs atoms is studied in Figure 3.4. By plotting the displacements of two nearest-neighbor Cs in a 2D histogram, one can see that when the first Cs moves (Cs on the left) along the y direction, the second Cs (Cs on the right) tends to move in the opposite direction. These side peaks align with previously discussed head-to-head Cs motions by Yaffe et. al. [100].

The distribution of Br displacements in $CsPbBr_3$ is shown in Figure 3.2b-c. The Br dynamic behavior along (axis y in Figure 3.2) is much smaller than perpendicular (axis x, z in Figure 3.2) to Pb-Br-Pb bonding axis. They are named longitudinal and transversal axes, respectively. In fact, the distribution of longitudinal displacement is found to fit the Gaussian function well, as examined in Figure 3.5. This suggests a more harmonic nature in the longitudinal vibrational modes, contrasting with the anharmonic behavior observed in other displacement directions.

In Figure 3.2b, the distribution of Br transversal displacements, which lie in the plane perpendicular to the Pb-Br-Pb bonding axis, are depicted. This distribution peaks at a nonzero displacement and noticeably deviates from a Gaussian form, a point that is elaborated upon in Figure 3.6. In this figure, Br transversal displacements are plot-

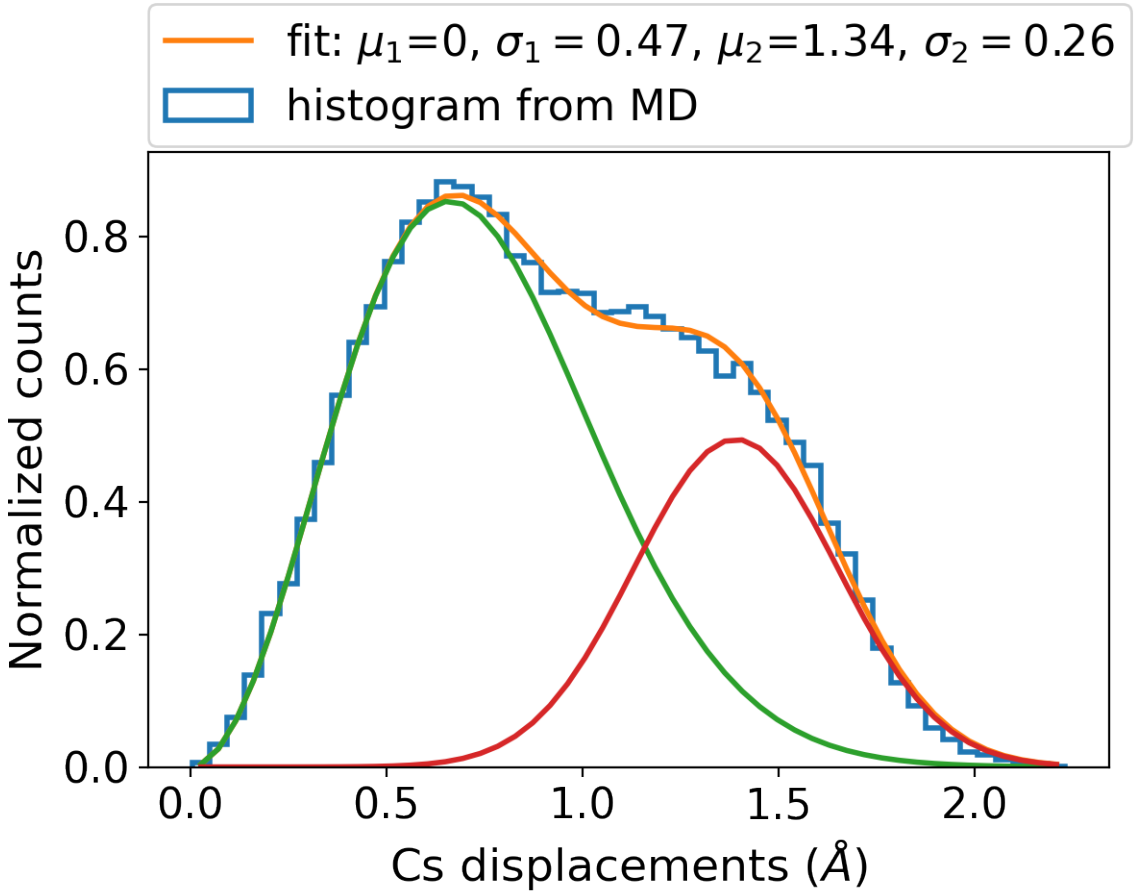

Figure 3.3 Histogram of Cs displacements and the fitting with Gaussian distribution in 1D radial coordinate $r = \sqrt{x^2 + y^2 + z^2}$. The histogram of Cs displacements calculated from MD simulation at 425 K is shown in blue line. Two peak features are fitted with the Gaussian distribution centered around $\mu_1 = 0$ (Eq. 2.45) and $\mu_2 \neq 0$ (Eq. 2.48), which are plotted in green and red lines respectively. They correspond to the central and side peaks in Fig. 3.2. Reprinted with permission from Ref. [17]. *Copyright © 2022, American Chemical Society.*

ted in a one-dimensional radial coordinate, with the Gaussian distribution in the form of $y(r) = C \cdot r \cdot \exp\left(\frac{(r-\mu)^2}{2\sigma^2}\right)$, where C is a constant, μ is the mean value and σ is the standard deviation. As expected, the distribution cannot be fit by a Gaussian distribution with $\mu = 0$. Although a Gaussian function with $\mu \neq 0$ result in better fitting, it is still not perfect. This deviation is significant as it is linked to the soft mode (octahedral tilting mode) in the system, underscoring the complexity of the anharmonicity associated with this mode. The implications of these results for the system's anharmonicity will be explored further below.

After investigating the dynamics of individual atoms, we are interested in the correlation between them. The fact that Cs displacements peak at zero while Br displacements peak significantly away from zero suggests that the most probable nearest-neighbor distance differs from the ideal cubic structure. To examine this, the pair distribution function (PDF) for Cs-Br nearest neighbors is computed. This PDF indicates the likelihood of finding a

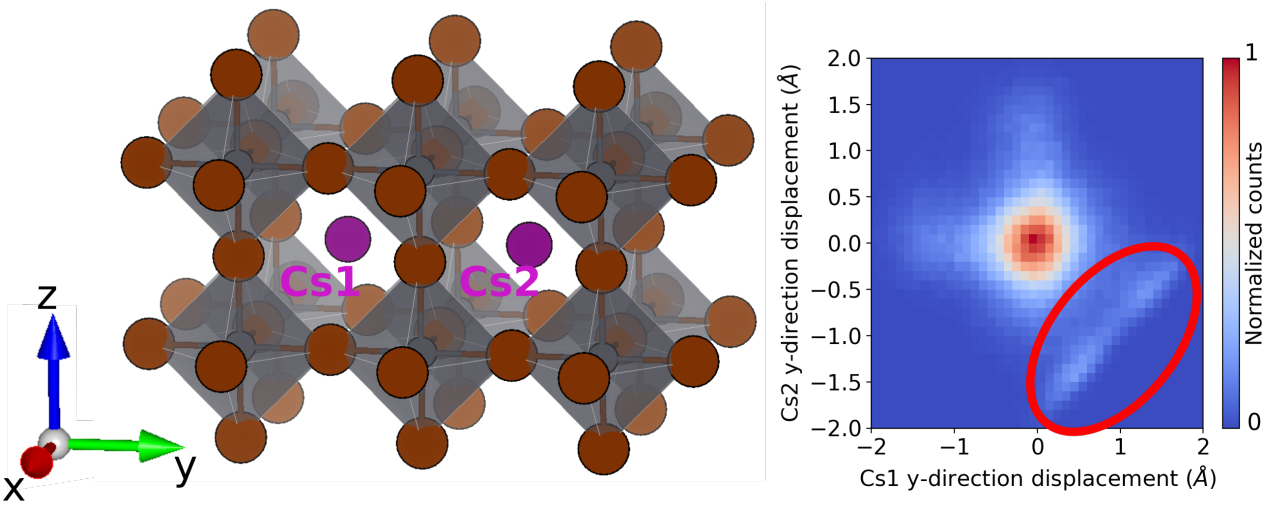

Figure 3.4 The left panel schematically illustrates two nearest-neighbor Cs atoms (Cs1 and Cs2) in the y-direction. The right panel shows the correlation between their displacements with 2D histogram. The red circle highlighted a notable feature, where Cs1 and Cs2 tend to move in opposite directions as reported in the literature by Yaffe et al. Phys. Rev. Lett. 2017, 118, 136001. Reprinted with permission from Ref. [17]. *Copyright © 2022, American Chemical Society.*

Br atom at a certain distance $d_{\text{Cs-Br}}$ from a Cs atom and vice versa, accounting for twelve nominal nearest neighbors Br around each Cs atom (see Eq. (2.40)).

In Figure 3.7, we plot the PDF of nearest-neighbor Cs and Br atoms at two temperatures. Both PDFs reveal significant deviations from the ideal structure's nearest-neighbor distance, with a peak at approximately 3.8 Åcompared to the expected 4.1 Å in the ideal cubic cell relaxed in a static DFT calculation. Additionally, the PDFs exhibit extended tails up to about 6.5 Å, indicating a broad range of Cs-Br distances and highlighting the disorder within the system.

These findings illustrate that the actual Br–Cs distances significantly vary from those predicted by an ideal cubic structure. It shows that the ideal structure, representing an average geometry, does not fully capture the details of Cs-Br interactions. In fact, similar Cs-Br distances are observed in the low-temperature phases, suggesting that these PDF results reflect the local and instantaneous low-symmetry structures present within the cubic phase. An intriguing coupling mechanism in the Cs-Br joint dynamics enhances the formation of the local structures.

3.1.3 Dynamic Cs-Br Coupling in $CsPbBr_3$

To investigate the coupled motion of Cs and Br atoms, we calculate 2D conditional histograms that map the distribution of Br displacements across specific planes, given a predefined condition of a nearest-neighbor Cs atom. As depicted in Figure 3.8, this method offers examination of simultaneous Cs and Br motions within the lattice and their mutual interactions. For instance, if the movements of Cs and Br atoms were independent,

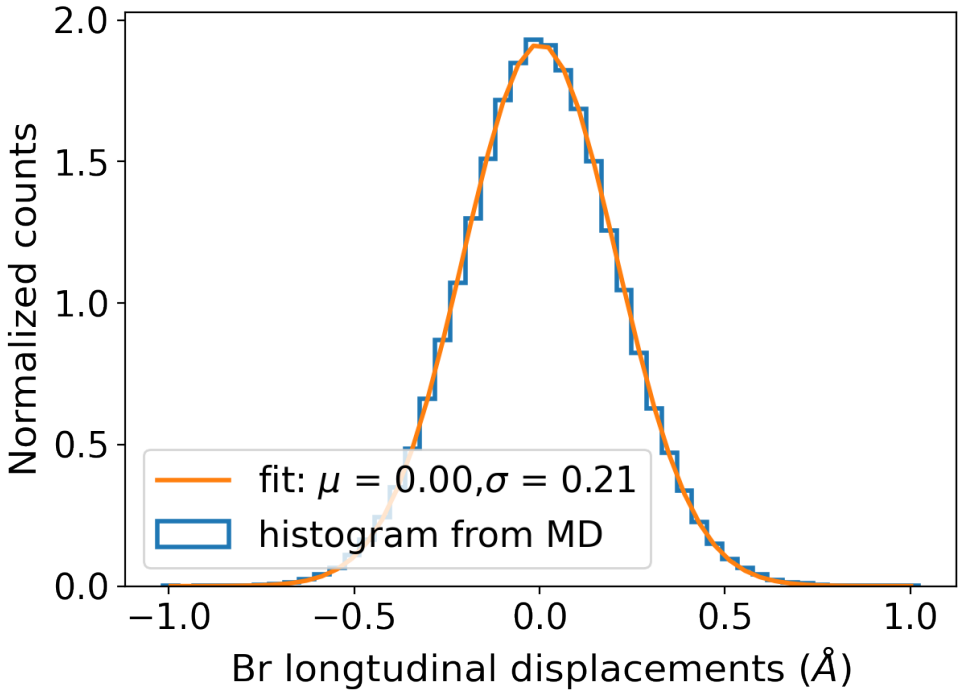

Figure 3.5 Histogram of the longitudinal Br displacement and a fitting with a Gaussian function. The blue line shows the 1D histogram calculated from MD simulation at 425 K and the orange line shows the fitting to a Gaussian function, $A \exp\left(-\frac{r^2}{\sigma}\right)$. Reprinted with permission from Ref. [17]. *Copyright © 2022, American Chemical Society.*

the distribution of Br displacements should remain consistently similar, regardless of the specific Cs displacement condition applied.

In light of our findings (see Figure 3.2a), we set conditions for Cs displacements based on two observed patterns: oscillations around the center of a nominal cubic cell and large displacements along the $\pm x$, $\pm y$, $\pm z$ directions. From these, we derive four distinct scenarios of Cs displacement considering symmetry to use as conditions for analyzing Br displacements. The four scenarios are illustrated in the top panels of Figure 3.9.

- Case I (Figure 3.9a): Cs oscillates around a cubic center with $-0.12\text{Å} \leq x, y, z \leq 0.12\text{Å}$.
- Case II (Figure 3.9b): Cs undergoes a large displacement parallel to the Pb-Br-Pb bonding axis (the $(+x, -x)$ direction in the figure) with $1.27\text{Å} \leq |x| \leq 1.51\text{Å}$ and $-0.12\text{Å} \leq y, z \leq 0.12\text{Å}$.
- Case III (Figure 3.9c): Cs exhibits a large displacement on the plane perpendicular to the Pb–Br–Pb bonding axis toward one nominal nearest-neighbor Br position of the ideal cubic cell (the $(-y, -z)$ direction in the figure) with $-1.51\text{Å} \leq y \leq 1.27\text{Å}$ and $-0.12\text{Å} \leq x, z \leq 0.12\text{Å}$.

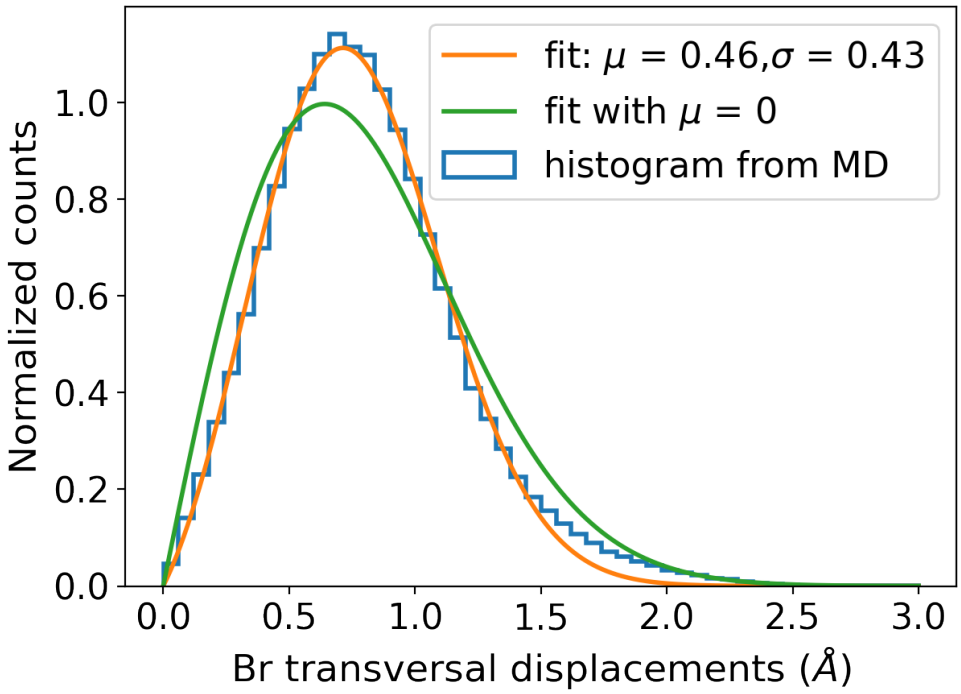

Figure 3.6 Histogram analysis of the transverse Br displacements shows fitting to Gaussian distributions centered at $\mu = 0$ and $\mu \neq 0$. The blue line represents data calculated from MD simulations at 425 K. The Gaussian distribution centered at $\mu = 0$ (green line) fails to align with the MD-generated histogram. However, the Gaussian distribution centered at $\mu = 0.46$ (orange line) achieves a better fitting. Reprinted with permission from Ref. [17]. *Copyright © 2022, American Chemical Society.*

- Case IV (Figure 3.9d): the same as III, but the difference is that Cs moves away from the Br position in the ideal cubic lattice (the $(+y, +z)$ direction in the figure) with $1.27\text{Å} \leq y \leq 1.51\text{Å}$ and $-0.12\text{Å} \leq x, z \leq 0.12\text{Å}$.

We note that scenarios II–IV involve a large displacement of Cs according to the side peaks of Figure 1a.

In scenario I, when Cs oscillates around the center of a nominally cubic cell (see Figure 3.9a), the Br histogram shows a broad distribution with two peaks that indicate two preferred Br positions, which is shown to correspond mainly to an octahedral rotation around one axis in Figure 3.10. In scenario II and III (see Figure 3.9b,c), in contrast to case I, the Br histogram displays only a single peak. The peak signifies a Br displacement over the yz-plane, which corresponds to octahedral rotation around both the y- and the z-axes. In scenario IV (refer to Figure 3.9d), where Cs moves away from a Br lattice position, the resulting Br displacement histogram reveals notably larger displacements and a wider distribution but lacks a distinct peak. We note that the features of the preferred Br motion in this particular scenario possibly suggest that Br interactions are not confined to the Cs within one unit cell. Instead, these patterns imply that Br may be engaging with Cs atoms in adjacent unit cells, indicating a more complex, inter-unit cell dynamic.

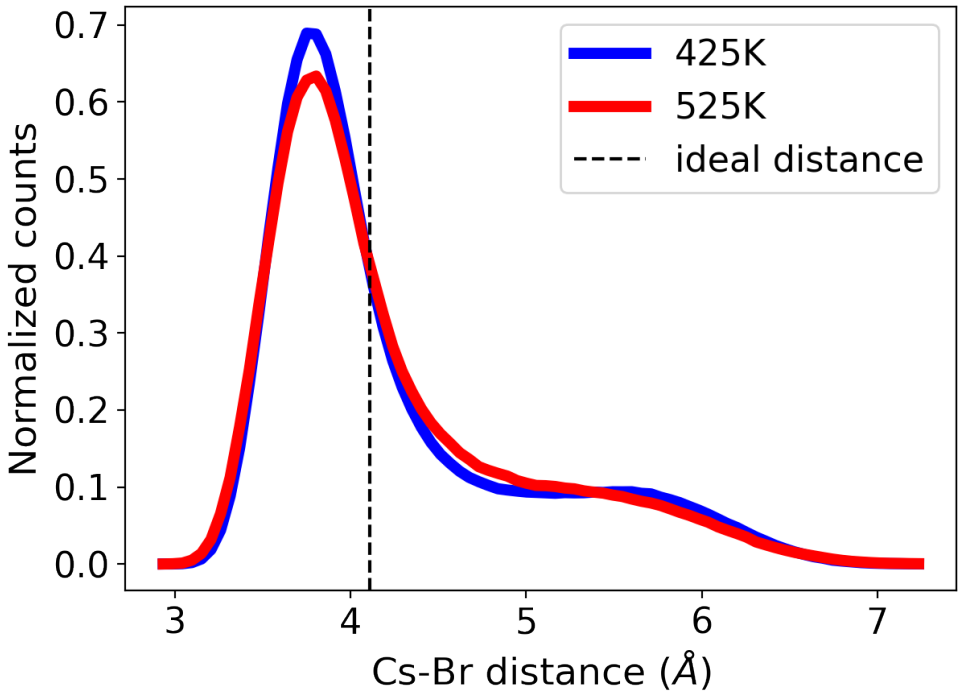

Figure 3.7 Pair-distribution function (PDF) of nearest-neighbor Cs and Br atoms, calculated from MD at T = 425 K (blue) and 525 K (red) as a function of the Cs-Br distance. The dashed vertical line indicates the distance predicted from the ideal cubic unit cell structure of $CsPbBr_3$. The main peaks of both temperatures are deviated from the distance in ideal lattice. Reprinted with permission from Ref. [17]. *Copyright © 2022, American Chemical Society.*

Collectively, our findings reveal an interlocking of Cs and Br displacements, challenging the common assumption that A-site cations in HaPs do not interact with the rest of the lattice. Contrary to this belief, we showed that both the shape and peaks of Br displacement distribution are significantly influenced by the behavior of neighboring Cs displacements, indicating a more interactive and connected behavior within the HaP lattice than previously thought. Moreover, the observed interlocking of Cs and Br displacements suggests the formation of local structures reminiscent of the low-temperature phases within the material. The intricate nature of these local structures adds complexity to the landscape of the potential energy surface (PES) in this system. This complexity is in line with strong anharmonic vibrations in HaPs.

Building upon these findings, we further explore the coupled Cs-Br motion beyond the scenarios of six Cs preferred positions within the nominal unit cell of $CsPbBr_3$ in Figure 3.11. Here, we consider the Cs displacements along all three directions toward face centers and calculate the conditional histogram of Br displacement under these varied Cs conditions. This approach reveals the most probable Br displacements associated with specific Cs movements. The left panel of Figure 3.11 shows the corresponding Br-Cs distances, offering a higher resolution of their coupled motions with an increased number of observational points for Cs positions within the 3D lattice.

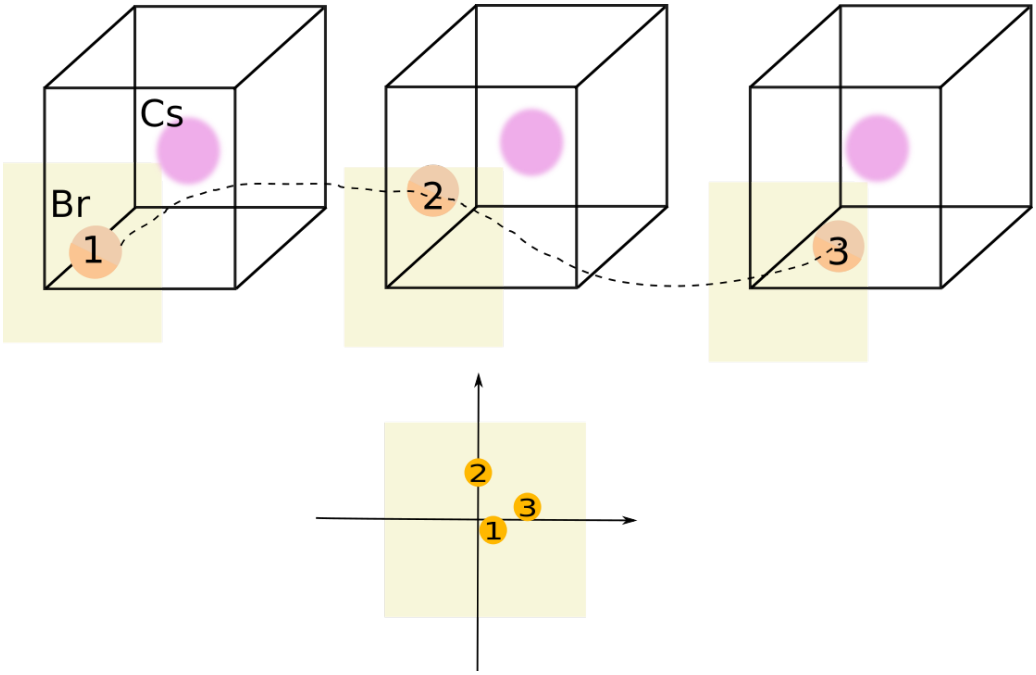

Figure 3.8 Schematic illustration of the Cs-Br conditional distribution. The top panel shows that we collect all the unit cells with Cs moving around the center of the cell in the MD trajectory. The bottom panel shows that we generate a histogram of the position of the Br atom in the plane perpendicular to the bonding axis and plot the distribution.

Notably, these distances can be compared to the PDF (cf. Figure 3.7) and explain the two features discussed above. First, the preferred Cs–Br distance is similar (around 3.8 Å) for most of the considered cases, aligning with the peak observed in the PDF. This observation reinforces the finding that the most frequent Cs–Br distance in the actual structure is shorter than the Cs–Br distance inferred from the ideal cubic lattice. Second, in a few cases along y and z directions, we observed a large preferred Cs–Br distance ranging around 5 Å to 6 Å. This variation is attributed to the large positive Cs displacements on the yz-plane, which prompt Br atoms to prefer the coupling with Cs in the adjacent unit cell, which leads to the long tail observed in PDF.

A symmetry consideration reveals that 8 out of 12 nearest-neighbor Br atoms to a Cs atom generally reside closer, correlating with the shorter Cs-Br distance (depicted as the blue area in the right panel of Figure 3.11). The remaining 4 Br atoms are situated further away, accounting for the longer distance (orange area in the right panel of Figure 3.11). Thus, we separately calculate the Cs-Br PDFs for these two groups of Br atoms. This separation confirms our conditional histogram-based analysis, effectively explaining the observed distribution characteristics in the Cs-Br PDF.

3.1.4 Local Dynamic Disorder and Energy Landscape

Having identified the local coupling in Cs-Br dynamics within $CsPbBr_3$, we now turn our attention to the broader implications on other material properties. We begin by examining the potential energy of Br movements, given their crucial role in the octahedral dynamics

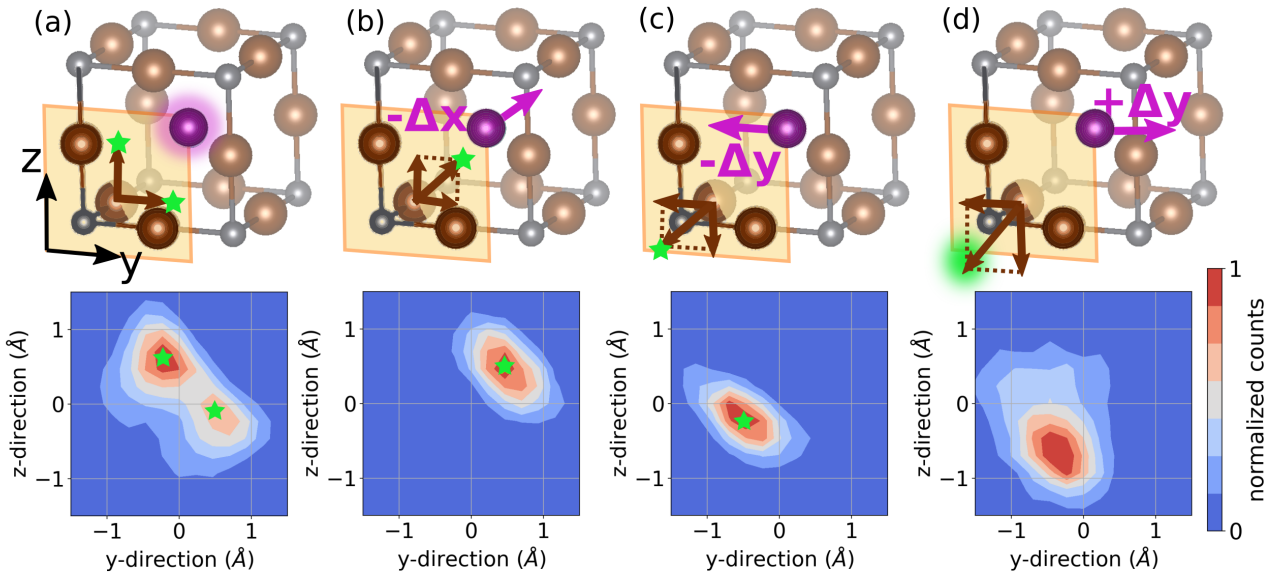

Figure 3.9 2D conditional histograms showing Br atom displacements given that a nearest-neighbor Cs atom displaces in a certain manner during MD simulations at 425 K as explained in Fig. 3.8. The top panels provide schematic representations of Cs atom displacements in violet color, alongside the corresponding preferred Br atom displacements shown in brown. The bottom panels present histograms of Br atom displacements that occur concurrently with the specific Cs movement in the top panels, with green markers indicating the areas where nearest-neighbor Br displacements occur most frequently. Reprinted with permission from Ref. [17]. *Copyright © 2022, American Chemical Society.*

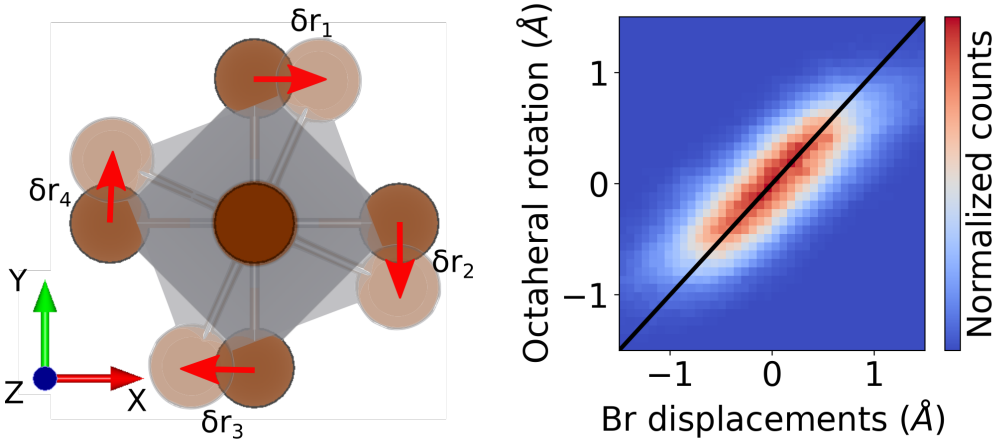

Figure 3.10 The relation of Br displacement and octahedral rotations. Left panel shows the schematic illustration of octahedral rotation, which is quantified by averaging the lateral movements of the four Br atoms in the plane perpendicular to the rotation axis. Right panel demonstrates a significant correlation between the transversal Br displacements and the octahedral rotation. It suggests that Br movements perpendicular to the Pb-Br-Pb bond axis play a major role in driving the octahedral rotation rather than contributing to octahedral distortion. Reprinted with permission from Ref. [17]. *Copyright © 2022, American Chemical Society.*

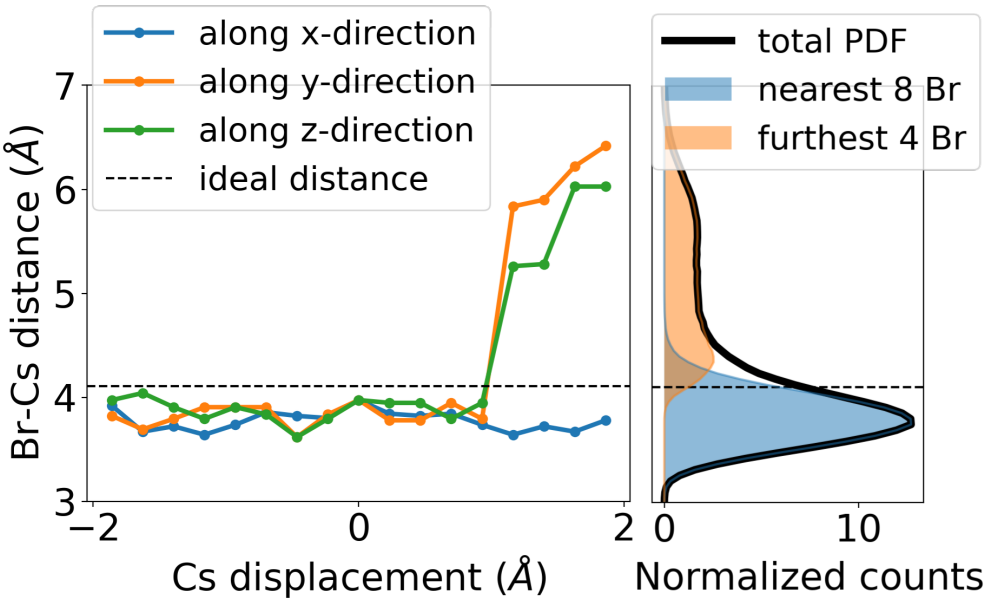

Figure 3.11 Left panel shows the Br-Cs distance with highest occurrence in one unit cell identified in 425K MD for specific Cs displacements. The blue line shows the Cs displacements along x-direction, parallel to the Pb-Br-Pb bonding axis, which corresponds to the motion as Figure 3.9b. The orange and green lines show the Cs displacements along y and z direction, which corresponds to the motion as Figure 3.9c (negative Cs displacement) and Figure 3.9d (positive Cs displacement). The dashed line is the Br-Cs distance of ideal lattice. Right panel shows two parts contributed to PDF at 425K. The blue area is calculated from the Cs and 8 closest neighboring Br atoms in the nominal unit cell while the orange area is calculated from the Cs and 4 remained Br atoms. By comparing these two panels, we confirm the importance of the coupled Br-Cs motion in explaining the PDF. Reprinted with permission from Ref. [17]. *Copyright © 2022, American Chemical Society.*

at finite temperatures and their involvement in forming the electronic states near the band edges. To this end, we consider the Br atoms to move in an ensemble-averaged potential that is due to the interactions with the other atoms in the system. Hence, we perform a Boltzmann inversion (introduced in Section 2.3.2) of Br displacements obtained from MD at T = 425 K and T = 525 K to compute effective potential wells for Br displacements (see Figure 3.12). The comparison of potential wells at these temperatures is particularly enlightening, given that 425 K is relatively close to the tetragonal-cubic phase transition temperature around 400 K of $CsPbBr_3$. For clarity, we focus on Br displacements in a specific direction to obtain a 1D potential, where we take an average of the y- and z-directions, i.e., the two directions perpendicular to the Pb–Br–Pb bonding axis (cf. Figure 3.2, top panel). This effective potential well is termed as “dynamic potential well”. It corresponds to displacements of a single Br atom embedded in the ensemble-averaged potential that is generated by all vibrational excitations present in the system, captured through MD simulation at specific temperatures (425K and 525K). This is contrasted with the “static potential well” from a frozen-phonon approach (orange line in Figure 3.12), which calculates energy changes from specific phonon mode displacements but does not consider dynamic effects of all possible vibrational modes. Specifically, the dynamic effect

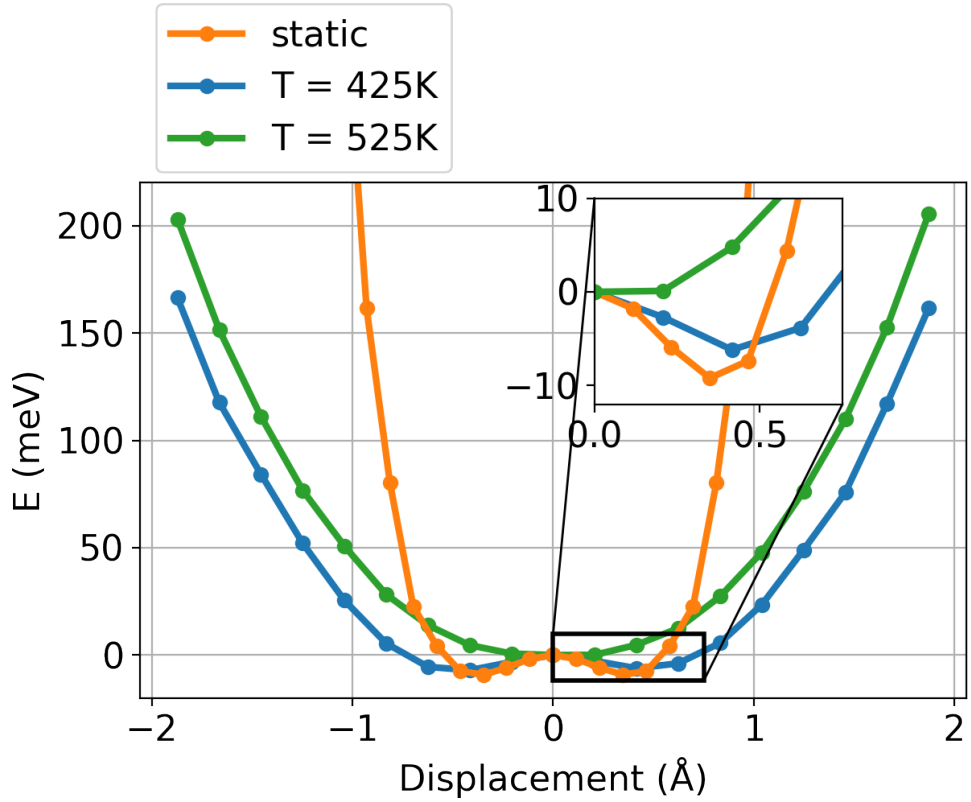

Figure 3.12 Potential energies calculated from two methods. The orange line shows the static potential obtained from frozen-phonon methods. The blue and green lines shows the effective potential using Boltzmann inversion method at 425 K and 525 K. Reprinted with permission from Ref. [17]. *Copyright © 2022, American Chemical Society.*

lead to an important difference between the potentials calculated from two approaches. The dynamic potential wells at both temperatures are found to be shallower compared to the static potential well. It shows that even small energy changes of 150 meV (about $5k_{\mathrm{B}}T$) could lead to relatively large Br displacements of 2 Å. This lowering of total energy comes from the dynamic effect, which not only includes the anharmonic terms of the octahedral tilting phonon mode but also the interactions between other phonon modes, especially those related to Cs displacements.

In addition, we can compare the two dynamic potentials at two temperatures. At T = 425 K, the dynamic potential well is reminiscent of a double-well potential, which is qualitatively similar to the static potential well, although the dynamic well is much shallower (see inset in Figure 3.12). At T = 525 K, the double-well feature disappears. In other words, the behavior of the system is closer to “harmonic" since the temperature effect is more pronounced. One must notice that even the potential well at 525K can not be fitted to a quadratic potential, so it is not a real harmonic. As a result, the depth of the double well is much smaller than the kinetic energy. We have seen that Br motions occurring along the direction perpendicular to the Pb–Br–Pb axis are related to the soft phonon modes driving the $PbBr_6$ octahedral tilting. The emergence and disappearance of the reminiscent double well feature close to the phase transition temperature show the complexity of soft

modes in this material, which is a mix of order-disorder and displacive structural phase transition.

To further investigate the dynamics at 425K and 525K, we calculate the pair distribution function of the nearest-neighbor (NN) Br-Br atoms as illustrated in Figure 3.13. The pair distribution function for the second NN pair, which is not along the bonding direction (Green line in Figure 3.13), is particularly interesting since it relates to the octahedral rotations. The results are plotted in Figure 3.14. Figure 3.14a and Figure 3.14c shows the PDF of 425 K and 525 K respectively. The slight differences in the overall PDF mainly comes from the second NN not aligned along the bond direction (in green). Figure (b)(d) shows the PDF of this part in detail. There are two peaks centered around 4.2 Å and 7.4 Å, which corresponds to the correlated rotations of two nearby octahedra. As the temperature increases, the thermal disorder dominates over the correlated octahedral rotation and leads to a more Gaussian-like PDF. This observation is concurrent to the result in the dynamic potential well and further confirms our finding.

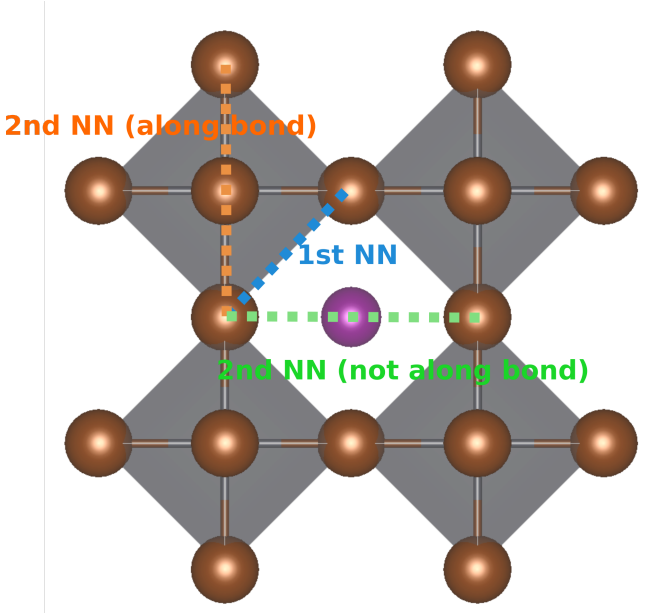

Figure 3.13 Schematic illustration of first and second nearest-neighbor Br-Br pairs. Notice that there are two types of second second nearest-neighbor Br-Br pairs. The orange one is along the Pb-Br-Pb bond direction, while the green one is not. The further analysis of PDF is discussed in Figure. 3.14. Reprinted with permission from Ref. [17]. *Copyright © 2022, American Chemical Society.*

3.1.5 In-Phase Octahedral Tilting Dynamics

We have found above that the octahedral tilting plays an important role in the anharmonic dynamics. In this section, we further investigate the in-phase and out-of-phase octahedral tilting modes at 425 K separately. Specifically, the quantity $\mathbf{R}(t) \cdot \mathbf{u}$ is calculated to obtain the projection of the Br displacement vector $\mathbf{R}(t)$ obtained from MD snapshots at time t, onto the in-phase and out-of-phase octahedral tilting mode $\mathbf{u}$, which are shown in Figure 3.15. The x-direction was set to be the rotation axis, and $\mathbf{R}(t)$ contains the displacement

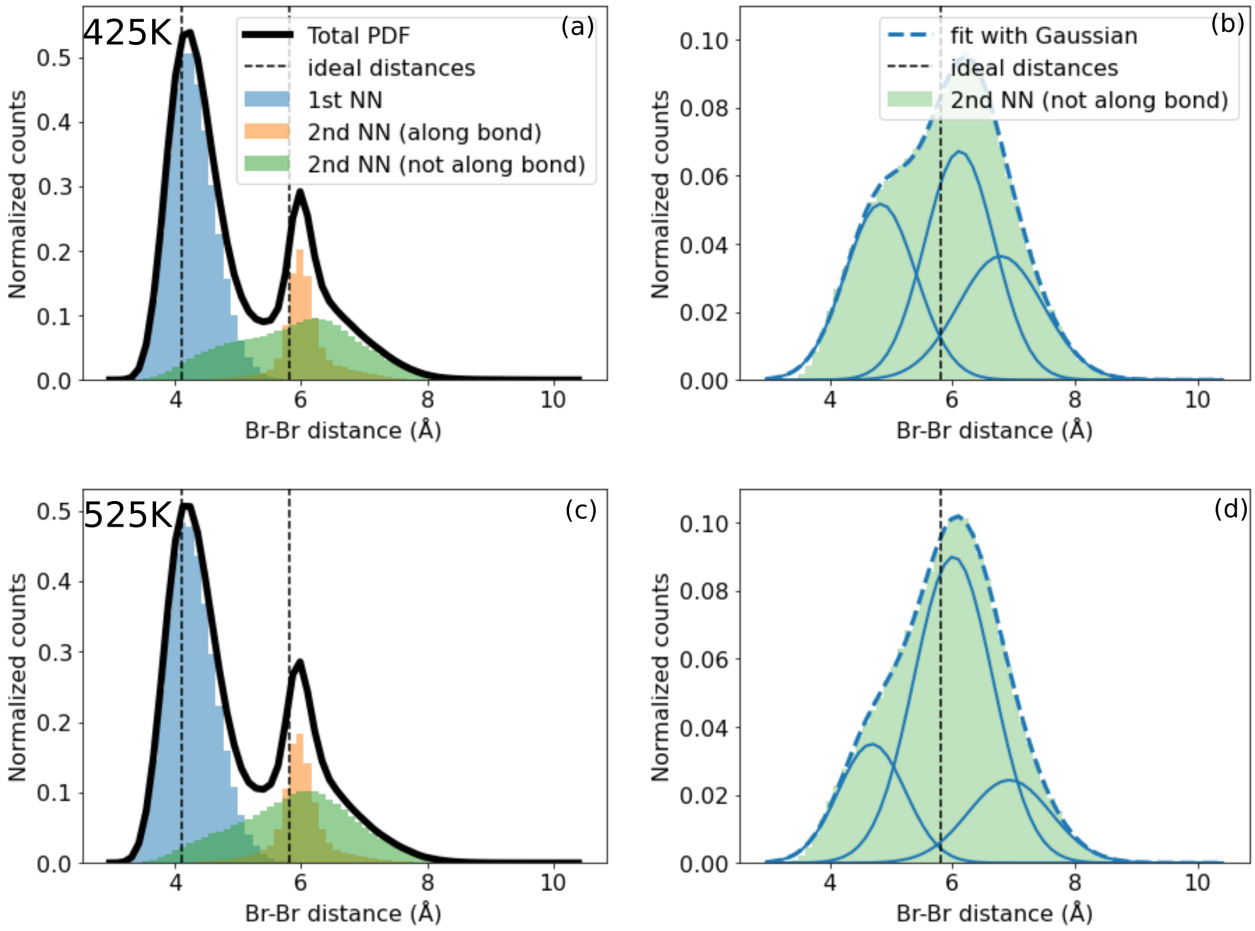

Figure 3.14 PDF of second nearest-neighbor Br-Br pairs. On the left, panels a, c show the first and second nearest-neighbor separately for 425 K and 525 K MD simulation. The Br-Br pairs studied here are illustrated in Fig. 3.13. On the right, panels b, d show the PDF of the second nearest-neighbor Br-Br pair that is not along the bonding direction. They are fitted by three Gaussian functions. Reprinted with permission from Ref. [17]. *Copyright © 2022, American Chemical Society.*

of all Br atoms in the supercell at time t. In Figure 3.16a, we find that in-phase tiltings dominate the cubic phase of $CsPbBr_3$, while out-of-phase tiltings only oscillate around zero. It is related to the structural phase transition from cubic phase to $P4/mbm$ tetragonal phase, which can be seen as freezing in-phase octahedral tiltings, as discussed in the literature for related systems [120, 99, 121, 122].

To probe whether the correlation between Cs and Br atoms plays a role in the contrasting behavior of the in-phase and out-of-phase octahedral tilting mode, we also calculated the cross-correlation of Br displacements involved in octahedral tilting and Cs displacements. The normalized cross-correlation is calculated between the absolute value of in-phase/out-of-phase projections, $|\mathbf{R}(t) \cdot \mathbf{u}| = A(t)$, and the average of the absolute Cs

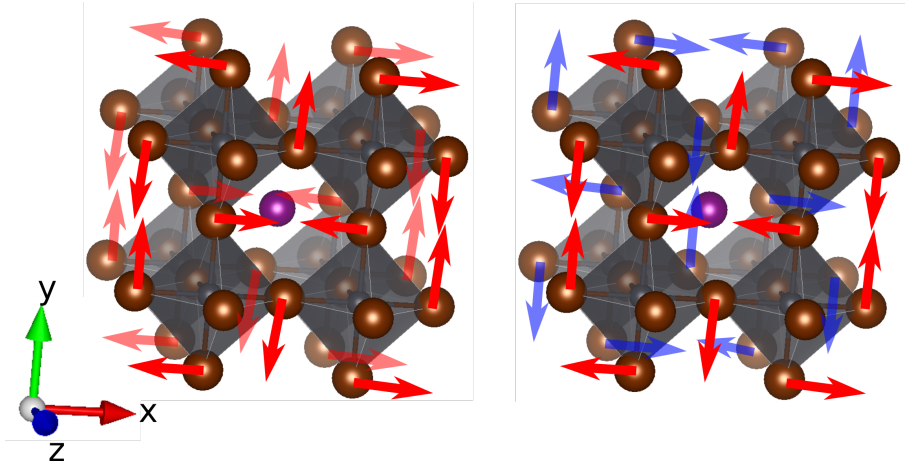

Figure 3.15 Schematic illustration of the in-phase (left) and out-of-phase (right) octahedral rotation modes corresponding to the imaginary frequency at M and R point in reciprocal space. Reprinted with permission from Ref. [17]. *Copyright © 2022, American Chemical Society.*

displacement along y- and z-directions, $B(t)$. The normalized cross-correlation is then written as

$$C(\Delta t) = \frac{1}{N_t} \sum_{t=1}^{N_t} \frac{(A(t+\Delta t) - \bar{A})(B(t) - \bar{B})}{\sigma(A)\sigma(B)} \tag{3.2}$$

where N_t is the total number of time steps. The projected displacements are shown in Figure 3.16b. These findings demonstrate the important role of Cs–Br coupling in the octahedral tilting dynamics of $CsPbBr_3$, which locally and instantaneously distort the HaP geometry significantly away from its average structure.

We have found above that at T = 525 K, the dynamic potential well for the Br displacements loses the double-well features and phonon hardening occurs. To investigate this change through the perspective of octahedral tilting, Figure 3.17 shows the projection of in-phase/ out-of-phase tilting in all three Cartesian coordinates at 525K. Although the out-of-phase tilting has a similar behavior as 425K shown in Figure 3.16, the in-phase tilting modes display a new behavior that they do not always oscillate around a finite amplitude. Instead, the projection amplitudes exhibit low-frequency oscillations between two octahedral tilting directions (positive/negative for the projection). This implies that thermal disorder becomes increasingly more important than correlated tilting motions at higher temperatures. As a result, the results suggest that at higher temperatures, transitions between local minima on the potential energy surface become more frequent, reducing the 'characteristic time' of octahedral tilting to less than the duration of our simulation, which is approximately 40 ps.

3.1.6 Conclusions

In summary, our study focused on the finite-temperature vibrational dynamics of the HaP material $CsPbBr_3$ and assessed local atomic structures. Through first-principles molecular dynamics calculations, we reveal that the actual motions of Cs and Br atoms deviate significantly from an ideal cubic structure. The dynamic coupling of the two species was

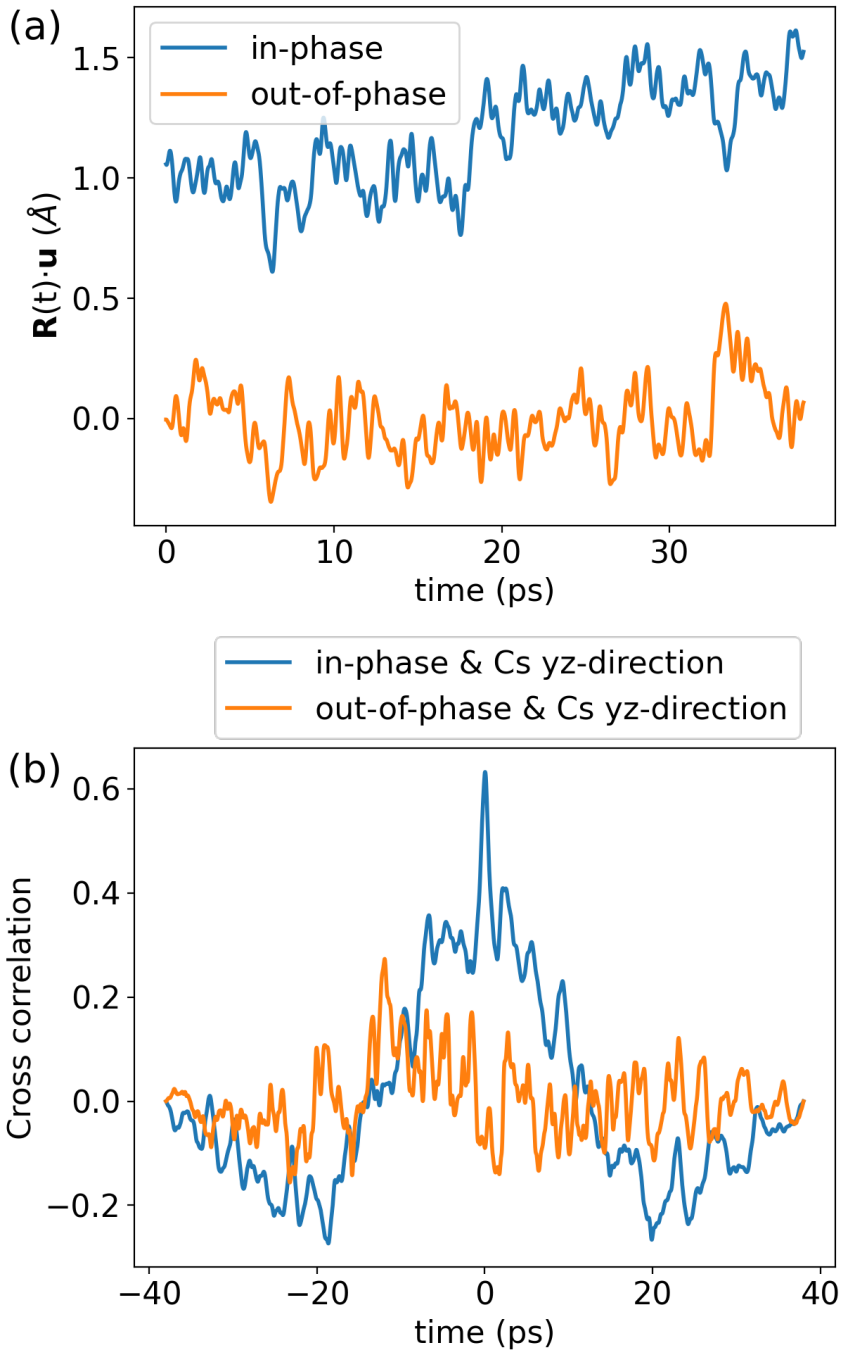

Figure 3.16 (a) Time-dependent projection of Br displacements on the two octahedral tilting modes (see Figure 3.15) around the x-axis during MD simulations at T = 425 K. (b) Cross-correlation of the octahedral tilting modes and the absolute displacement of Cs in the plane perpendicular to the Pb–Br–Pb bond. It is noted that the in-phase tilting exhibits a stronger correlation with the Cs displacements. Reprinted with permission from Ref. [17]. *Copyright © 2022, American Chemical Society.*

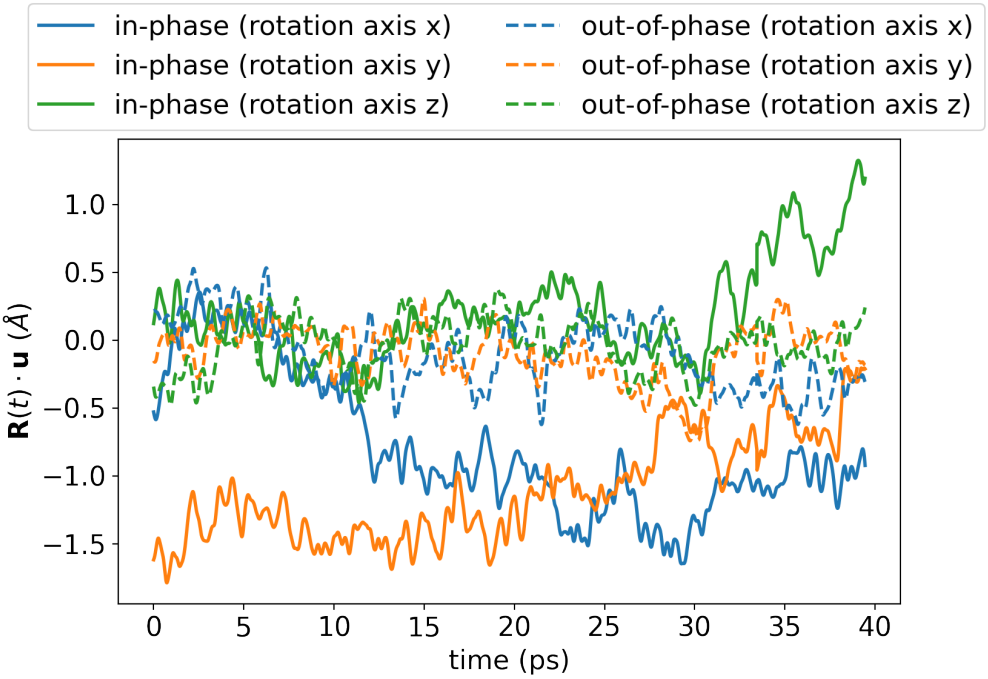

Figure 3.17 Time-dependent projection of Br displacements on octahedral tilting modes around three axes at 525 K MD simulation. The projection of out-of-phase tilting remains around zero, while the in-phase tilting can oscillate around finite quantities (similar to the orthorhombic phase). Reprinted with permission from Ref. [17]. *Copyright © 2022, American Chemical Society.*

demonstrated by the most likely Cs–Br distance being significantly shorter than that inferred from an ideal cubic structure. This coupling is associated with very shallow potential wells for Br motions, occurring in an energy landscape that is both locally and dynamically disordered. By projecting the Br motion to the octahedral tilting modes, we showed that Cs–Br coupling plays an important role in the octahedral tilting dynamics of $CsPbBr_3$. We also compared the dynamic behavior of 425K and 525K to show the special structural phase transition in this system. Since the Br atomic orbitals are known to significantly contribute to the electronic states close to the band edges, this is relevant for the optoelectronic properties of HaPs, which will be investigated in the next section.

3.2 Impact of Anharmonic Dynamics on Band Gap in Halide Perovskites

Note that the results of Chapter 4 are based on the published paper [22], which was done in close collaboration with group member Stefan Seidl (“equal contribution").

3.2.1 Introduction to optoelectronic properties of halide perovskites

The unique structural properties of HaPs can lead to favorable optoelectronic properties that are useful in many applications. HaPs are not only promising candidates for high-efficiency and solution-processable solar cells, but also have potential applications for other optoelectronic applications as well [123], such as light-emitting diodes (LEDs) [124, 125], photodetectors [126], and lasers [127].

The rapid developments in HaPs optoelectronic devices arise from their remarkable properties. First of all, HaPs possess suitable band gaps for sunlight absorption. The band gaps of typical HaPs are around 1.5 eV, which aligns well with the solar spectrum’s maximum intensity, allowing for optimal absorption of visible light. In contrast to Si, HaPs also have a direct or close-to-direct band gap that makes the absorption more efficient. Besides their ideal band gap for solar cells, HaPs exhibit exceptional tunability of band gap from 1.5 to 3.2 eV by adjusting halide anions and the A-site cations mixing ratio [128, 129].

Another notable property is their high absorption coefficients with sharp optical absorption edges. The Urbach energy can reach 15 meV for $CH_3NH_3PbI_3$ perovskites [130]. The high absorption coefficients imply that they are available for thin film devices, which have lower costs and more flexibility in application. The sharp absorption edge not only ensures the efficient absorption of light in solar cells but also contributes to the high color purity of LEDs [131].

Furthermore, the long carrier diffusion length is another desirable feature that is particularly important for solar cell technology. The diffusion length measures how far charge carriers travel before they recombine. Long diffusion length ensures that the charge carriers can reach the electrodes and contribute to the electric current. In HaPs, the diffusion length could reach micrometer [132]. The diffusion length is a combination of two other electronic properties: carrier mobility and lifetime. HaPs have relatively good carrier mobility that can reach hundreds of cm^2/ Vs at room temperature [133, 134] and charge carrier lifetime exceeding 15 μs [135]. In addition, the exciton binding energies are relatively small compared to room-temperature thermal energy [136], which leads to efficient separation of charge carriers in solar cells. Specifically, the free charge carriers will be generated without too much energy loss at room temperature.

While these optoelectronic properties enhance their efficiency in photovoltaic (PV) applications, the relationship between these properties and dynamics are still extensively studied [137, 15, 138]. Several models have been proposed to demonstrate this coupling between structure and function. For example, the octahedral rotation corresponding to the low-frequency imaginary phonon modes could influence the band gap [21, 23]. The

dynamic shortening of disorder potential was shown to lead to a small Urbach energy [18, 111]. The special temperature dependence of carrier mobility $\mu \propto T^{-1.5}$ can be explained by the dynamic disorder effect [19]. Lattice fluctuations cause charge carriers to become self-trapped in large polaronic states that can influence the charge recombination [139]. The inorganic lattice and electronic interband polarizations are major contributors to exciton screening [137].

Among these optoelectronic properties, the fundamental band gap is a key quantity for light-matter interactions in semiconductor optoelectronics [140, 13]. In the single-particle perspective, it is defined as the energy gap between the valence band maximum and the conduction band minimum. Since real-world devices are operated at room temperature, it is essential to understand the influence of thermal effects on the band gap and other properties. However, there is an ongoing debate on the leading thermal effects that determine band gaps of HaPs, which centers on factors like higher-order electron-phonon interactions [24, 141], thermal lattice expansion [142, 143, 144], and vibrations [89, 23, 21]. Specifically, the anharmonic vibrations, including pronounced octahedral tilting dynamics and large-amplitude atomic displacements, play an important role in their dynamics as shown in Chapter 3.1.1. Therefore, we will investigate the impact of anharmonic vibrations on the fundamental band gap of HaPs in this section, to deepen the understanding of both experimental measurements and theoretical predictions.

3.2.2 Failure of static structure picture

We start with the experimental measurements of the temperature dependence of $CsPbBr_3$ band gap in three phases. Figure 3.18a shows the reflectance spectra between 300 K and 560 K of a $CsPbBr_3$ single-crystal [1]. The peaks around 2.4 eV are associated with optical absorption energy, which is approximately equal to the band gap energy because the exciton binding energy of $CsPbBr_3$ (on the order of a few tens of meV [145]) is small compared to the fundamental band gap. As a result, we can view it as a proxy for the temperature development of the band gap.

Notably, it is shown that the band gap change in the measured temperature range is mild. Despite the measurement going across the orthorhombic-tetragonal and tetragonal-cubic phase transitions at 361 K and 403 K respectively, the thermal effects on the spectra are relatively subtle. These observations align with prior experimental studies [146], yet they significantly differ from the predictions of static theoretical calculations.

The static structures of cubic and orthorhombic phases are shown in Figure 3.18b, which were relaxed in DFT. Our calculation reveals a notable reduction in the band-gap value, by as much as 0.7 eV, when transitioning from the orthorhombic to the cubic structure, which aligns with results from prior research [147, 148]. The band gaps were calculated with PBE functional [33], augmented by dispersive corrections of Tkatchenko-Scheffler (TS) scheme with iterative Hirshfeld partitioning of the charge density [118, 149], including the effect of spin-orbit coupling (SOC) implemented in `VASP`. A plane-wave energy cutoff of

[1] Measured by Guy Reuveni and Sigalit Aharon in the group of Omer Yaffe at Weizmann Institute of Science

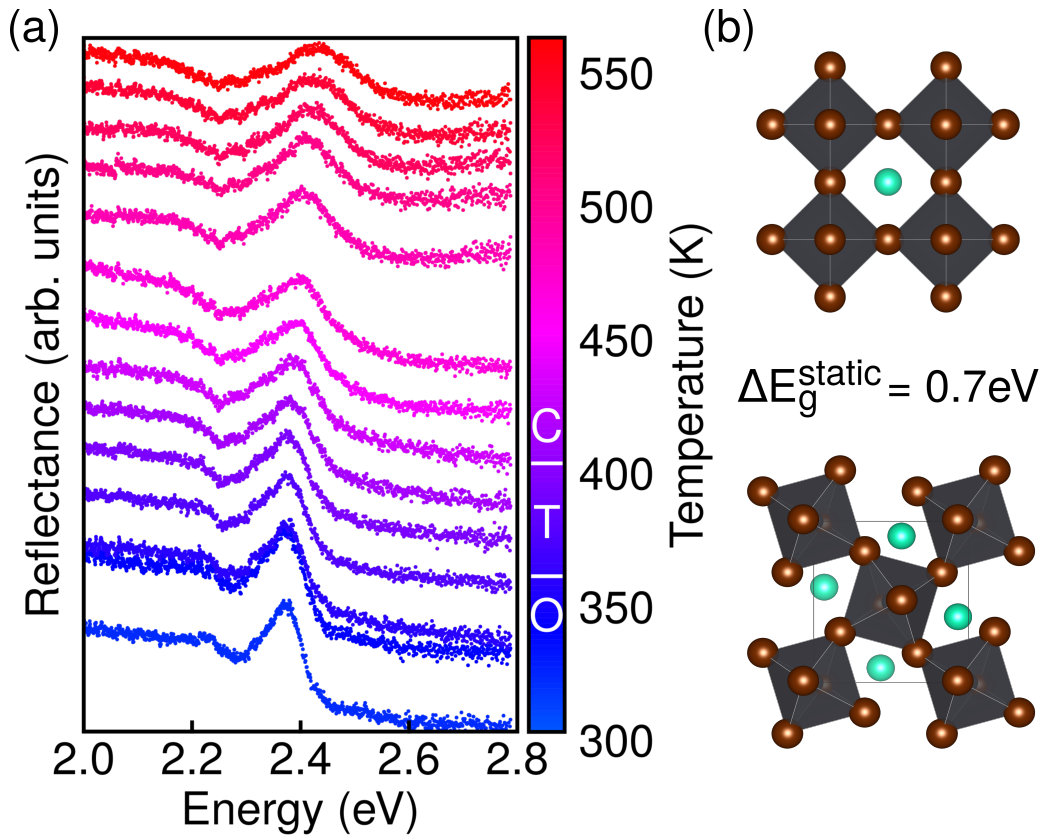

Figure 3.18 Panel (a): Reflectance measurements of $CsPbBr_3$ single crystals of varying temperatures across three phases. The spectrum is measured with the interval of 20 K temperature increments, which is shown by the color bar on the right. The white horizontal lines in the color bar mark the temperatures of phase transitions reported in the literature [115]. Panel (b): Schematic diagrams of $CsPbBr_3$ structure in cubic and orthorhombic phase. ΔE_g^{static} is the changes in band gaps, which are determined through static DFT calculations for both the orthorhombic and cubic structures. Reprinted with permission from [22]. *Copyright © 2023 by the American Physical Society.*

400 eV, energy convergence threshold of 10^{-6} eV, and an 8 $\times$ 8 $\times$ 8 Γ-centered k-grid (6 $\times$ 4 $\times$ 6) were used for the cubic (orthorhombic) phase.

The discrepancy between experimental observations and theoretical predictions underscores the importance of including dynamic effects for the finite-temperature behavior of HaPs. This motivates us to include thermal effects for a set of temperatures to examine the thermally-induced band gap renormalization.

3.2.3 Temperature-dependent band gap study with two approaches

Two methods are employed to investigate the thermal effect on band gaps: the Monte Carlo (MC) method (see Section 2.5.3) and the molecular dynamics (MD) method (see Section 2.3).

We begin with the MC method, which includes the full-order electron-phonon coupling effect but treats the atomic vibrations within the harmonic approximation. It provides an

ensemble average of band gaps with stochastic samples of atomic displacements according to pre-calculated phonon modes. Specifically, the phonon modes were calculated at Γ point with finite difference method implemented in VASP with 160 atom supercell. Note that we ignored the phonon modes with imaginary frequency in the procedure. We applied it to both cubic (4 $\times$ 4 $\times$ 2) and orthorhombic phase (2 $\times$ 2 $\times$ 2), while excluding the intermediate tetragonal structure, which only exists in a very narrow temperature range. The kinetic-energy cutoff and energy convergence threshold are set to 400 eV and 10^{-8} eV. The integration in reciprocal space was carried out over a 3 $\times$ 2 $\times$ 3 k-grid for the orthorhombic and a 2 $\times$ 2 $\times$ 4 grid for the cubic phase. Since the phonon frequency and eigenmodes are obtained with harmonic approximation, the MC method does not include the anharmonic effect intrinsically. Then, 100 distorted structures were generated for six temperatures. The fundamental band gap was calculated at different temperatures as a statistical average of them, where we employed a kinetic-energy cutoff of 300 eV, an energy convergence threshold of 10^{-4} eV, and a Γ centered k-grid of 2 $\times$ 2 $\times$ 2 for orthorhombic, and 2 $\times$ 2 $\times$ 4 for cubic $CsPbBr_3$. We included the effect of SOC in these self-consistent DFT calculations as well.

The results are represented by the blue dashed line in Figure 3.19. Notably, it underestimates the band gaps in the cubic phase and leads to a jump of 0.4 eV between the orthorhombic at 325 K and cubic phases at 425 K. However, the difference is smaller compared to the difference between static structures and experimental measurements in Figure 3.18b. Although we yield an improvement by considering thermal effects, the results are still far from the experimental observation showing a mild shift (Figure 3.18a). In conclusion, the major discrepancy we had in Figure 3.18 is not fully solved within the framework of harmonic approximation.

To explain the experiment trend of the temperature-dependent band gap, we next go beyond the harmonic approximation with the MD method. We conducted DFT-based MD calculations employing the canonical (NVT) ensemble with an energy cutoff of 300 eV. For the cubic phase, we utilized a 1 $\times$ 1 $\times$ 2 k-grid, and for the orthorhombic phase, a single k-point was used. The systems were equilibrated for 8 ps followed by extensive production runs of 42 ps to sample 100 configurations at specified temperatures. The band gaps were then calculated by averaging these sampled configurations using the idea of ergodicity, once again using the PBE DFT-functional with SOC using the same set of parameters in VASP. As MD simulations do not rely on harmonic approximation and provide an exact framework for atomic motions within the Born-Oppenheimer approximation, this approach accounts for vibrational anharmonicity to all orders at finite temperatures.

The results are shown by the red solid line in Figure 3.19. It is worth noting that the MD data capture various key characteristics of the thermal electronic structure in $CsPbBr_3$ we have seen in the experiment (Figure 3.18a): First, in the temperature range between 275 K and 525 K, we find mild changes in the band gap value, which differs by less than 0.1 eV. Second, the band gap around phase transition temperature has a difference that amounts to only 0.1 eV between the cubic phase at 425K and the orthorhombic case at 325 K. They show that it is important to include the anharmonic effect to capture the correct feature of experiments.

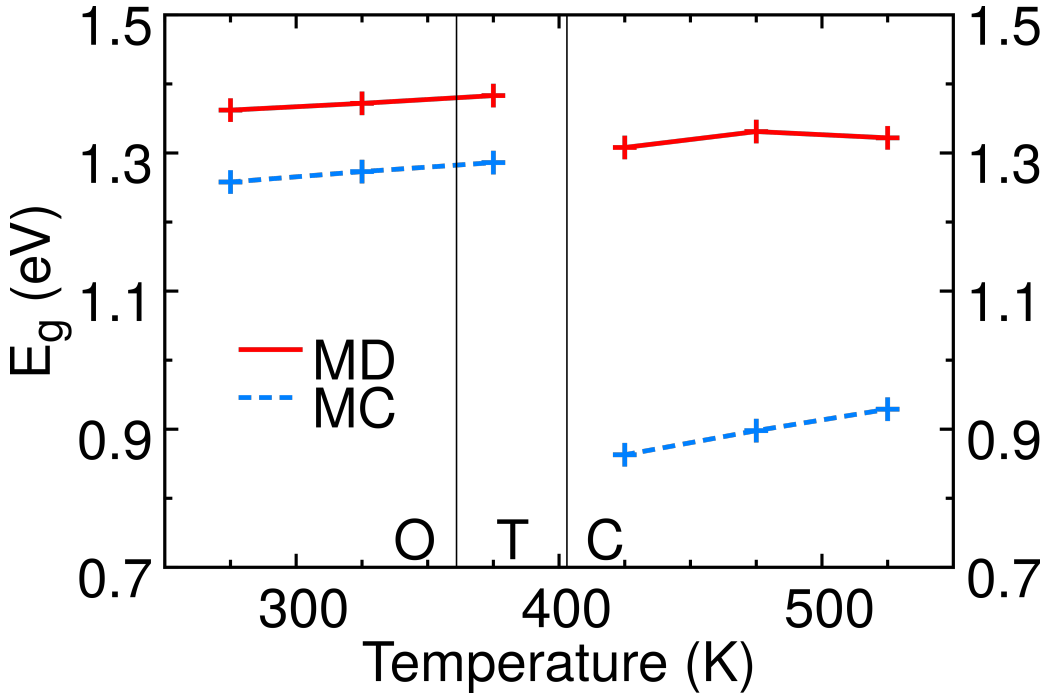

Figure 3.19 Temperature-dependent fundamental band-gap of $CsPbBr_3$. The blue-dashed lines are computed by the MC method (see Section 2.5.3), while the DFT-based MD calculations compute the red lines (see Section 2.5.4). The vertical lines indicate reported phase-transition temperatures [115]. The discrepancies of band gaps from the experimentally measured peak in Figure 3.18 (≈ 2.4) can be attributed to the known limitations of the PBE exchange-correlation functional. Specifically, the band gap values in our calculations are consistently underestimated, a common issue stemming from the inherent band-gap problem associated with semilocal DFT methods. Reprinted with permission from [22]. *Copyright © 2023 by the American Physical Society.*

Furthermore, we are able to extract the precise amount of the anharmonic effect on the band gap by comparing these two methods. As a consistency check, we show the difference is negligible for bulk Si that generally is expected to be fairly harmonic in Figure 3.20. The band gaps are calculated at temperatures of 100 K, 300 K, and 700 K using a Si supercell of 128 atoms. At 700 K, the difference between MC (blue dashed line) and MD (red solid line) is very small (around 0.01 eV). At a temperature range lower than the Debye temperature of 640 K, the differences mainly come from the quantum effects since MC and MD follow Bose-Einstein and Maxwell-Boltzmann statistics respectively. The comparison between the two methods for Si can be contrasted with the large difference seen for $CsPbBr_3$ in Figure 3.19, highlighting the importance of the anharmonic effect in this material.

At 425 K, both the MC and MD methods indicate an increase in the band gap compared to the static calculation for the cubic phase. The MC method, accounting for dynamic fluctuations of harmonic motions, enlarges the band gap by approximately 0.3 eV. In contrast, the MD method, which additionally considers anharmonic motion, leads to a more substantial increase of about 0.7 eV in the band gap at this temperature in the cubic phase. Consequently, anharmonic effects contribute nearly 0.5 eV to the band gap renormalization at 425 K. This anharmonic contribution to the gap exceeds the pure-phonon contribution

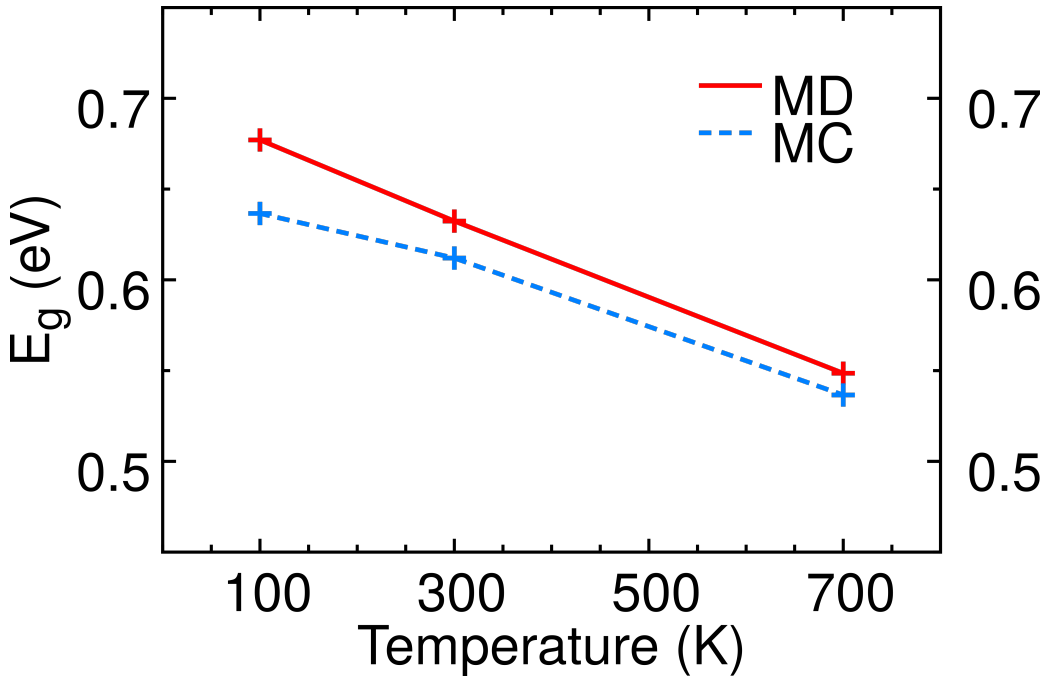

Figure 3.20 Temperature-dependent band gap of bulk Si. The blue-dashed lines are computed by the MC method (see Section 2.5.3), while the DFT-based MD calculations compute the red lines (see Section 2.5.4). The difference between the two methods is small since Si is a system with weak anharmonicity. Reprinted with permission from [22]. *Copyright © 2023 by the American Physical Society.*

and largely resolves the discrepancies of Figure 3.18. The dominance of the anharmonic effect on the band gap can be further established through a comparison of its magnitude ($\approx$ 0.5 eV) to significant effects of SOC ($\approx$ 0.8 eV) and approximate exchange-correlation treatments ($\approx$ 0.9 eV) that are commonly known for $CsPbBr_3$ and other HaP variants.

Additionally, within the temperature range corresponding to the orthorhombic phase, the discrepancies between the band gaps determined by MC and MD methods are noticeably smaller, suggesting a more harmonic character in the orthorhombic phase. Furthermore, it is observed that the MC and MD band gap values converge with increasing temperature, implying that the anharmonic effects are most pronounced around the phase transition temperature. This characteristic can be attributed to the temperature-dependent nature of overdamped dynamics, a topic that will be elaborated upon in the following chapter.

3.2.4 Free energy and estimation of anharmonic effect of one phonon mode

To better understand the microscopic mechanism driving the temperature-dependent evolution of the band gap, we examine the free energy changes linked to transversal Br displacements (refer to Fig. 3.21a). This analysis applied Boltzmann inversion (see Section 2.3.2) on sets of structures generated by several approaches, including MD trajectories in the orthorhombic phase at 325 K, MD trajectories in the cubic phase at 425 K, and MC-generated structures of the cubic phase at 425 K. The obtained effective potential can be

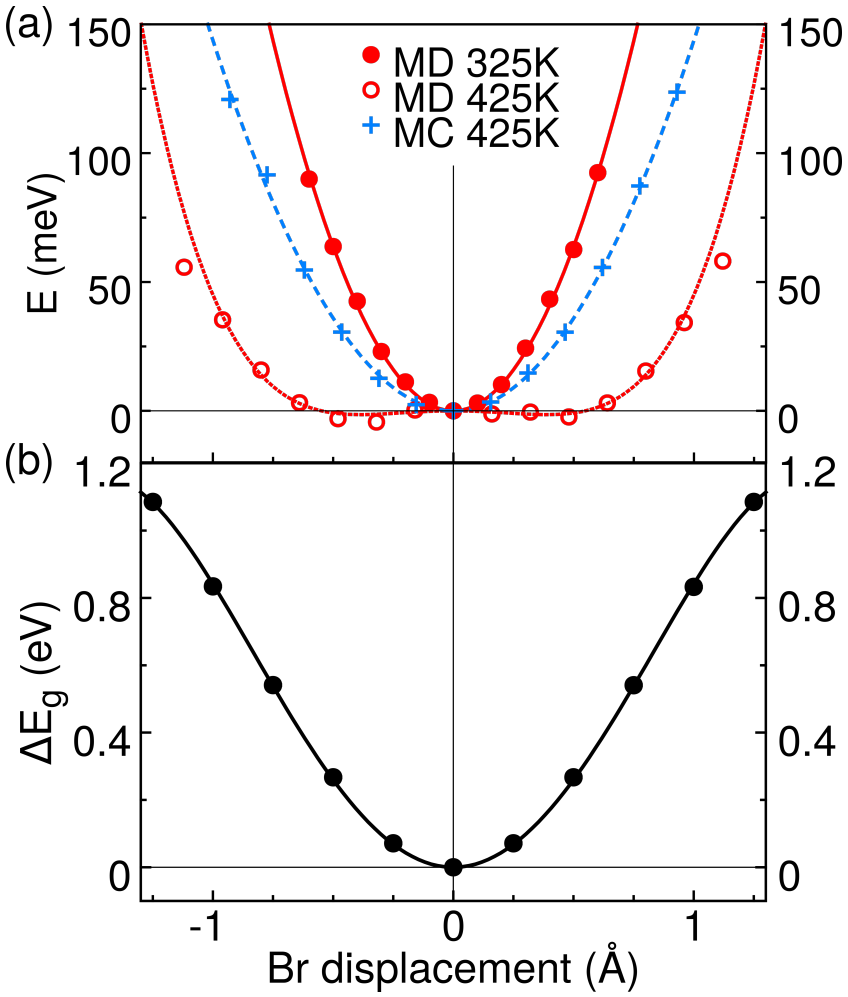

Figure 3.21 (a) Changes in effective potential energy related to the transversal movement (perpendicular to the Pb-Br-Pb bond axis) of a Br atom in $CsPbBr_3$. The red dots are derived from Boltzmann inversion of MD trajectories for the orthorhombic phase at 325K (represented by red disks) and for the cubic phase at 425 K (represented by red circles). The blue crosses are derived from Boltzmann inversion of MC data at 425 K. The colored lines indicate fits: quadratic functions for the orthorhombic MD and cubic MC data, and a function of the form $ax^4 + bx^2$ for the cubic MD data. The zero point on the x-axis aligns with the time-averaged position of a Br atom. (b) Changes in the band gap, ΔE_g as a function of transversal displacement of Br. The set of displaced structures is generated from the phonon eigenvector that is associated with the octahedral-tilting phonon mode at the M-point in reciprocal space (see Figure 3.22). Reprinted with permission from [22]. *Copyright © 2023 by the American Physical Society.*

directly compared to the quadratic potential with harmonic approximation and characterize atomic vibrations of different methods and temperatures. We focus on the transversal motions of Br displacements, as highlighted in the previous chapter, where we discussed the significant impact of octahedral tilting dynamics on the electronic structure of HaPs. Notice that the Br atom in the orthorhombic phase has lower symmetry and here only Br on the $a - b$ plane is used.

In the orthorhombic phase, the free energy has a harmonic profile, with thermal atomic displacements being relatively small. Conversely, in the cubic phase, the behavior is

anharmonic, characterized by a shallow and broad potential that deviates from a quadratic form. This suggests a multitude of possible configurations within the multi-well potentials. It's important to note that the free-energy changes observed in the MC approach are intrinsically harmonic, as they are derived from harmonic phonon modes. Interestingly, free-energy changes associated with Br motion show marked differences between the orthorhombic and cubic phases of $CsPbBr_3$, even though the average band gap remains relatively similar in both phases. It is important to note that the x-axis in this analysis corresponds to the time-averaged position of the Br atom. If we consider the orthorhombic phase as a transformation from the cubic structure through octahedral rotation around multiple axes, then the quadratic-like potential well in the orthorhombic phase would be positioned at a non-zero point on the cubic axis. This observation suggests that the system adopts lower symmetry structures in the cubic phase, which will be discussed in the next section.

Having identified the transient octahedral tiltings in the cubic phase of $CsPbBr_3$, we next focus on how vibrational anharmonicity influences the band gap renormalizations associated with these tiltings. Establishing a connection between the dynamic band gap variations observed in the MD simulations and specific phonon modes is challenging, primarily because purely harmonic phonon modes do not account for anharmonic effects. For instance, when calculating the band gap changes associated with a particular phonon mode, not only are the higher-order terms in the potential energy typically overlooked, but the interaction of that mode with other concurrent vibrations in the system is also often disregarded.

The following simplified model is constructed to provide qualitative insight into the anharmonic effect. First, we extract the phonon eigenvector of an octahedral tilting mode in cubic $CsPbBr_3$ using harmonic phonon calculations and the `phonopy` package [150]. This particular mode at the M point in the Brillouin zone of the cubic phase is imaginary and is not included in the standard MC approach. It is marked as the red point in Figure 3.22. Within the harmonic approximation, it has an imaginary frequency and represents a phonon mode involved in the in-phase octahedral tilting around one axis, as shown in Figure 3.15, that lowers the symmetry of the material. This provides us with a set of structures with atomic displacements corresponding to this phonon mode. Next, we compute the change of the band gap, $\Delta E_g(x)$, as a function of transversal Br displacement, x, for this particular phonon mode using DFT (see Figure 3.21b). An ensemble integration of these band gap changes can now be performed classically, using either the MC or MD free-energy profile (see Figure 3.21a). Therefore, the total change in the band gap is determined by the equation:

$$\Delta E_g^{\text{tot}} = Z^{-1} \int dx \Delta E_g(x) \exp\left(-\frac{V_i(x)}{k_B T}\right), \tag{3.3}$$

where $Z = \int dx \exp(-V_i(x)/k_{\mathrm{B}}T)$ serves as the normalization constant (partition function). The index i denotes the use of either the MC or MD free-energy profile of Figure 3.21a for the integration, with T set to 425 K.

Note that this model is predicated on the assumption that the Br displacements are solely attributed to the phonon mode under consideration. Utilizing this simplified approach, we

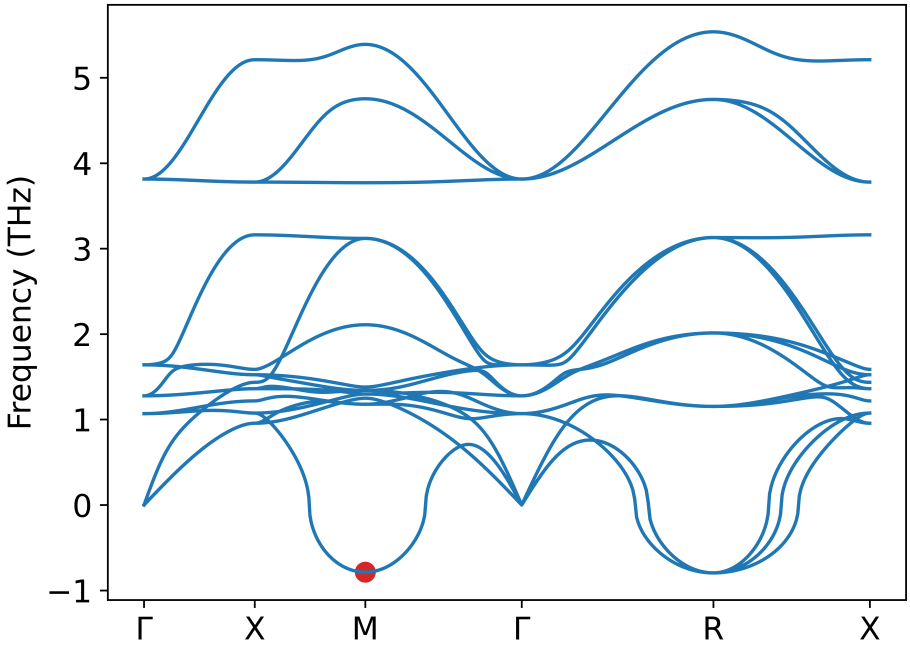

Figure 3.22 Phonon dispersion relation of $CsPbBr_3$ in the cubic phase. The calculation is implemented with the package Phonopy [150]. The imaginary mode considered in the model calculations presented in Figure 3.21, is marked in red. Note that this particular mode corresponds to in-phase octahedral tilting and is not included in the MC method. Reprinted with permission from [22]. *Copyright © 2023 by the American Physical Society.*

calculate a total band gap change of 0.17 eV for the MC and 0.28 eV for the MD scenario. The harmonic nature of the MC free-energy profile, contrasted with the anharmonic profile derived from MD, suggests that anharmonic fluctuations lead to more pronounced dynamic changes in the band gap. Our model can be viewed as accounting for the low-frequency peak around 1.5 THz observed in the gap spectral function alone, as shown in Figure 2.8. A more accurate estimation could be achieved by considering the electron-phonon coupling strength for each phonon mode in the full range of gap spectral function. While the structural details of the anharmonic effect are specific to HaPs, we hypothesize that anharmonic effects play a significant role in the broader class of anharmonic semiconductors.

3.2.5 Microscopic explanation

We have characterized the anharmonic dynamics with local disorders in the last chapter and seen that they have a significant effect on the temperature dependence of band gaps above. Now, we want to build the connection between the strong anharmonic effect on the band gap and the atomic motion from the microscopic perspective. Specifically, the system transiently exhibits octahedral tilting patterns that are similar to the average structure of the orthorhombic phase. To illustrate this, we employed a moving average method

for analyzing the low-frequency behavior, which plays a critical role in the band gap of cubic phase $CsPbBr_3$. This is demonstrated in Figure 3.23, where we present the Fourier transformation of the time-dependent band gap. Notably, the primary contributors to the dynamic changes in the band gap are low-frequency components below 2.5 THz, indicating that the predominant time scale of these fluctuations lies within the range of hundreds of femtoseconds (fs) to 1 picosecond (ps). It is also important to note that the frequency range of the band gap is approximately twice that of the phonon frequency (around 5 Hz), which comes from the fact that electron-phonon coupling is proportional to the absolute value of displacement.

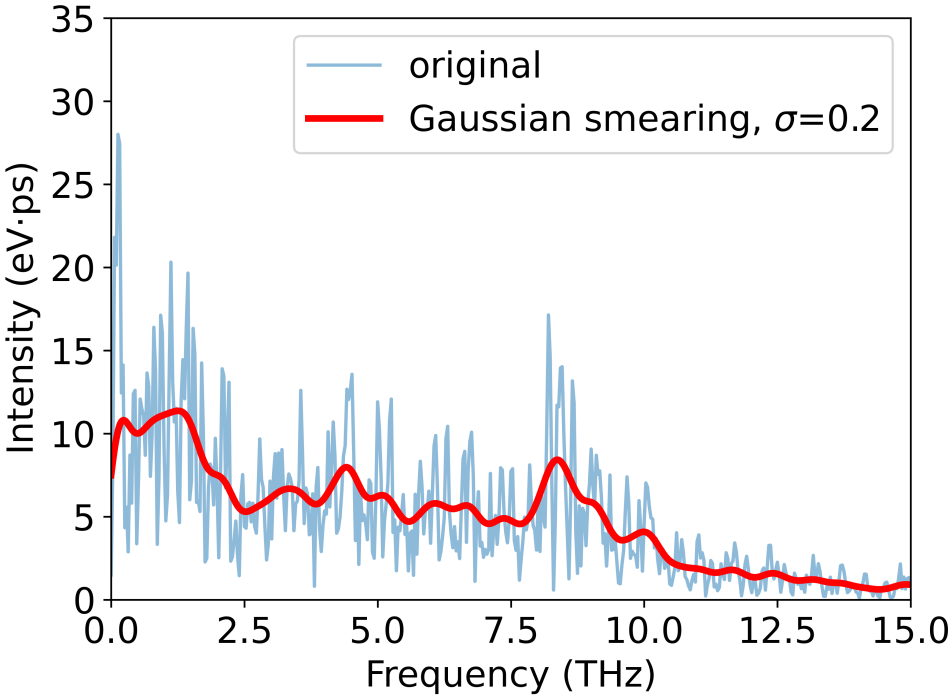

Figure 3.23 Spectrum of dynamic band-gap changes in $CsPbBr_3$, determined by performing a Fourier transformation on the time series of the band gap in MD simulation at 425 K, i.e. $\mathcal{F}E_g(t)$. The blue line is the original spectrum and the red line shows the smoothed spectrum after Gaussian smearing with a parameter $\sigma = 0.2$: $f_{\text{smoothed}}(x) = \int f(x') \frac{1}{\sqrt{2\pi}\sigma} e^{-\frac{(x-x')^2}{2\sigma^2}} dx'$. Reprinted with permission from [22]. *Copyright © 2023 by the American Physical Society.*

We refined our analysis by applying a moving average to the MD trajectory at 425K, with a time window of 1 ps, averaging all snapshots within this window to filter out the high-frequency components. The results are schematically shown in Figure 3.24, where we demonstrate this process with four representative samples of two octahedra from the supercell, spaced at 10 ps intervals. In Figure 3.24a, the orthorhombic phase at 325 K is shown, where the four averaged structures are very similar to the static structure. It indicates that octahedral tilting can be viewed as a static disorder from the cubic structure with atoms oscillating harmonically at the potential energy surface minima. Conversely, as depicted in Figure 3.24b, the cubic phase at 425 K presents four distinct averaged

structures, indicating dynamic disorder with atoms transitioning between different minima (octahedral tilting configurations) on a picosecond timescale.

This picture offers an explanation for the similar band gaps observed in the cubic and orthorhombic phases. The so-called ideal cubic structure is in reality a temporal average. At finite temperatures, atomic motions become significant, resulting in local and transient low-symmetry distortions in both space and time. Therefore, the cubic phase can be conceptualized as a 'dynamic' orthorhombic phase, which rationalizes the similarity in band gaps.

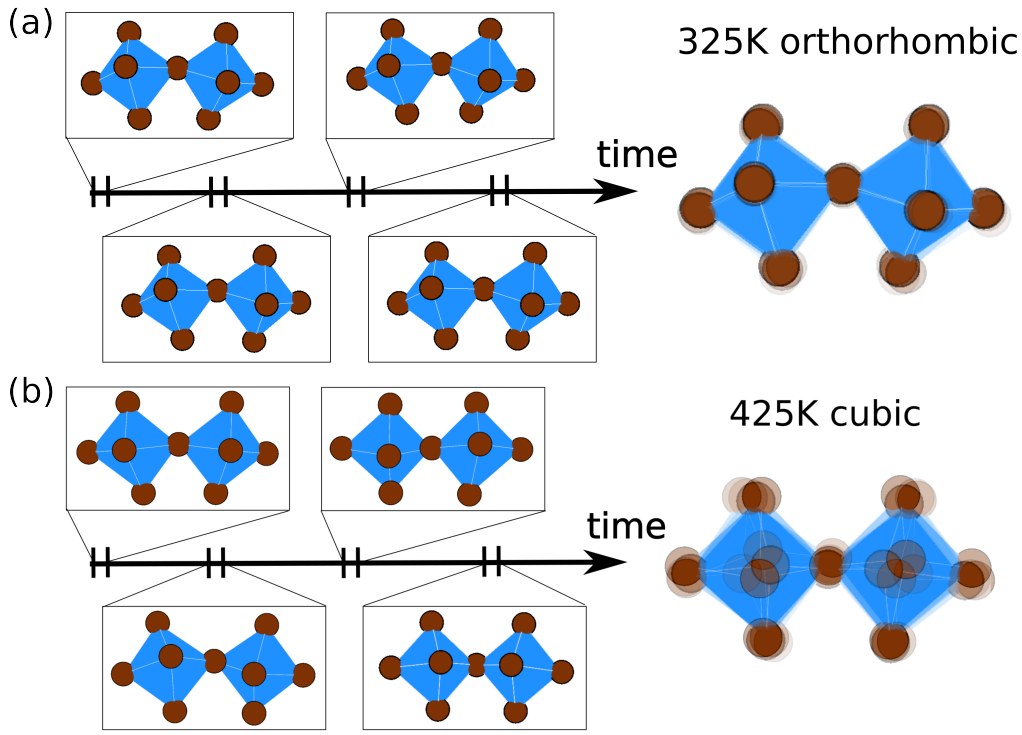

Figure 3.24 Left panel: Schematic diagram of structures time-averaged over a 1 ps window from specific segments of the MD trajectory in the cubic phase of $CsPbBr_3$ at temperatures of: (a) 425 K and (b) 325 K. Right panel: Schematic diagram that shows the overlap of the structures displayed in the left panel. Reprinted with permission from [22]. *Copyright © 2023 by the American Physical Society.*

To quantitatively examine the presence of low-symmetry local structures, we analyzed the radial distribution function g(r) and the Pb-Br-Pb bond angles in the XZ-plane for both the original MD structures in two phases [(a) and (c)] and the moving averaged structures of the cubic phase MD [(b) and (d)], as shown in Figure 3.25.

Specifically, Figure 3.25a reveals the difference in the radial distribution function (RDF) of the two phases. A noticeable distinction occurs around 4 Å, the expected range for Br-Br and Cs-Br pairs. At 325 K in the orthorhombic phase, two distinct peaks are evident at the position corresponding to the static structure. Conversely, for the ideal cubic structure at 425 K, Br-Br and Cs-Br pairs should exhibit identical distances; however, the MD dynamics suggest the emergence of two peaks. This finding aligns with the PDFs for Cs-Br seen in Figure 3.7 and for Br-Br in Figure 3.14a, which were discussed in the

previous chapter and also show two-peak characteristics. In Figure 3.7, the Cs-Br peak is found to be shorter than the distance in the ideal lattice, while in Figure 3.14a, the nearest neighbor Br-Br peak appears further than the ideal distance, indicating the presence of two peaks at 425 K.

This phenomenon was previously attributed to local disorders in Section 3.1.3, but now we show that this local disorder resembles the orthorhombic phase with the moving average structures of 425 K MD at Figure 3.25b. With the moving average applied to the 425 K MD structures, Figure 3.25b exhibits a resemblance to the orthorhombic phase, with two well-defined peaks in the RDF.

The distribution of bond angles in Figure 3.25c and 3.25d further supports these observations. Again, we see different behaviors of 325 K and 425 K distribution at first glance. In the orthorhombic phase, the static structure displays octahedral tilting with bond angles around 150° and 210°. The MD histogram reflects these tiltings with two corresponding peaks centered around these values, which are indicative of harmonic atomic oscillations. In the cubic phase, the ideal structure should exhibit a bond angle of 180° due to the absence of octahedral tilting. However, the 425 K histogram presents a broad peak stretching from 160° to 200° with almost the same amount of occurrence, suggesting the existence of local structures akin to the orthorhombic phase.

Aligned with the RDF obtained from the moving averaged structures of MD at 425 K shown in Figure 3.25(b), we present the histogram of band angle from the same set of moving averaged structures in Figure 3.25(d). By filtering out the high-frequency components, we observed a two-peak pattern resembling the orthorhombic phase. This serves as evidence for the emergence of orthorhombic-like low-symmetry disorder within the cubic phase.

3.2.6 Conclusion

In this chapter, we have explored the influence of thermal lattice vibrations on the band gap of $CsPbBr_3$. By employing a combination of DFT-based MC and MD calculations, we quantified the significant impact of dynamic fluctuations, extending beyond harmonic motions, on the electronic structure. Particularly in the cubic phase at 425 K, these fluctuations were found to contribute substantially, widening the band gap by approximately 450 meV. We developed a simplified model to further elucidate this observation, providing qualitative insights into the anharmonic effects at play. To understand the microscopic underpinnings of this observation, we investigate the relationship between the band gap and local structural dynamics. Using a moving average analysis of the MD trajectories, we demonstrated that low-symmetry structures, reminiscent of the orthorhombic phase, transiently emerge within the cubic phase, contributing to the dynamic variability of the band gap. Our approach highlights that the cubic phase maintains a dynamic balance of these transient low-symmetry structures, significantly influencing its electronic properties. This phenomenon offers a compelling explanation for the observed minimal changes in the band gap across various temperatures and during phase transitions, as identified in our experimental data. Consequently, our findings underscore that pronounced anhar-

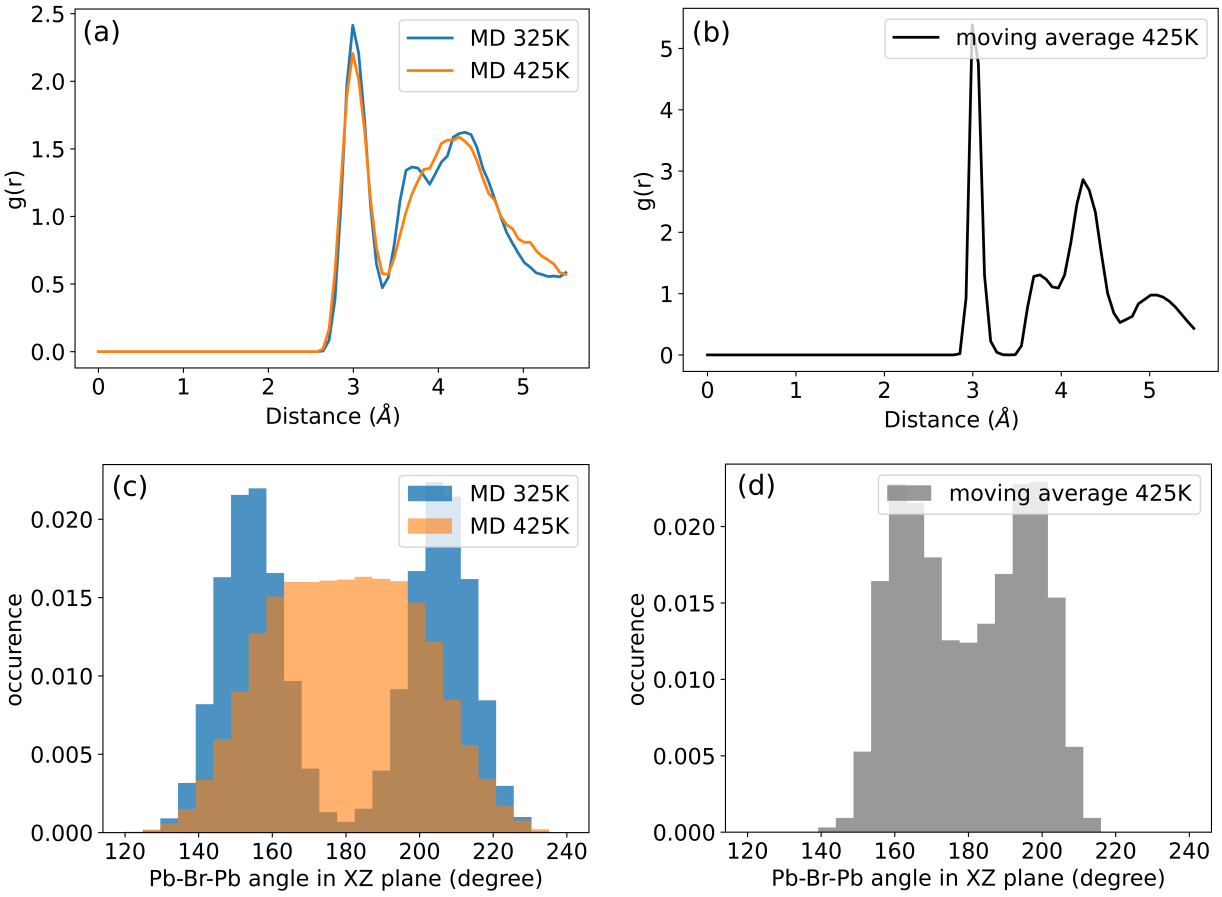

Figure 3.25 (a) Radial distribution function g(r) of $CsPbBr_3$ computed from the orthorhombic and cubic phase MD simulation. The blue line corresponds to the 325 K orthorhombic phase MD simulation, while the orange line is at the 425 K cubic phase. (b) Radial distribution function g(r) computed from a moving average structure of 425 K MD, as shown in Figure 3.24. We find signatures of peak splitting at around 4 Å that are reminiscent of the result for the orthorhombic phase as in panel (a). (c) Histogram of Pb-Br-Pb bond angles in $CsPbBr_3$ in the orthorhombic (325 K) and cubic (425 K) phase, computed from MD. (d) Histogram of Pb-Br-Pb bond angles computed from a moving average structure of 425 K MD. Applying a 1 ps moving average analysis to the bond angles again highlights features consistent with those of the orthorhombic phase, as the histogram demonstrated in blue color in panel (c). Reprinted with permission from [22]. *Copyright © 2023 by the American Physical Society.*

monic fluctuations and the transient emergence of low-symmetry structures, as revealed by our simplified model, are key in determining the electronic structure of $CsPbBr_3$.

Given the prevalence of large-amplitude anharmonic motions of halide ions in HaPs, these effects likely influence other variants as well. $MAPbBr_3$, a typical 3D hybrid organic-inorganic HaP, exhibits phase transitions at ≈150 K and ≈240 K [151]. Experimental studies have observed a 10 meV reduction in the optical transition energy at the lower-temperature transition and an almost continuous higher-temperature transition [146, 152, 153, 154], contrasting the larger band gap decrease predicted by static DFT [155]. Our findings that anharmonic fluctuations lead to only mild band gap changes might explain

this discrepancy: less pronounced fluctuations at lower temperatures lead to more noticeable band gap shifts at the orthorhombic-to-tetragonal transition due to the change of average structure and symmetry of crystal i.e., similar to the templating effect discussed in the literature [156, 157]. However, at higher temperatures, during the tetragonal-to-cubic transition, the anharmonic effect dominates, resulting in a continuous band gap [158, 159]. In 2D HaPs, more profound spectral changes have been observed during phase transitions at 270 K for BA_2PbI_4 [160, 161, 162]. Both DFT and optical measurements agree on band gap lowering due to structural and symmetry changes [161], but theoretical predictions of the shift are larger than experimental findings, which indictates that anharmonic fluctuations can also occur in 2D HaPs [163]. This analysis reveals that anharmonic fluctuations are a key factor in the behavior of electronic structure in HaPs, influencing the behavior of band gap change across different phases and temperature ranges. It highlights the potential of further optimizing the optoelectronic properties in HaPs through the engineering of chemical compositions.

3.3 Role of Overdamped Dynamics in Halide Perovskites

3.3.1 Overdamped dynamics in halide perovskites

The so-called overdamped phenomenon is defined for the behavior of soft mode approaching the phase transition temperature, which is often measured by vibrational spectroscopy. These measurements can not only provide the temperature dependence of the soft mode frequency but are also able to provide information on the behavior of the linewidth of the soft mode [25]. It was often found that the soft mode becomes heavily damped or even overdamped on approaching the transition temperature, where the linewidth is even larger than the soft mode frequency. The overdamped effect is observed in several oxide perovskites ($BaTiO_3$[164, 165, 166], $KNbO_3$[167, 168]), or bcc phase of Zr [169] and Ti [170]. The overdamped behavior has been reported in HaPs by neutron scattering experiments dating back to the 1970s [171]. In recent years, further studies on the overdamped behavior for both inorganic and hybrid HaPs were conducted by neutron and X-ray scattering measurements [172, 173, 174, 175, 176, 23].

Previous studies have shown that $CsPbBr_3$ is not only an anharmonic material but also displays overdamped fluctuations. Lanigan-Atkins et al. [23] showed that the overdamped mode span along the edges of the cubic Brillouin zone measured by momentum-resolved neutron and X-ray scattering. Fransson et al. [64] predicted that the overdamped mode remains over a wide temperature range (almost 200K) above the tetragonal-to-cubic transition temperature.

In the context of this thesis, anharmonicity means that the higher-order terms of potential energy beyond harmonic approximation are important. Among these anharmonic systems, we are especially interested in a group of materials with the double-well potential along specific normal mode coordinates. In other words, the second-order term of Taylor expansion of potential energy has negative coefficients. Notice that it does not necessarily mean this term is large. Thus, the phonon frequency of this normal mode calculated within harmonic approximation is imaginary. This is the case for many perovskites in the high-temperature phase, whose static structures are not at the minimum of ground state energy surface, and the structures are stabilized by thermal effect as discussed in Section 2.4.3.

If the anharmonicity is relatively small, one can stay in the quasi-particle picture based on perturbation theory, where phonons are dampened with a shifted frequency and finite lifetime. However, in some cases, the damping is comparable to phonon frequency. Thus, the phonon lifetime is shorter than one oscillation period, and the phonon picture may break down. This overdamped behavior causes challenges in both theoretical models and computational algorithms. In this work, we aim to evaluate the methodology and investigate the impact of overdamped behavior on band gaps of HaPs.

3.3.2 Separate MD dynamics on two time scales

In the previous chapter, we explored how anharmonic structural fluctuations significantly influence the electronic structure of cubic phase HaPs, resulting in band gaps that are comparable to those in the orthorhombic phase. We established that this band gap behavior is closely linked to the presence of transient low-symmetry structures, which become apparent upon filtering out high-frequency dynamics. In other words, the dynamics appear two-time scales, which might be a phenomenon also discussed in recent studies [177, 64], play a crucial role in substantial band gap renormalization.

To deepen our understanding of how dynamics across various time scales affect the band gap, we propose an extension of the moving average concept to encompass all time steps in MD simulations. Specifically, we calculate the moving average atomic displacements $u_{\mathrm{slow}}(t)$ to isolate the low-frequency component of atomic fluctuations, which is termed as "slow fluctuation" here because they have a characteristic time scale of ps. Note that the moving average is only applied to Cs atoms and Br displacements perpendicular to their bonding direction (as illustrated in the inset of Figure 3.26b) since these are the elements for which we found strongly anharmonic features. We define $u_{\mathrm{slow}}(t)$ using the following equation:

$$u_{\mathrm{slow}}(t) = \frac{1}{\Delta t}\int_{t}^{t+\Delta t} dt' u(t')w(t'), \tag{3.4}$$

where Δt represents the chosen averaging window, set at 4 ps, $u(t)$ represents the fluctuation of MD simulation, and $w(t)$ is a Blackman window function to reduce the spectral leakage after Fourier transformation. By subtracting the slow fluctuation part $\bar{u}_{\mathrm{slow}}(t)$ from the full fluctuation $u(t)$ in MD simulation, we derive the high-frequency component, named as "fast fluctuation":

$$u_{\mathrm{fast}}(t) = u(t) - u_{\mathrm{slow}}(t). \tag{3.5}$$

To visually demonstrate these fluctuations, Figure 3.26 displays the displacement of a single Br atom along one axis perpendicular to the bond in the MD simulation, illustrating the three types of fluctuations described above. The separation of the full MD fluctuation can be comprehended through the perspective of muti-well PES. In this framework, slow fluctuations (Figure 3.26b) are associated with the motion of atoms among the multiple minima of the PES, each representing different octahedral tilting configurations. These slow fluctuations, characterized by their longer time scales, reflect the system's ability to explore various structural configurations across different potential wells in the cubic phase. On the other hand, fast fluctuations (Figure 3.26c) correspond to the more rapid oscillations of atoms around these minima within a single well. In our definition, after the removal of the inter-well motion attributed to the slow fluctuations, these minima are adjusted to the ideal cubic structure. As a result, fast fluctuations are understood to represent atomic oscillations within a 'pseudo' potential well, which is centered around the ideal structure.

Additionally, we have calculated the corresponding band gap (using PBE functional without SOC) for each type of fluctuation by averaging the band gaps of sampled structures across all three fluctuation categories. In Table 3.1, we list the band gaps obtained with different methods for cubic phase at 425 K. Remarkably, the slow fluctuations alone yield

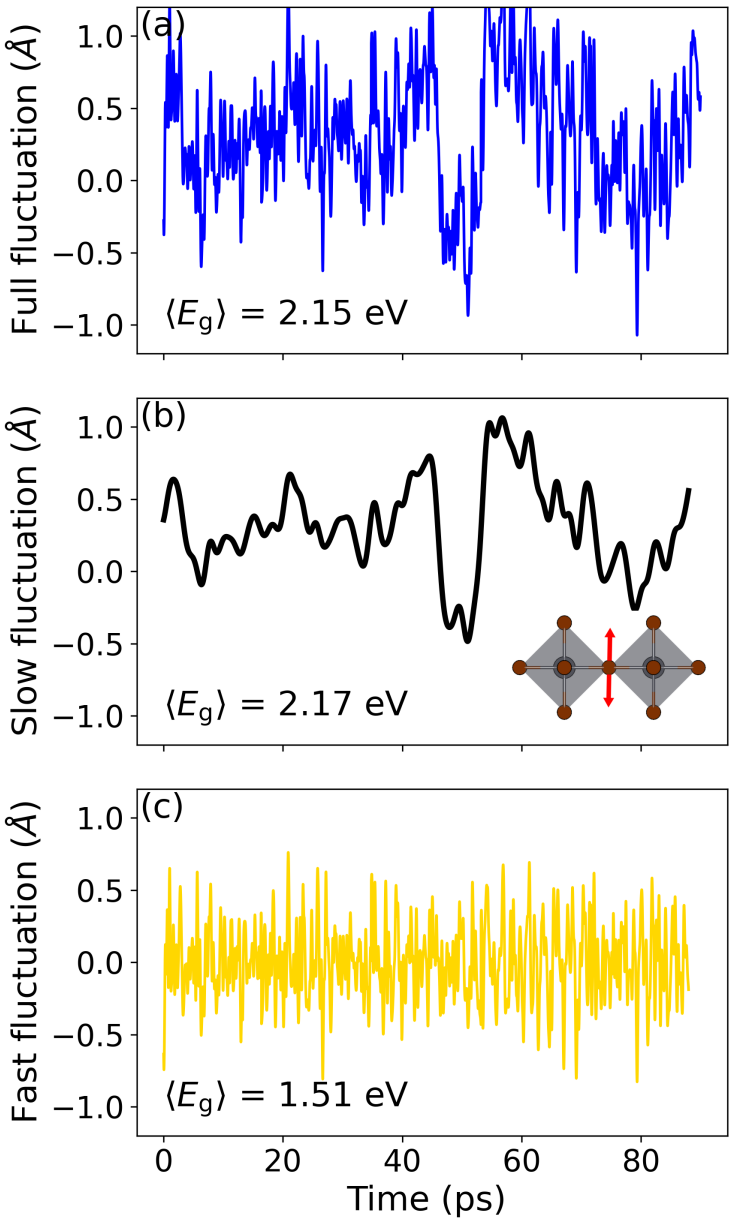

Figure 3.26 (a) Total fluctuation of a typical Br displacement. (b) Slow fluctuation from moving-averaged of full displacement. The time window is 4 ps. (c) Fast fluctuation moves around the moving-averaged displacement which is obtained by subtracting the moving average from the full fluctuation.

	static	MC	MD	MD fast	MD slow
Band gap (eV)	1.43	1.78	2.15	1.51	2.17

Table 3.1 Band gap at 425K with different methods

a band gap (2.17 eV) that is similar to that obtained from the full MD simulation (2.15 eV). In contrast, the band gap resulting from fast fluctuations (1.51 eV) is significantly smaller than that of the slow fluctuations. Thus, we can conclude that the large renormalization of the band gap by anharmonic fluctuations is primarily driven by the slow fluctuation component, which corresponds to the low-symmetry structures at potential minima. Moreover, we can also find the band gap of fast fluctuation is comparable to the gap from MC approach, which is based on the harmonic approximation. In other words, if we ignore the possibility of hoping through the energy barrier and only consider the dynamics within the local minima of the potential well, the high-frequency components in MD simulation can be approximated to atomic motion in an effective harmonic potential.

3.3.3 Damped harmonic oscillator (DHO) model

As discussed in Section 2.4.3, a DHO model can be used to understand the overdamped modes [64]. Instead of using independent harmonic oscillators to describe the phonon modes as done in harmonic approximation, we use damped harmonic oscillators to include the interaction between modes via a damping coefficient:

$$\frac{d^2Q_k(t)}{dt^2} + \Gamma_k \frac{dQ_k(t)}{dt} + \omega_k^2 Q_k(t) = 0 \tag{3.6}$$

where Γ_k is the damping coefficient and ω_k is the frequency of undamped harmonic oscillator of mode $k = (\mathbf{k}, \nu)$.

In the overdamped case, where $\omega_k < \Gamma_k/2$, the velocity autocorrelation function can be derived as shown in Eq. (3.7) [64]:

$$C(t) = \frac{A'}{\tau_L - \tau_S}\left(\frac{1}{\tau_S}e^{-t/\tau_S} - \frac{1}{\tau_L}e^{-t/\tau_L}\right), \tag{3.7}$$

where τ_S and τ_L correspond to fast (short time-scale) and slow (long time-scale) fluctuations, respectively, as defined in Eq. (2.103). This equation demonstrates that overdamped phonon modes lead to dynamics with two distinct time scales.

To further validate this in the context of $CsPbBr_3$, we calculated the VDOS for both the full MD simulation and the fast MD fluctuation, as illustrated in Figure 3.26. The results, presented in Figure 3.27, show that the VDOS of the full fluctuation and fast fluctuation are strikingly similar, except for the low-frequency range. This observation is consistent with expectations for a strongly overdamped scenario, characterized by $\tau_L \gg \tau_S$. In such cases, the second term (with time scale τ_L) in the expression of the velocity autocorrelation function (Eq. (3.7)) is much smaller compared to the first term (with time

scale τ_S). Since the VDOS is related to the Fourier transformation of the velocity autocorrelation function, the long time term only contributes little to the low-frequency range in VDOS. This shows that our MD simulation aligns with the theoretical understanding of overdamped dynamics with the DHO model.

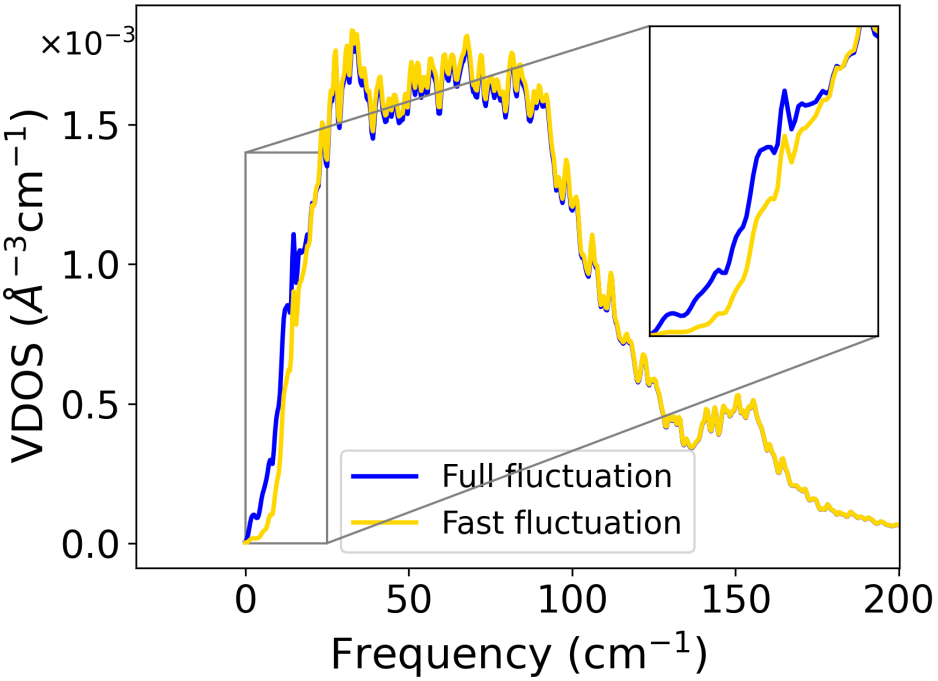

Figure 3.27 VDOS of full fluctuation (blue) and fast fluctuation (gold) at 425K. The inset is a zoom-in at the low-frequency range.

3.3.4 Augmented MC with renormalized phonons

In Chapter 3.2.3, we evaluated the contributions of anharmonic effects on temperature-dependent band gaps by comparing MC and MD methods. However, we encountered a limitation of the MC method, particularly in handling imaginary phonon modes. This limitation arises because the displacements generated in our approach are proportional to $1/\omega$, as discussed in Eq. (2.145). Thus, it is not applicable to phonon modes with imaginary frequency.

A frequently adopted approach for addressing anharmonic phonon modes is phonon renormalization, as discussed in Section 2.4.4. This approach utilizes renormalized phonon modes to calculate various properties, including thermal characteristics [54], electronic structure renormalization [90], and carrier transport [178]. However, applying this method for band gap calculations in HaPs is questionable, especially due to the presence of overdamped phonon modes, which can lead to the breakdown of phonon pictures.

To elucidate the impact of overdamped dynamics, we examine two examples: $SrTiO_3$ at 1000 K and $CsPbBr_3$ at 425 K. They are chosen since both of these materials share per-

ovskite structures and exhibit strong anharmonicity. We focus on the temperature range of cubic phases, where they both display soft phonon modes with imaginary frequencies in the harmonic approximation. In $SrTiO_3$, these soft modes are found at the Brillouin zone center and boundary, corresponding to ferroelectric modes of polarized displacements and antiferrodistortive modes of octahedral rotations, respectively. In $CsPbBr_3$, the soft modes are associated with in-phase and out-of-phase octahedral rotations, which are exclusively located at the Brillouin zone boundary.

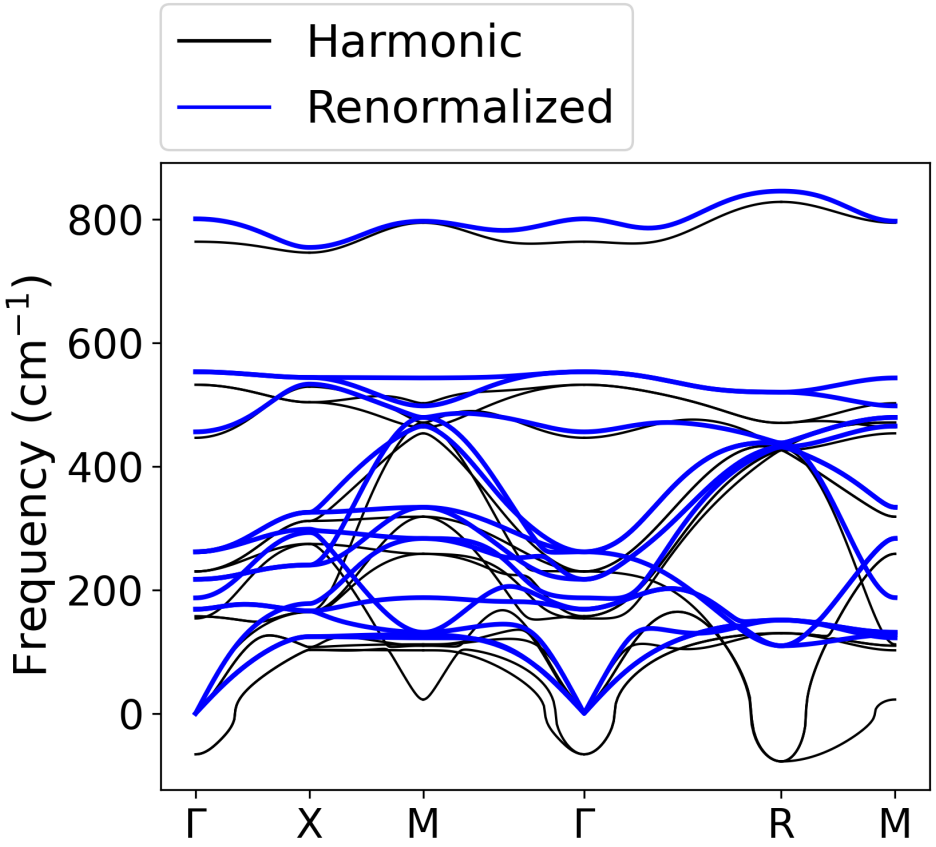

Figure 3.28 Phonon dispersion of cubic $SrTiO_3$ calculated with the PBEsol functional. The black line corresponds to the phonon modes with harmonic approximation and the blue line corresponds to the phonon modes after phonon renormalization at 1000 K.

Figure 3.28 presents the phonon dispersion of $SrTiO_3$. The harmonic approximation is depicted with a black line, while the phonon dispersion after renormalization at 1000 K is shown in a blue line. Here we use the Temperature-Dependent Effective Potential (TDEP) method [74, 55] for renormalizing the phonon modes. After the renormalization, the imaginary-frequency modes are stabilized and we see an increase of frequency of phonon modes in general.

Building on our analysis of phonon dispersion in $SrTiO_3$, we now turn our attention to band gap calculations. Using the two sets of phonon modes, we evaluated the band gap at 1000 K using the MC method and compared it with the band gaps derived from MD, as indicated in Table 3.2. In the table, the MC calculation based on harmonic phonon

Material	Static	MC (Harmonic)	MC (Renormalized)	MD
$SrTiO_3$ @ 1000 K	1.81 eV	1.97 eV	1.46 eV	1.53 eV
$CsPbBr_3$ @ 425 K	1.43 eV	1.78 eV	1.64 eV	2.15 eV

Table 3.2 Comparison of band gaps of $SrTiO_3$ at 1000 K and $CsPbBr_3$ at 425 K calculated using different methods

modes is labeled as 'MC (Harmonic)'. For this, we disregard the imaginary frequency modes at the Γ and R points, as well as the very low-frequency mode at the M point in the Brillouin zone. The MC calculation using renormalized phonon modes is denoted as 'MC (Renormalized)', where all phonon modes are considered with no imaginary frequency after renormalization.

Compared against the static band gap of $SrTiO_3$, the band gap derived from the MC method using harmonic phonon modes shows an increase with temperature, which is a feature discussed by Wu et al. [90]. Noteworthy, the MC method with renormalized phonons results in a decrease of the band gap, as measured in previous experiments [179]. Moreover, the band gap values obtained from the MC method with renormalized phonons align well with the MD results, which consider anharmonicity to full order. It suggests that the MC with renormalized phonon approach (see Section 2.5.3) effectively captures the gap renormalization associated with anharmonic effects in cubic phase $SrTiO_3$. On the other hand, the regular MC fails to capture the correct trend with respect to temperatures.

Similar to $SrTiO_3$, the cubic phase of $CsPbBr_3$ also exhibits instability at 0 K, as shown in the phonon dispersion in Figure 3.29. The harmonic phonon modes, represented by black lines, display imaginary frequencies at the M and R points within the Brillouin zone, while the renormalized phonon modes are displayed in blue lines using DynaPhoPy [69] with the help of MD simulation. Also, the renormalized phonon modes are calculated with full MD simulation, exclusively considering the fast fluctuations to investigate the anharmonic effects. Furthermore, phonon renormalization that only considers fast fluctuations (see Section 3.3.2) is also calculated as a comparison, which is illustrated in Figure 3.29 with golden lines. In this case, we use a pseudo-trajectory that only considers the high-frequency fluctuations around the ideal lattice as an input to DynaPhoPy for phonon renormalization.

Surprisingly, considering only fast fluctuations leads to similar phonon dispersion as with the full dynamics. This observation suggests that the fast fluctuations dominate the phonon renormalization process, while the slow fluctuations contributions, which are important for accurately capturing the band gap changes, play a minor role. In fact, this feature aligns with the results of VDOS in Figure. 3.27, where it was found that the impact of slow fluctuations is considerably less pronounced than that of fast fluctuations, reinforcing the notion that the latter plays a dominant role in the phonon dispersion characteristics.

However, the discussion also highlights a limitation in our phonon renormalization methodology, particularly for overdamped systems like $CsPbBr_3$ at 425 K. It fails to account for

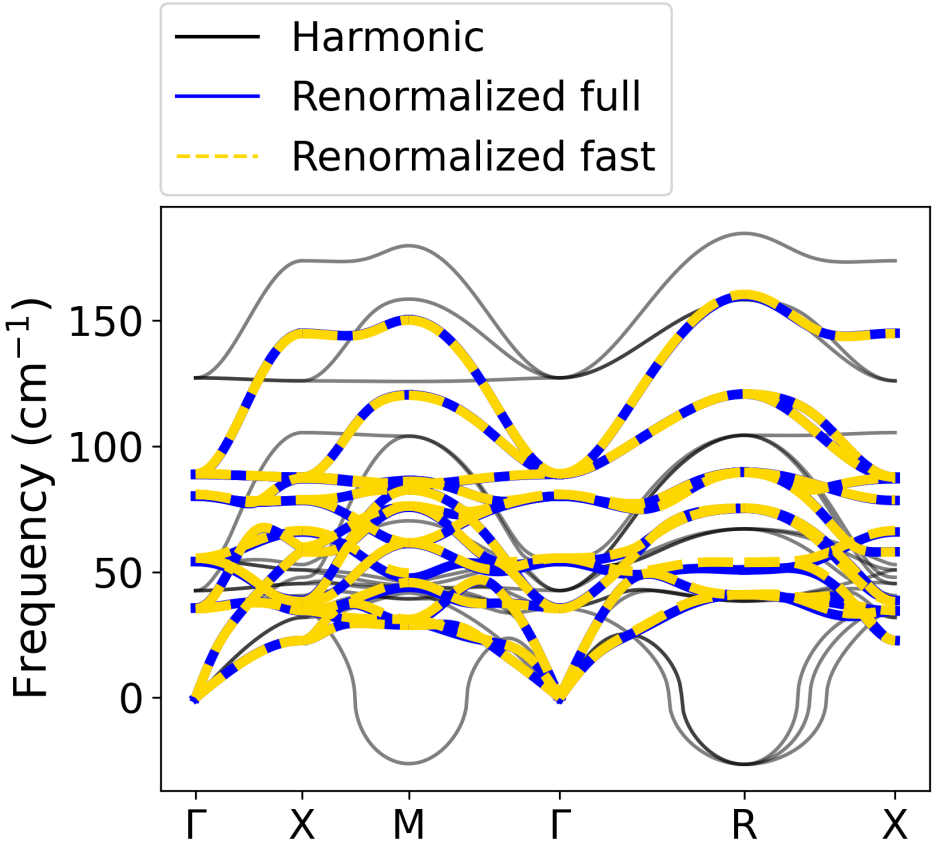

Figure 3.29 Phonon dispersion of cubic $CsPbBr_3$ calculated with the PBE+TS functional. The solid black line corresponds to the phonon modes with harmonic approximation, the solid blue line corresponds to the phonon modes after phonon renormalization with full MD at 425 K, and the dashed golden line represents the phonon renormalized by the fast fluctuation extracted from MD as discussed in Figure 3.26c.

the impact of slow fluctuations on band gap renormalization. The renormalization process of DynaPhoPy is based on so-called “normal mode decomposition", where one projects VDOS on the phonon modes and fits the projection to a Lorentzian function to obtain the renormalized phonon frequency (see Section 2.4.4). This method, while effective in capturing the essence of phonon behavior influenced by fast fluctuations, may not fully account for the broader spectrum of dynamic interactions facilitated by slow fluctuations. Therefore, the resulting phonon dispersion cannot fully reflect the material’s anharmonic landscape and its impact on the electronic structure.

The band gap results of $CsPbBr_3$ at 425 K are shown in the second row of Table 3.2. In contrast to $SrTiO_3$, for $CsPbBr_3$ the MC with renormalized phonon method leads to the band gap renormalization very close to MC with harmonic phonon. However, it fails to obtain a similar band gap as MD, which serves as a benchmark for fully capturing the material’s anharmonicity.

The observed discrepancies between $SrTiO_3$ at 1000 K and $CsPbBr_3$ at 425 K highlight the presence of distinct anharmonic dynamics across different materials [180], which influences their electronic properties significantly. A critical difference is whether overdamped phonon modes are present, which introduces two time scales into the dynamics, and leads to breakdown of independent phonon framework. It has been shown in experiments that the soft modes in $SrTiO_3$ only exhibit overdamped behavior nearing the transition temperature [181, 182, 183], and are underdamped at 1000 K. Conversely, $CsPbBr_3$ demonstrates overdamped behavior over a broader temperature range after phase transition, extending nearly to 600 K [64], highlighting a more substantial influence of anharmonic dynamics beyond mere transitional phenomena. In this case, the common used phonon renormalization cannot capture both time scales and lead to a challenge in characterizing and accounting for anharmonicity in theoretical and computational models.

3.3.5 Augmented MC with anharmonic effect

In order to correctly characterize the complex dynamics for overdamped phonon mode, we augment the MC approach beyond the limitation of harmonic and Gaussian distributions (see detailed discussion of theory in Section 2.5.3). This new method has the advantage of better characterizing the dynamics based on a more complex potential well. In the previously introduced MC method, our calculations are always based on the assumption of a harmonic potential, either by directly calculating the phonon eigenvector and frequency from the dynamical matrix (standard MC) or by fitting to a second-order potential or Lorentzian distribution with phonon renormalization (MC with renormalized phonon). Conversely, the new method involves sampling the soft modes through a non-Gaussian distribution derived from a potential energy that includes higher-order terms, which allows us to better model the atomic fluctuations in the system.

The method begins with the identification of the soft modes, which become unstable and lead to overdamped dynamics at certain temperatures range. In $CsPbBr_3$, there are three phonon modes at M point and three at R point in the Brillouin zone that relate to octahedral tiltings around three axes. The eigenvectors of these phonon modes can be calculated with Phonopy [150]. One can displace the atoms along the eigenvector and calculate the total energy of distorted structures with VASP [116] to obtain the potential energy in normal mode coordinates. Since the phonon modes are unstable, the energy at the ideal position is not minimal and cannot be fit to a quadratic function. That is why we use a polynomial up to the 14th order to fit the potential energies as shown previously in Figure 3.30a.

Once the potential well $U(Q)$ for a specific phonon mode is obtained, we can solve a 1D Shördinger equation (Eq. (3.8)) with this potential in the normal mode coordinates Q

$$-\frac{\hbar^2}{2m_p}\frac{d^2\psi_i(Q)}{dQ^2} + U(Q)\psi_i(Q) = E_i\psi_i(Q), \tag{3.8}$$

where m_p is the proton mass, and ψ_i is the wavefunction of the i-th quantum state with energy level E_i (horizontal lines in Fig. 3.30a). Then, one can obtain the distribution over

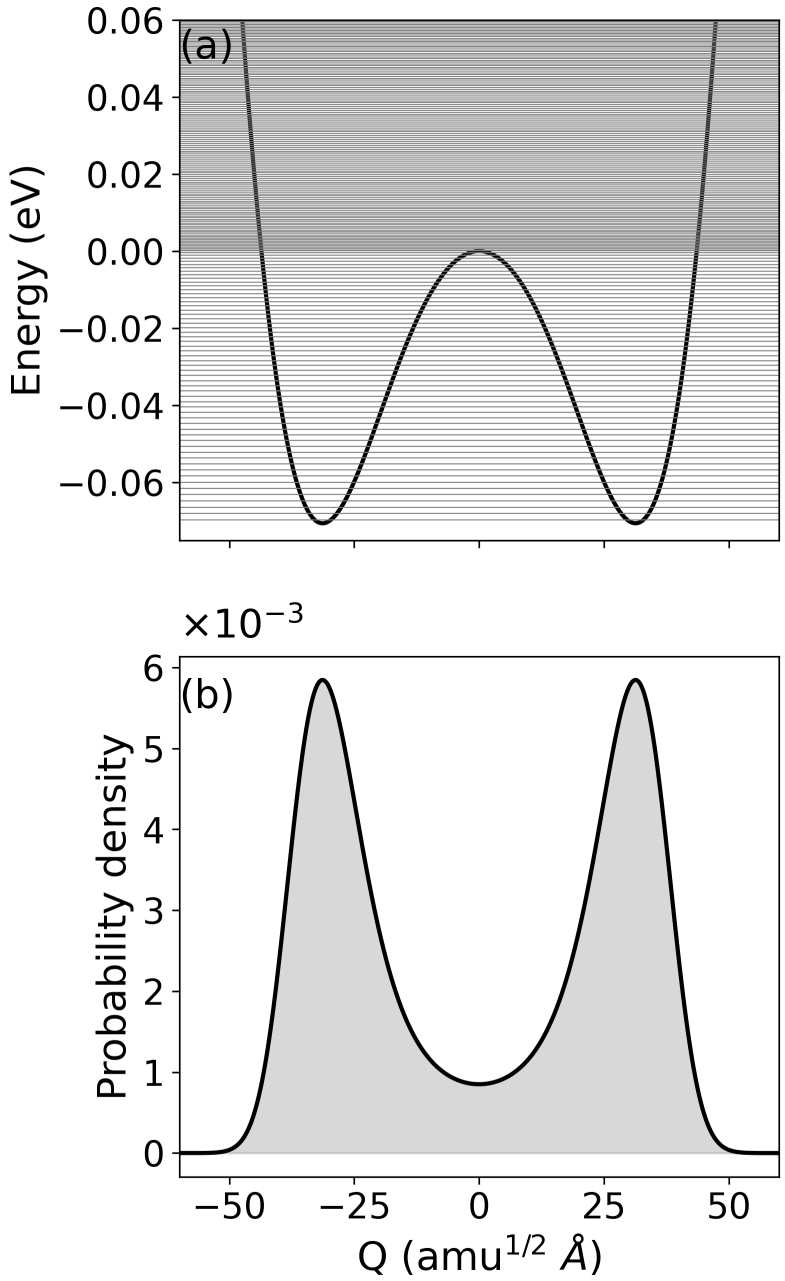

Figure 3.30 (a) Anharmonic double-well potential energy along the mode M as a function of normal mode coordinates Q. The horizontal lines represent the eigenvalues by solving the Schoṙdinger equation. (b) The corresponding probability density distribution as a function of Q.

the normal mode coordinates Q at finite temperature by assuming the occupation for each quantum state following Boltzmann distribution as discussed in Eq. (2.148).

$$P_i(Q) = \frac{1}{Z}\sum_{i=0}^{\infty} e^{-\frac{E_i}{k_B T}} |\psi_i(Q)|^2. \tag{3.9}$$

where the partition function $Z = \sum_{i=0}^{\infty} e^{-\frac{E_i}{k_B T}}$ and $|\psi_i(Q)|^2$ represents the probability of Q of i-th quantum state. Figure 3.30b shows the probability distribution of soft mode at M=(0.5,0.5,0).

After we established the appropriate distribution, the MC simulation proceeds by sampling configurations according to this tailored distribution. In practice, we directly add displacements generated from the above probability to the harmonic MC, which does not include these imaginary phonon modes. This procedure allows for a more accurate representation of the system's ensemble space, including especially those slow fluctuations (Figure 3.26b) related to the octahedral tilting modes.

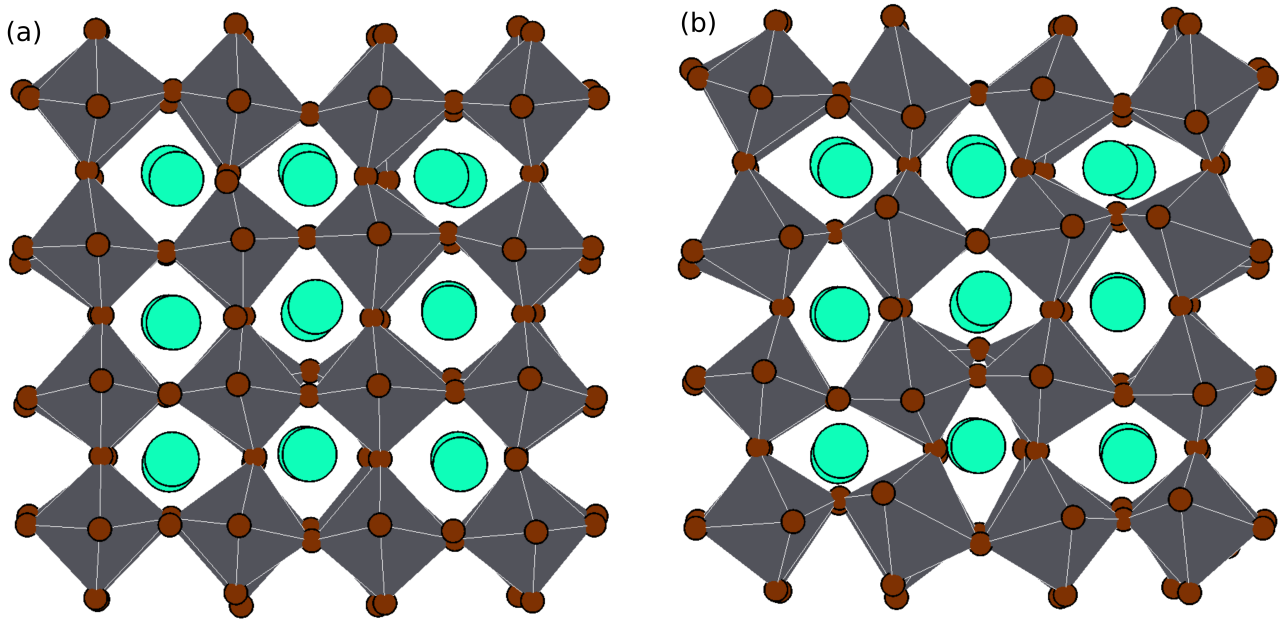

Figure 3.31 Exampled (a) structure generated from standard MC without imaginary phonon mode and (b) structure generated from augmented MC considering the soft phonon mode.

This can be seen by the comparison of sampled configurations obtained from two methods in Figure 3.31. Figure 3.31a shows the result from harmonic MC, where the imaginary modes are ignored. Though there are distortions of octahedra, the tilting behavior is not really captured. Conversely, after we add the effect of imaginary modes using our augmented MC method in Figure 3.31b, the octahedral tilting is more obvious. This is important to correctly reproduce the band gap of the system.

Notably, we are able to obtain the band gap of 1.92 eV at 425 K for $CsPbBr_3$ with the augmented MC method, which is much closer to the MD gap. Through the augmented MC, we not only provide a method to better compute the electronic properties of anharmonic materials with significant overdamped phonon modes but also improve our understanding of how lattice dynamics contribute to them.

3.3.6 Disentangle the phonon contribution to band gap

We have used three methods to calculate the band gaps of $CsPbBr_3$ at 425 K in the last sections. Given the overdamped dynamics of these material, the methods lead to different results. The MD fully includes the anharmonic dynamics and can reproduce the mild band-gap change across phase transition. However, it has several disadvantages. First, the validity of this approach is based on the assumption that the ensemble average can be approximated with time average, which requires a long enough simulation time, especially for materials with complex potential energy surfaces. For example, configurations with small probability but large effects on the electronic properties could be missed in the simulation. It is possible to simulate several MD trajectories from different starting points in parallel to obtain better statistics to alleviate the problem. Second, although the MD method provides a large amount of information, it is hard to interpret from a theoretical viewpoint. Concepts such as phonon or anharmonicity cannot be directly applied to the atomic positions and atomic velocities. Analysis related correlation functions are required, but again largely constrained by the size of simulation cells and the length of simulation time.

On the contrary, the MC methods are easier to implement with stochastic sampling of phase space. Also, the sampling of this method is based on phonons with normal mode coordinates, so it is easier to disentangle the contribution through a perturbative perspective and provide further physical understanding. In addition, the sampling can be fully quantum mechanical, which is important for studying materials at low temperatures. However, we have seen that the MC method is not fully valid for materials with complex dynamics including anharmonicity or overdamped phonons. Even after being augmented with anharmonicity, there is still a difference from the gap obtained by MD method for $CsPbBr_3$.

To further understand the origin of the difference, we expand the potential energy $V(\{Q_i\})$ in terms of normal mode coordinates Q_i:

$$\begin{aligned} V(\{Q_i\}) = &\sum_i a_i^{(2)} Q_i^2 && \text{(harmonic terms)} \\ &+ \sum_i a_i^{(3)} Q_i^3 + a_i^{(4)} Q_i^4 + \dots && \text{(higher-order anharmonic terms)} \\ &+ \sum_{ij} b_{ij}^{(4)} Q_i^2 Q_j^2 + \dots && \text{(cross anharmonic terms)} \end{aligned} \tag{3.10}$$

where $a_i^{(n)}$ and $b_{ij}^{(n)}$ are the n-th order coefficients of terms with one normal mode coordinate and terms with more than one coordinate.

As briefly discussed in Section 2.5.3, although we have augmented MC method with high-order anharmonic terms for each normal mode, the interactions between normal modes (cross anharmonic terms in Eq. (3.10)) are ignored. These cross terms are expected to be small since we start from harmonic approximation where there is no interaction between phonon modes. Thus, only the first two lines of Eq. (3.10) are considered in these methods. However, in our case, the overdamped behavior of $CsPbBr_3$ at 425 K makes the system significantly deviate from the harmonic approximation so that the

cross anharmonic terms cannot be ignored anymore. In conclusion, we can infer that the remaining 0.2 eV discrepancy between MD and the augmented MC method for the band gap comes from the effect of cross anharmonic terms on the electronic structures.

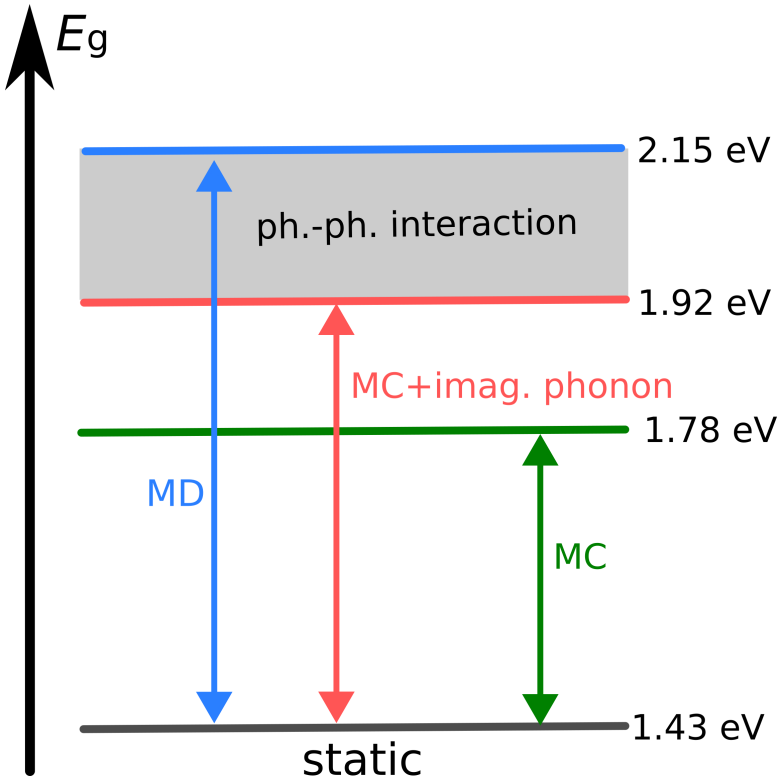

Figure 3.32 Sketch of band gaps of $CsPbBr_3$ at 425 K obtained from different methods with PBE functional. The blue line is MD result that includes all the anharmonic terms. The red line is the augmented MC with anharmonicity. The green line represents the harmonic MC that does not consider the imaginary phonons.

The analysis depicted in Figure 3.32 provides a schematic illustration of phonon contributions to the band gap renormalization for $CsPbBr_3$ at 425 K. By differentiating between the impacts of harmonic, higher-order anharmonic, and cross-anharmonic terms within the lattice dynamics in Eq. (3.10), we are able to conduct a detailed exploration of how each component influences the electronic structure at finite temperature conditions. This disentanglement is critical for a deeper understanding of the intricate interplay between phonon dynamics and electronic properties in materials exhibiting strong anharmonic behavior. It is important to note that both methodologies incorporate electron-phonon coupling via the formalism presented in Eq. (2.130), which inherently considers higher-order terms in electron-phonon interaction. Consequently, the observed discrepancies in band gap renormalization are attributed solely to the differing approaches to sampling lattice dynamics at finite temperatures.

In Figure 3.32, the MD results, depicted by the blue line, serve as a benchmark by encompassing the full spectrum of anharmonic dynamics, including both higher-order anharmonic terms and cross-anharmonic interactions. Compared to the static structure, this comprehensive dynamic approach yields an increased band gap of approximately 0.7 eV. The red line illustrates the outcomes from the augmented MC method, which incorporates

higher-order anharmonic contributions in addition to harmonic terms, resulting in a band gap renormalization of 0.5 eV. The area shaded in grey between these two lines quantifies the effect of phonon-phonon interactions not fully captured by the augmented MC method. This partial consideration highlights the significant role that these higher-order terms play in the overdamped material, offering insight into the mechanisms driving the band gap changes. Finally, the green line represents the traditional MC method, which considers only harmonic vibrations, leading to a band gap renormalization of 0.35 eV.

In summary, this comprehensive analysis not only sheds light on the individual contributions of different phonon interactions to the band gap renormalization but also underscores the necessity of incorporating a full spectrum of phonon dynamics for accurate materials modeling. It reveals that while the augmented MC method provides a significant step forward in capturing the essence of anharmonic effects, there remains a gap in fully replicating the complex phonon-phonon interactions observed in full MD simulations. This gap points to the ongoing challenge and opportunity for further methodological advancements to bridge our understanding of phonon contributions and their effects on material properties at finite temperatures.

3.3.7 Conclusion

In this chapter, we have focused on probing the impact of overdamped phonon modes on dynamic and electronic properties. Through an investigation with different methodologies, including MD, MC methods with renormalized phonon, and MC methods with anharmonic effect, we unravel the complex interplay between various phonon dynamics and their contributions to the band gap renormalization in cubic phase perovskites. We highlight the critical role of transient low-symmetry structures and the necessity to account for both fast and slow fluctuations within these materials.

Applying the moving average concepts to MD simulations, we have categorized the dynamics of $CsPbBr_3$ at 425 K as 'slow fluctuation' and 'fast fluctuation'. By examining the impact of two time scales on the band gap separately, we find that the large renormalization of the band gap in this material mainly comes from the slow fluctuation. Moreover, this behavior is further understood through DHO model, offering novel insights into the special anharmonic effects of $CsPbBr_3$ with overdamped phonon modes. Given the breakdown of the independent phonon model for overdamped materials, the computation method based on phonons may not work. For example, this issue limits the usage of the MC with the renormalized phonon method, which can well capture the anharmonic fluctuations for underdamped anharmonic materials like $SrTiO_3$. The introduction of the augmented MC method improves the prediction of the electronic properties, which is tailored to incorporate non-Gaussian distributions arising from complex potential energy landscapes. This novel method can capture the anharmonic fluctuations more accurately and advance our understanding of HaPs. Furthermore, we have calculated the influence of harmonic, higher-order anharmonic, and cross-anharmonic terms for $CsPbBr_3$ by disentangling phonon contributions to the band gap. This disentanglement identifies the

limitations of the augmented MC method in fully replicating the intricate phonon-phonon interactions captured by full MD simulations.

In conclusion, this chapter has not only contributed to our theoretical knowledge of electron-phonon coupling for overdamped phonon modes in HaPs but also established a classification of anharmonic behaviors for applying methods practically. These insights pave the way for future research on the unique anharmonic dynamics of HaPs, driving control and prediction of material behaviors of halide perovskite optoelectronic devices.

4 Conclusions and Outlook

Halide perovskites (HaPs) are promising candidates for next-generation photovoltaic materials with fast development of efficiency and low-cost production process. Distinct from traditional inorganic semiconductors, HaPs are characterized by their unique anharmonic vibrational fluctuations, intimately linked to their exceptional optoelectronic behaviors. Despite their promising attributes, a complete understanding of the anharmonic structural dynamics and their extensive implications on material functionality has remained to be investigated. Here, we probed the underlying physical mechanisms governing the microscopic dynamics and illustrated the influence of these mechanisms on the macroscopic functional properties through a combination of computational and theoretical perspectives. Specifically, this work studied the anharmonic dynamics of $CsPbBr_3$, a prototypical halide perovskite, unveiling the significant impact of anharmonicity on its electronic properties and highlighting the crucial role of overdamped dynamics. Various computational methods were used to explore the connection between dynamics and electronic properties at finite temperatures. Our analysis based on molecular dynamics not only challenges the conventional harmonic approximation but also provides insight into local disorder that leads to the mild band gap change across phases. We developed augmented Monte Carlo methods by integrating the often-overlooked imaginary soft phonons, thereby enriching our understanding of the complex anharmonic landscape of HaPs. These results set the stage for future innovations in photovoltaic material development.

To characterize the complex vibrational dynamics of halide perovskites at finite temperatures, our investigation started with examining the atomic structures within $CsPbBr_3$ from first-principles molecular dynamics calculations. We uncovered that the real-time atomic trajectories of Cs and Br atoms strongly deviate from the harmonic vibrations of an ideal cubic lattice. This deviation not only probed the strong anharmonic effect on dynamics but also illustrated the profound coupling between Cs and Br atoms. This coupling reduced Cs–Br distances and indicated the presence of very shallow potential wells of transversal Br motions within a dynamic potential energy landscape. Our analysis further revealed the critical role of Cs–Br interactions in facilitating octahedral tilting dynamics, which is closely associated with the soft modes of $CsPbBr_3$. By drawing connections to $PbBr_6$ octahedral tilting modes, we illustrated how these local interactions underpin the broader lattice dynamics, contributing to the material's unique anharmonic characteristics. The comparative study of dynamic behavior across temperatures unveiled the material's distinctive structural phase transition, offering new insights into the temperature-dependent behavior of $CsPbBr_3$.

The investigation of the anharmonic dynamics focusing on the coupling motion of Cs and Br atoms improved our understanding of the dynamic properties of halide perovskites.

The A-site of halide perovskites is often viewed as a space filler since it does not contribute to the electronic states near the band edges. However, our findings underscore the critical role of A-site cations in forming local disorders and indirectly influencing the optoelectronic properties of HaPs. This revelation opens up new perspectives on the potential applications for A-site engineering. Building on this understanding, the dynamic interplay observed between halide ions and A-site cations in $CsPbBr_3$ invites further exploration, especially in hybrid halide perovskites where organic molecules occupy the A-site. Moreover, understanding the local disorders opens new avenues for tailoring their optoelectronic behavior. By manipulating the local structures or phases through external means, such as pressure application or elemental mixing, we can potentially engineer materials with optimized properties for specific applications. Besides, the investigation found a correlation between the Cs movement and in-phase octahedral tilting, which could be a possible origin of the specific structural phase transition from cubic to $P4/mbm$ tetragonal phase.

Next, we explored the impact of thermal lattice vibrations on the band gap of $CsPbBr_3$ and showed that the static structures have large discrepancies from the experimental band gaps, emphasizing the necessity to consider the anharmonic effect. We quantified the anharmonic effects by comparing MC and MD results and demonstrated their large impact on band gaps of halide perovskites at high-temperature phases. Our analysis also revealed the transient emergence of low-symmetry structures within the cubic phase, which can be viewed as reminiscent of the orthorhombic phase. These transient low-symmetry structures showed the dynamic disorder nature of the cubic phase, profoundly influencing its electronic properties. Such findings provide a robust framework for interpreting the mild changes observed in the band gap across various temperatures and during phase transitions, consistent with experimental data.

From an experimental standpoint, our research can extend into the realm of HaPs semiconductors beyond $CsPbBr_3$, shedding light on the general behavior of electronic properties of HaPs under thermal fluctuations. The behavior of band gaps across the phase transition provides invaluable information about the dynamic properties of these systems. This understanding is not confined to 3D inorganic HaPs alone but extends to a broader spectrum, including hybrid organic-inorganic HaPs and even 2D perovskite structures, which have different behavior of gaps and various anharmonic fluctuations within the potential energy surface. Consequently, our findings could help to tailor HaP materials for enhanced optoelectronic applications by understanding the anharmonic effects. Theoretically, HaPs are a great platform to study the electron-phonon interaction of systems with anharmonic fluctuations. This research paves the way for a deeper comprehension of other materials known for their strong anharmonic behaviors, such as oxide perovskites, thermoelectric materials, and ion conductors, potentially unlocking new theoretical frameworks that can better describe their functional properties.

In the last part, our research focused on the overdamped phonon modes and electronic properties within the cubic phase of $CsPbBr_3$, offering a novel perspective to understand the impact of anharmonic behavior. We have studied the role of transient low-symmetry structures in the high-temperature phase by separating the contribution of fast and slow fluctuations on the band gap. It demonstrated the importance of considering slow fluctu-

ations between the local configurations in this system. Using the damped harmonic oscillator (DHO) model, we have associated these fluctuations with the overdamped phonon modes measured in experiments. The breakdown of the quasi-particle phonon picture showed the limitations of conventional phonon-based computational methods in accurately capturing the complex dynamics of overdamped systems, prompting the development of an augmented MC method. This novel approach, designed to embrace the non-Gaussian distributions characteristic of complex potential energy landscapes, marked a step forward in accurately modeling anharmonic fluctuations within halide perovskites. Based on this understanding of anharmonicity, we can classify the anharmonic materials and disentangle the phonon contribution to band gaps. It provided a general theoretical framework for understanding the electron-phonon coupling in anharmonic materials.

Our research on the influence of overdamped phonon dynamics on electronic properties shows that the anharmonic dynamics of halide perovskites are special with complex potential energy surfaces. We introduce the augmented MC method that better describes the dynamics by considering the potential energy beyond second-order, offering a promising direction for enhancing the accuracy of electronic property predictions. Furthermore, our method disentangles the phonon contributions into harmonic, higher-order anharmonic, and cross-anharmonic terms. We highlight the role of each term in modeling materials with overdamped modes. This approach provides a new perspective on electron-phonon coupling in anharmonic systems. By understanding the dynamic contribution to the optoelectronic behaviors of each term in the normal mode expansion, we are able to further develop computational methods and optimize halide perovskite-based optoelectronic devices.

In summary, this work unravels the connection between the structural dynamics and optoelectronic properties of halide perovskites, focusing on the role of anharmonicity and overdamped phonon modes. As illustrated in Figure 4.1, we establish a framework that connects microscopic structural phenomena, such as transient low-symmetry structures and two time scales in fluctuations, with the optoelectronic performance of halide perovskites, especially the band gap. It helps us to grasp the physical mechanism behind the connection and enables us to optimize the design and application of these materials in optoelectronics.

Building on the insights presented in this work, we now turn to outlooks for possible future research. One area for future research lies in refining computational methodologies. The augmented Monte Carlo (MC) method introduced here ignores the interaction between normal modes and starts from a potential well of a single normal mode coordinates. It is possible to use two or more normal mode coordinates to describe the potential energy surface in higher dimensions, which would allow us to study the interaction between normal modes. Additionally, the development of the machine learning force field enables us to study materials with a larger size and longer simulation time [184, 64, 42]. In this work, we mainly use time correlation functions, like velocity autocorrelation functions, to analyze the MD data. However, the application of spatial correlation functions is often restricted by the limited size of the supercells. The machine learning approach enables us to study the spatial correlation with a characteristic length much larger than the local disorder. Besides accelerating MD, the machine learning model can provide deeper insights into the

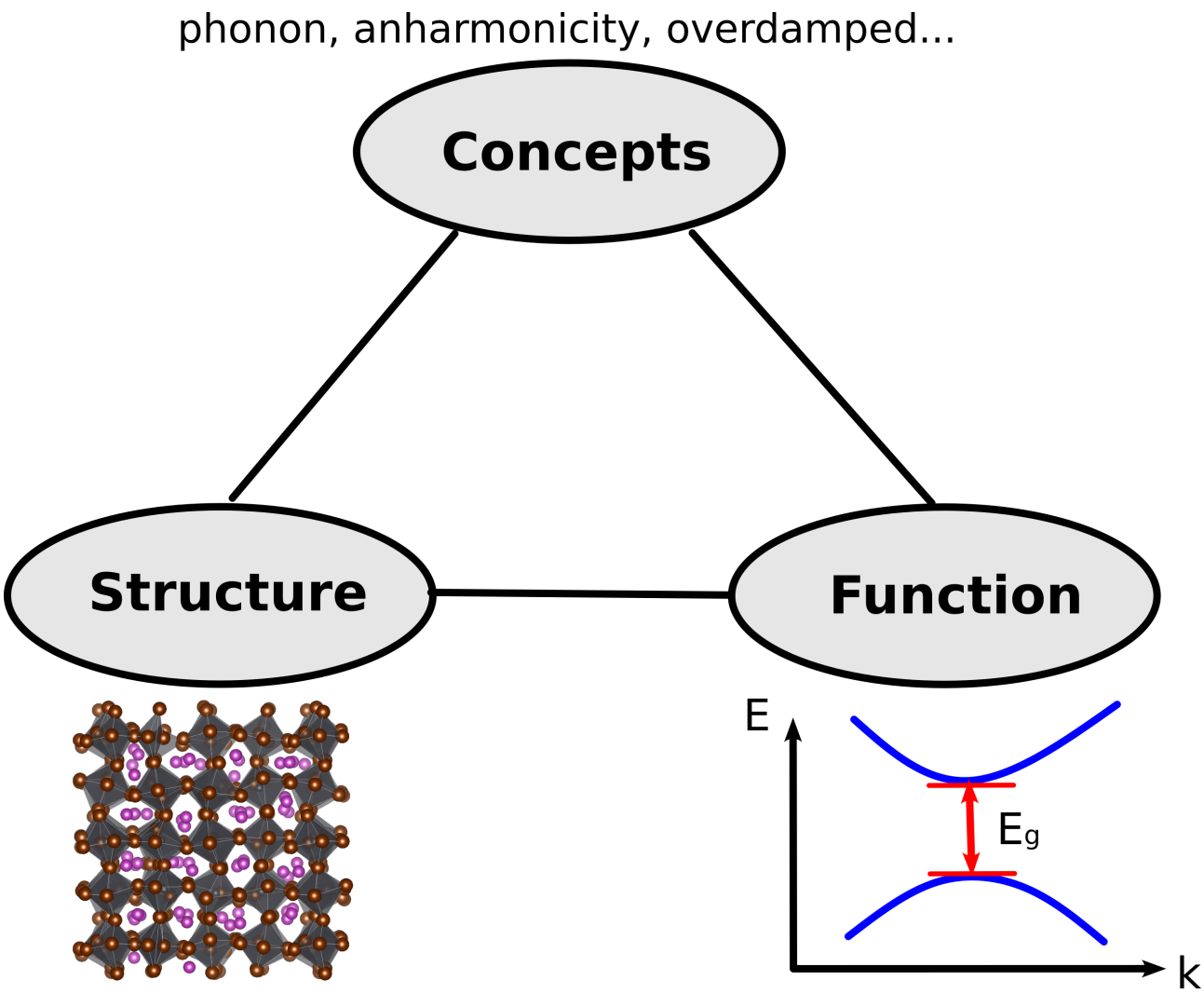

Figure 4.1 Schematic illustration of establishing a connection between the microscopic structural dynamics of halide perovskites and their macroscopic functional properties through theoretical concepts.

complex anharmonic effects and phonon dynamics within halide perovskites. Using unsupervised learning, it is possible to uncover patterns that are not apparent in systems with complicated dynamics such as halide perovskites and generate new perspectives on the dynamical influence of functional properties [185, 186, 187].

Another area for future research lies in expanding our study on lattice dynamics to a broader range of materials as well as functional properties. We have demonstrated the coupling between A-site and X-site dynamics in inorganic perovskites. With an organic molecule occupying the A-site in hybrid perovskites, this interaction may have different behavior and be even more interesting in mixed perovskites to tailor the properties [110, 188]. With their unique quantum confinement and surface phenomena, the anharmonic dynamics in 2D perovskites is another exciting frontier for future research [163, 189]. In parallel, the impact of dynamics on other functional properties, such as carrier mobility and thermal conductivity, requires further investigation. A deeper understanding of carrier mobility within these materials can illuminate pathways to enhance

charge transport mechanisms, crucial for improving device efficiency and performance. Recent research also stressed the importance of the anharmonic motion in molecular crystals [190] and superionic battery materials [191, 192, 193, 194]. Similarly, investigating thermal conductivity is appealing for thermoelectric materials [54, 195, 196, 197].

Finally, the last part for future research is to precisely calculate observables that can be directly compared with experimental spectroscopy measurements. This trajectory involves developing methodologies to calculate correlation functions that describe the dynamic behavior within these materials and provide theoretical spectra for spectroscopic techniques such as infrared (IR) or Raman spectroscopy [198, 199, 200]. Another task is to develop approaches to evaluate spectral functions that provide insights into the many-body interactions within a material and compare them to techniques such as angle-resolved photoemission spectroscopy (ARPES) [201, 60] or neutron scattering [202, 23]. Therefore we can bridge the gap between theoretical predictions and experimental observations to validate theoretical models and facilitate the engineering in experiments.

Bibliography

[1] Joel Millward-Hopkins, Julia K. Steinberger, Narasimha D. Rao, and Yannick Oswald. Providing decent living with minimum energy: A global scenario. *Glob. Environ. Chang.*, 65:102168, November 2020.

[2] Nico Wunderling, Ricarda Winkelmann, Johan Rockström, Sina Loriani, David I. Armstrong McKay, Paul D. L. Ritchie, Boris Sakschewski, and Jonathan F. Donges. Global warming overshoots increase risks of climate tipping cascades in a network model. *Nat. Clim. Chang.*, 13(1):75–82, January 2023.

[3] World Energy Outlook 2023 – Analysis. https://www.iea.org/reports/world-energy-outlook-2023.

[4] Net Zero Roadmap: A Global Pathway to Keep the 1.5 °C Goal in Reach – Analysis. https://www.iea.org/reports/net-zero-roadmap-a-global-pathway-to-keep-the-15-0c-goal-in-reach.

[5] Corsin Battaglia, Andres Cuevas, and Stefaan De Wolf. High-efficiency crystalline silicon solar cells: Status and perspectives. *Energy Environ. Sci.*, 9(5):1552–1576, 2016.

[6] Hao Lin, Miao Yang, Xiaoning Ru, Genshun Wang, Shi Yin, Fuguo Peng, Chengjian Hong, Minghao Qu, Junxiong Lu, Liang Fang, Can Han, Paul Procel, Olindo Isabella, Pingqi Gao, Zhenguo Li, and Xixiang Xu. Silicon heterojunction solar cells with up to 26.81% efficiency achieved by electrically optimized nanocrystalline-silicon hole contact layers. *Nat Energy*, 8(8):789–799, August 2023.

[7] Neeraj Kant and Pushpendra Singh. Review of next generation photovoltaic solar cell technology and comparative materialistic development. *Mater. Today Proc.*, 56:3460–3470, January 2022.

[8] Priyanka Roy, Aritra Ghosh, Fraser Barclay, Ayush Khare, and Erdem Cuce. Perovskite Solar Cells: A Review of the Recent Advances. *Coatings*, 12(8):1089, August 2022.

[9] Mark Peplow. A new kind of solar cell is coming: Is it the future of green energy? *Nature*, 623(7989):902–905, November 2023.

[10] Akihiro Kojima, Kenjiro Teshima, Yasuo Shirai, and Tsutomu Miyasaka. Organometal Halide Perovskites as Visible-Light Sensitizers for Photovoltaic Cells. *J. Am. Chem. Soc.*, 131(17):6050–6051, May 2009.

[11] Best Research-Cell Efficiency Chart. https://www.nrel.gov/pv/cell-efficiency.html.

[12] Hui Li and Wei Zhang. Perovskite Tandem Solar Cells: From Fundamentals to Commercial Deployment. *Chem. Rev.*, 120(18):9835–9950, September 2020.

[13] William Shockley and Hans J. Queisser. Detailed Balance Limit of Efficiency of p-n Junction Solar Cells. *J. Appl. Phys.*, 32(3):510–519, June 2004.

[14] Ajay Kumar Jena, Ashish Kulkarni, and Tsutomu Miyasaka. Halide Perovskite Photovoltaics: Background, Status, and Future Prospects. *Chem. Rev.*, 119(5):3036–3103, March 2019.

[15] David A. Egger, Achintya Bera, David Cahen, Gary Hodes, Thomas Kirchartz, Leeor Kronik, Robert Lovrincic, Andrew M. Rappe, David R. Reichman, and Omer Yaffe. What Remains Unexplained about the Properties of Halide Perovskites? *Adv. Mater.*, 30(20):1800691, 2018.

[16] Andrei A. Bunaciu, Elena gabriela Udriştioiu, and Hassan Y. Aboul-Enein. X-Ray Diffraction: Instrumentation and Applications. *Crit. Rev. Anal. Chem.*, 45(4):289–299, October 2015.

[17] Xiangzhou Zhu, Sebastián Caicedo-Dávila, Christian Gehrmann, and David A. Egger. Probing the Disorder Inside the Cubic Unit Cell of Halide Perovskites from First-Principles. *ACS Appl. Mater. Interfaces*, 34:16, April 2022.

[18] Christian Gehrmann and David A. Egger. Dynamic shortening of disorder potentials in anharmonic halide perovskites. *Nat. Commun.*, 10(1):3141, July 2019.

[19] Maximilian J. Schilcher, Paul J. Robinson, David J. Abramovitch, Liang Z. Tan, Andrew M. Rappe, David R. Reichman, and David A. Egger. The Significance of Polarons and Dynamic Disorder in Halide Perovskites. *ACS Energy Lett.*, 6(6):2162–2173, June 2021.

[20] Xin-Gang Zhao, Zhi Wang, Oleksandr I. Malyi, and Alex Zunger. Effect of static local distortions vs. dynamic motions on the stability and band gaps of cubic oxide and halide perovskites. *Mater. Today*, 49:107–122, October 2021.

[21] Ruo Xi Yang, Jonathan M. Skelton, E. Lora da Silva, Jarvist M. Frost, and Aron Walsh. Spontaneous Octahedral Tilting in the Cubic Inorganic Cesium Halide Perovskites $CsSnX_3$ and $CsPbX_3$ (X = F, Cl, Br, I). *J. Phys. Chem. Lett.*, 8(19):4720–4726, October 2017.

[22] Stefan A. Seidl, Xiangzhou Zhu, Guy Reuveni, Sigalit Aharon, Christian Gehrmann, Sebastián Caicedo-Dávila, Omer Yaffe, and David A. Egger. Anharmonic fluctuations govern the band gap of halide perovskites. *Phys. Rev. Mater.*, 7(9):L092401, September 2023.

[23] T. Lanigan-Atkins, X. He, M. J. Krogstad, D. M. Pajerowski, D. L. Abernathy, Guangyong N. M. N. Xu, Zhijun Xu, D.-Y. Chung, M. G. Kanatzidis, S. Rosenkranz,

R. Osborn, and O. Delaire. Two-dimensional overdamped fluctuations of the soft perovskite lattice in $CsPbBr_3$. *Nat. Mater.*, 20(7):977–983, July 2021.

[24] Wissam A. Saidi, Samuel Poncé, and Bartomeu Monserrat. Temperature Dependence of the Energy Levels of Methylammonium Lead Iodide Perovskite from First-Principles. *J. Phys. Chem. Lett.*, 7(24):5247–5252, December 2016.

[25] Richard M. Martin. *Electronic Structure: Basic Theory and Practical Methods*. Cambridge University Press, Cambridge, 2004.

[26] M. Born and R. Oppenheimer. Zur Quantentheorie der Molekeln. *Ann. Phys.*, 389(20):457–484, 1927.

[27] Dominik Marx and Jürg Hutter. *Ab Initio Molecular Dynamics: Basic Theory and Advanced Methods*. Cambridge University Press, 1 edition, April 2009.

[28] Simone Pisana, Michele Lazzeri, Cinzia Casiraghi, Kostya S. Novoselov, A. K. Geim, Andrea C. Ferrari, and Francesco Mauri. Breakdown of the adiabatic Born–Oppenheimer approximation in graphene. *Nature Mater*, 6(3):198–201, March 2007.

[29] Feliciano Giustino. *Materials Modelling Using Density Functional Theory: Properties and Predictions*. Oxford University Press, Oxford, 1st ed edition, 2014.

[30] P. Hohenberg and W. Kohn. Inhomogeneous Electron Gas. *Phys. Rev.*, 136(3B):B864–B871, November 1964.

[31] W. Kohn and L. J. Sham. Self-Consistent Equations Including Exchange and Correlation Effects. *Phys. Rev.*, 140(4A):A1133–A1138, November 1965.

[32] D. M. Ceperley and B. J. Alder. Ground State of the Electron Gas by a Stochastic Method. *Phys. Rev. Lett.*, 45(7):566–569, August 1980.

[33] John P Perdew, Kieron Burke, and Matthias Ernzerhof. Generalized Gradient Approximation Made Simple. *Phys. Rev. Lett.*, 77(18):3865–3868, 1996.

[34] Aliaksandr V. Krukau, Oleg A. Vydrov, Artur F. Izmaylov, and Gustavo E. Scuseria. Influence of the exchange screening parameter on the performance of screened hybrid functionals. *J. Chem. Phys.*, 125(22):224106, December 2006.

[35] John P. Perdew, Matthias Ernzerhof, and Kieron Burke. Rationale for mixing exact exchange with density functional approximations. *J. Chem. Phys.*, 105(22):9982–9985, December 1996.

[36] P. J. Stephens, F. J. Devlin, C. F. Chabalowski, and M. J. Frisch. Ab Initio Calculation of Vibrational Absorption and Circular Dichroism Spectra Using Density Functional Force Fields. *J. Phys. Chem.*, 98(45):11623–11627, November 1994.

[37] D. R. Hartree. The Wave Mechanics of an Atom with a Non-Coulomb Central Field. Part II. Some Results and Discussion. *Math. Proc. Camb. Philos. Soc.*, 24(1):111–132, January 1928.

[38] V. Fock. Näherungsmethode zur Lösung des quantenmechanischen Mehrkörperproblems. *Z. Physik*, 61(1):126–148, January 1930.

[39] H. Ehrenreich and M. H. Cohen. Self-Consistent Field Approach to the Many-Electron Problem. *Phys. Rev.*, 115(4):786–790, August 1959.

[40] H. Hellmann. Zur Rolle der kinetischen Elektronenenergie für die zwischenatomaren Krüfte. *Z. Physik*, 85(3-4):180–190, March 1933.

[41] R. P. Feynman. Forces in Molecules. *Phys. Rev.*, 56(4):340–343, August 1939.

[42] Ryosuke Jinnouchi, Jonathan Lahnsteiner, Ferenc Karsai, Georg Kresse, and Menno Bokdam. Phase Transitions of Hybrid Perovskites Simulated by Machine-Learning Force Fields Trained on the Fly with Bayesian Inference. *Phys. Rev. Lett.*, 122(22):225701, June 2019.

[43] Loup Verlet. Computer "Experiments" on Classical Fluids. I. Thermodynamical Properties of Lennard-Jones Molecules. *Phys. Rev.*, 159(1):98–103, July 1967.

[44] Shuichi Nosé. A unified formulation of the constant temperature molecular dynamics methods. *J. Chem. Phys.*, 81(1):511–519, July 1984.

[45] William G. Hoover. Canonical dynamics: Equilibrium phase-space distributions. *Phys. Rev. A*, 31(3):1695–1697, March 1985.

[46] Michael P. Allen and Dominic J. Tildesley. *Computer Simulation of Liquids*. Oxford University PressOxford, 2 edition, June 2017.

[47] Hans C. Andersen. Molecular dynamics simulations at constant pressure and/or temperature. *J. Chem. Phys.*, 72(4):2384–2393, February 1980.

[48] Maxwell W. Terban and Simon J. L. Billinge. Structural Analysis of Molecular Materials Using the Pair Distribution Function. *Chem. Rev.*, 122(1):1208–1272, January 2022.

[49] Donald Allan McQuarrie. *Statistical Mechanics*. Harper's Chemistry Series. Harper Collins, New York, 1976.

[50] R E Dinnebier and S J L Billinge, editors. *Powder Diffraction: Theory and Practice*. Royal Society of Chemistry, Cambridge, 2008.

[51] Martin T. Dove. *Introduction to Lattice Dynamics*. Cambridge University Press, 1 edition, October 1993.

[52] Abraham Nitzan. *Chemical Dynamics in Condensed Phases: Relaxation, Transfer and Reactions in Condensed Molecular Systems*. Oxford Graduate Texts. Oxford University Press, Oxford ; New York, 2006.

[53] J. E. Turney, E. S. Landry, A. J. H. McGaughey, and C. H. Amon. Predicting phonon properties and thermal conductivity from anharmonic lattice dynamics calculations and molecular dynamics simulations. *Phys. Rev. B*, 79(6):064301, February 2009.

[54] Johan Klarbring, Olle Hellman, Igor A. Abrikosov, and Sergei I. Simak. Anharmonicity and Ultralow Thermal Conductivity in Lead-Free Halide Double Perovskites. *Phys. Rev. Lett.*, 125(4):045701, July 2020.

[55] Nina Shulumba, Olle Hellman, and Austin J. Minnich. Lattice Thermal Conductivity of Polyethylene Molecular Crystals from First-Principles Including Nuclear Quantum Effects. *Phys. Rev. Lett.*, 119(18):185901, October 2017.

[56] Matthew Z Mayers, Liang Z Tan, David A Egger, Andrew M Rappe, and David R Reichman. How Lattice and Charge Fluctuations Control Carrier Dynamics in Halide Perovskites. *Nano Lett.*, 18(12):8041–8046, 2018.

[57] Aryeh Gold-Parker, Peter M. Gehring, Jonathan M. Skelton, Ian C. Smith, Dan Parshall, Jarvist M. Frost, Hemamala I. Karunadasa, Aron Walsh, and Michael F. Toney. Acoustic phonon lifetimes limit thermal transport in methylammonium lead iodide. *Proc. Natl. Acad. Sci.*, 115(47):11905–11910, November 2018.

[58] J. Bardeen, L. N. Cooper, and J. R. Schrieffer. Theory of Superconductivity. *Phys. Rev.*, 108(5):1175–1204, December 1957.

[59] Elaine A. Moore Smart, Lesley E. Superconductivity. In *Solid State Chemistry*. CRC Press, 5 edition, 2020.

[60] Feliciano Giustino. Electron-phonon interactions from first principles. *Rev. Mod. Phys.*, 89(1):015003, February 2017.

[61] Bin Wei, Qiyang Sun, Chen Li, and Jiawang Hong. Phonon anharmonicity: A pertinent review of recent progress and perspective. *Sci. China Phys. Mech. Astron.*, 64(11):117001, November 2021.

[62] R.A. Cowley. The lattice dynamics of an anharmonic crystal. *Adv. Phys.*, 12(48):421–480, October 1963.

[63] A D Bruce and R A Cowley. Lattice dynamics of strontium titanate: Anharmonic interactions and structural phase transitions. *J. Phys. C: Solid State Phys.*, 6(15):2422–2440, August 1973.

[64] Erik Fransson, Petter Rosander, Fredrik Eriksson, J. Magnus Rahm, Terumasa Tadano, and Paul Erhart. Limits of the phonon quasi-particle picture at the cubic-to-tetragonal phase transition in halide perovskites. *Commun. Phys.*, 6(1):1–7, July 2023.

[65] Erik Fransson, Mattias Slabanja, Paul Erhart, and Göran Wahnström. Dynasor—A Tool for Extracting Dynamical Structure Factors and Current Correlation Functions from Molecular Dynamics Simulations. *Adv. Theory Simul.*, 4(2):2000240, 2021.

[66] Terumasa Tadano and Shinji Tsuneyuki. Self-consistent phonon calculations of lattice dynamical properties in cubic $SrTiO_3$ with first-principles anharmonic force constants. *Phys. Rev. B*, 92(5):054301, August 2015.

[67] P. Souvatzis, O. Eriksson, M. I. Katsnelson, and S. P. Rudin. Entropy Driven Stabilization of Energetically Unstable Crystal Structures Explained from First Principles Theory. *Phys. Rev. Lett.*, 100(9):095901, March 2008.

[68] Ion Errea, Matteo Calandra, and Francesco Mauri. Anharmonic free energies and phonon dispersions from the stochastic self-consistent harmonic approximation: Application to platinum and palladium hydrides. *Phys. Rev. B*, 89(6):064302, February 2014.

[69] Abel Carreras, Atsushi Togo, and Isao Tanaka. DynaPhoPy: A code for extracting phonon quasiparticles from molecular dynamics simulations. *Comput. Phys. Commun.*, 221:221–234, December 2017.

[70] Tao Sun, Dong-Bo Zhang, and Renata M. Wentzcovitch. Dynamic stabilization of cubic $casio_3$ perovskite at high temperatures and pressures from ab initio molecular dynamics. *Phys. Rev. B*, 89(9):094109, March 2014.

[71] Tao Sun, Xiao Shen, and Philip B. Allen. Phonon quasiparticles and anharmonic perturbation theory tested by molecular dynamics on a model system. *Phys. Rev. B*, 82(22):224304, December 2010.

[72] O. Hellman, I. A. Abrikosov, and S. I. Simak. Lattice dynamics of anharmonic solids from first principles. *Phys. Rev. B*, 84(18):180301, November 2011.

[73] Olle Hellman and I. A. Abrikosov. Temperature-dependent effective third-order interatomic force constants from first principles. *Phys. Rev. B*, 88(14):144301, October 2013.

[74] Olle Hellman, Peter Steneteg, I. A. Abrikosov, and S. I. Simak. Temperature dependent effective potential method for accurate free energy calculations of solids. *Phys. Rev. B*, 87(10):104111, March 2013.

[75] Maxwell D. Radin, John C. Thomas, and Anton Van Der Ven. Order-disorder versus displacive transitions in Jahn-Teller active layered materials. *Phys. Rev. Mater.*, 4(4):043601, April 2020.

[76] P A Fleury. The Effects of Soft Modes on the Structure and Properties of Materials. *Annu. Rev. Mater. Sci.*, 6(1):157–180, August 1976.

[77] W. Cochran. Crystal stability and the theory of ferroelectricity. *Adv. Phys.*, 9(36):387–423, October 1960.

[78] J. F. Scott. Soft-mode spectroscopy: Experimental studies of structural phase transitions. *Rev. Mod. Phys.*, 46(1):83–128, January 1974.

[79] R.A. Cowley. Structural phase transitions I. Landau theory. *Advances in Physics*, 29(1):1–110, February 1980.

[80] G Venkataraman. Soft modes and structural phase transitions. *Bull. Mater. Sci.*, 1(3-4):129–170, December 1979.

[81] Bartomeu Monserrat. Electron–phonon coupling from finite differences. *J. Phys.: Condens. Matter*, 30(8):083001, February 2018.

[82] Melvin Lax. The Franck-Condon Principle and Its Application to Crystals. *J. Chem. Phys.*, 20(11):1752–1760, November 1952.

[83] Christopher E Patrick and Feliciano Giustino. Unified theory of electron–phonon renormalization and phonon-assisted optical absorption. *J. Phys.: Condens. Matter*, 26(36):365503, September 2014.

[84] S. Poncé, Y. Gillet, J. Laflamme Janssen, A. Marini, M. Verstraete, and X. Gonze. Temperature dependence of the electronic structure of semiconductors and insulators. *J. Chem. Phys.*, 143(10):102813, September 2015.

[85] Marios Zacharias, George Volonakis, Feliciano Giustino, and Jacky Even. Anharmonic lattice dynamics via the special displacement method. *Phys. Rev. B*, 108(3):035155, July 2023.

[86] S. Poncé, G. Antonius, Y. Gillet, P. Boulanger, J. Laflamme Janssen, A. Marini, M. Côté, and X. Gonze. Temperature dependence of electronic eigenenergies in the adiabatic harmonic approximation. *Phys. Rev. B*, 90(21):214304, December 2014.

[87] P B Allen and V Heine. Theory of the temperature dependence of electronic band structures. *J. Phys. C: Solid State Phys.*, 9(12):2305–2312, June 1976.

[88] P. B. Allen and M. Cardona. Theory of the temperature dependence of the direct gap of germanium. *Phys. Rev. B*, 23(4):1495–1505, February 1981.

[89] Christopher E. Patrick, Karsten W. Jacobsen, and Kristian S. Thygesen. Anharmonic stabilization and band gap renormalization in the perovskite cssni$_3$. *Phys. Rev. B*, 92(20):201205, November 2015.

[90] Yu-Ning Wu, Wissam A. Saidi, Jeffrey K. Wuenschell, Terumasa Tadano, Paul Ohodnicki, Benjamin Chorpening, and Yuhua Duan. Anharmonicity Explains Temperature Renormalization Effects of the Band Gap in SrTiO$_3$. *J. Phys. Chem. Lett.*, 11(7):2518–2523, April 2020.

[91] Jonathan M. Skelton, Lee A. Burton, Stephen C. Parker, Aron Walsh, Chang-Eun Kim, Aloysius Soon, John Buckeridge, Alexey A. Sokol, C. Richard A. Catlow, Atsushi Togo, and Isao Tanaka. Anharmonicity in the High-Temperature $Cmcm$ Phase of SnSe: Soft Modes and Three-Phonon Interactions. *Phys. Rev. Lett.*, 117(7):075502, August 2016.

[92] R. A. Evarestov, E. A. Kotomin, A. Senocrate, R. K. Kremer, and J. Maier. First-principles comparative study of perfect and defective CsPbX$_3$ (X = Br, I) crystals. *Phys. Chem. Chem. Phys.*, 22(7):3914–3920, 2020.

[93] V. M. Goldschmidt. Die Gesetze der Krystallochemie. *Naturwissenschaften*, 14(21):477–485, May 1926.

[94] W. Travis, E. N. K. Glover, H. Bronstein, D. O. Scanlon, and R. G. Palgrave. On the application of the tolerance factor to inorganic and hybrid halide perovskites: A revised system. *Chem. Sci.*, 7(7):4548–4556, 2016.

[95] Edson Meyer, Dorcas Mutukwa, Nyengerai Zingwe, and Raymond Taziwa. Lead-Free Halide Double Perovskites: A Review of the Structural, Optical, and Stability Properties as Well as Their Viability to Replace Lead Halide Perovskites. *Metals*, 8(9):667, September 2018.

[96] Xiaotong Li, Justin M. Hoffman, and Mercouri G. Kanatzidis. The 2D Halide Perovskite Rulebook: How the Spacer Influences Everything from the Structure to Optoelectronic Device Efficiency. *Chem. Rev.*, 121(4):2230–2291, February 2021.

[97] Silvia Colella, Edoardo Mosconi, Paolo Fedeli, Andrea Listorti, Francesco Gazza, Fabio Orlandi, Patrizia Ferro, Tullo Besagni, Aurora Rizzo, Gianluca Calestani, Giuseppe Gigli, Filippo De Angelis, and Roberto Mosca. $MAPbI_{3-x}Cl_x$ Mixed Halide Perovskite for Hybrid Solar Cells: The Role of Chloride as Dopant on the Transport and Structural Properties. *Chem. Mater.*, 25(22):4613–4618, November 2013.

[98] David P. McMeekin, Golnaz Sadoughi, Waqaas Rehman, Giles E. Eperon, Michael Saliba, Maximilian T. Hörantner, Amir Haghighirad, Nobuya Sakai, Lars Korte, Bernd Rech, Michael B. Johnston, Laura M. Herz, and Henry J. Snaith. A mixed-cation lead mixed-halide perovskite absorber for tandem solar cells. *Science*, 351(6269):151–155, January 2016.

[99] Alexander N. Beecher, Octavi E. Semonin, Jonathan M. Skelton, Jarvist M. Frost, Maxwell W. Terban, Haowei Zhai, Ahmet Alatas, Jonathan S. Owen, Aron Walsh, and Simon J. L. Billinge. Direct Observation of Dynamic Symmetry Breaking above Room Temperature in Methylammonium Lead Iodide Perovskite. *ACS Energy Lett.*, 1(4):880–887, October 2016.

[100] Omer Yaffe, Yinsheng Guo, Liang Z. Tan, David A. Egger, Trevor Hull, Constantinos C. Stoumpos, Fan Zheng, Tony F. Heinz, Leeor Kronik, Mercouri G. Kanatzidis, Jonathan S. Owen, Andrew M. Rappe, Marcos A. Pimenta, and Louis E. Brus. Local Polar Fluctuations in Lead Halide Perovskite Crystals. *Phys. Rev. Lett.*, 118(13):136001, March 2017.

[101] Bayrammurad Saparov and David B. Mitzi. Organic–Inorganic Perovskites: Structural Versatility for Functional Materials Design. *Chem. Rev.*, 116(7):4558–4596, April 2016.

[102] Chr Kn Møller. Crystal structure and photoconductivity of cæsium plumbohalides. *Nature*, 182(4647):1436, 1958.

[103] Dieter Weber. $CH_3NH_3PbX_3$, ein Pb (II)-system mit kubischer perowskitstruktur $CH_3NH_3PbX_3$, a Pb (II)-system with cubic perovskite structure. *Z. Für Naturforsch B*, 33(12):1443–1445, 1978.

[104] Richard J. Worhatch, Hyun Jeong Kim, Ian P. Swainson, André L. Yonkeu, and Simon J.L. Billinge. Study of local structure in selected organic-inorganic perovskites in the Pm$\bar{3}$m phase. *Chem. Mater.*, 20(4):1272–1277, 2008.

[105] Andrea Bernasconi and Lorenzo Malavasi. Direct evidence of permanent octahedra distortion in mapbbr$_3$ hybrid perovskite. *ACS Energy Lett.*, 2(4):863–868, April 2017.

[106] Katharine Page, Joan E. Siewenie, Paolo Quadrelli, and Lorenzo Malavasi. Short-Range Order of Methylammonium and Persistence of Distortion at the Local Scale in MAPbBr$_3$ Hybrid Perovskite. *Angew. Chem. Int. Ed.*, 55(46):14320–14324, 2016.

[107] Daniel B. Straus, Shu Guo, AM Milinda Abeykoon, and Robert J. Cava. Understanding the Instability of the Halide Perovskite CsPbI 3 through Temperature-Dependent Structural Analysis. *Adv. Mater.*, 32(32):2001069, August 2020.

[108] Lingyuan Gao, Lena Yadgarov, Rituraj Sharma, Roman Korobko, Kyle M. McCall, Douglas H. Fabini, Constantinos C. Stoumpos, Mercouri G. Kanatzidis, Andrew M. Rappe, and Omer Yaffe. Metal cation s lone-pairs increase octahedral tilting instabilities in halide perovskites. *Mater. Adv.*, 2(14):4610–4616, 2021.

[109] Harishchandra Singh, Ruixiang Fei, Yevgeny Rakita, Michael Kulbak, David Cahen, Andrew M. Rappe, and Anatoly I. Frenkel. Origin of the anomalous Pb-Br bond dynamics in formamidinium lead bromide perovskites. *Phys. Rev. B*, 101(5):054302, February 2020.

[110] Dibyajyoti Ghosh, Philip Walsh Atkins, M. Saiful Islam, Alison B. Walker, and Christopher Eames. Good Vibrations: Locking of Octahedral Tilting in Mixed-Cation Iodide Perovskites for Solar Cells. *ACS Energy Lett.*, 2(10):2424–2429, October 2017.

[111] Christian Gehrmann, Sebastián Caicedo-Dávila, Xiangzhou Zhu, and David A. Egger. Transversal Halide Motion Intensifies Band-To-Band Transitions in Halide Perovskites. *Adv. Sci.*, 9(16):2200706, 2022.

[112] Constantinos C. Stoumpos, Christos D. Malliakas, John A. Peters, Zhifu Liu, Maria Sebastian, Jino Im, Thomas C. Chasapis, Arief C. Wibowo, Duck Young Chung, Arthur J. Freeman, Bruce W. Wessels, and Mercouri G. Kanatzidis. Crystal Growth of the Perovskite Semiconductor CsPbBr$_3$: A New Material for High-Energy Radiation Detection. *Cryst. Growth Des.*, 13(7):2722–2727, July 2013.

[113] Michael Kulbak, David Cahen, and Gary Hodes. How Important Is the Organic Part of Lead Halide Perovskite Photovoltaic Cells? Efficient CsPbBr$_3$ Cells. *J. Phys. Chem. Lett.*, 6(13):2452–2456, July 2015.

[114] M. Puppin, S. Polishchuk, N. Colonna, A. Crepaldi, D. N. Dirin, O. Nazarenko, R. De Gennaro, G. Gatti, S. Roth, T. Barillot, L. Poletto, R. P. Xian, L. Rettig, M. Wolf, R. Ernstorfer, M. V. Kovalenko, N. Marzari, M. Grioni, and M. Chergui. Evidence of Large Polarons in Photoemission Band Mapping of the Perovskite Semiconductor cspbbr$_3$. *Phys. Rev. Lett.*, 124(20):206402, May 2020.

[115] Shunsuke Hirotsu, Jimpei Harada, Masashi Iizumi, and Kazuo Gesi. Structural Phase Transitions in $CsPbBr_3$. *J. Phys. Soc. Jpn.*, 37(5):1393–1398, November 1974.

[116] G. Kresse and J. Furthmüller. Efficient iterative schemes for ab initio total-energy calculations using a plane-wave basis set. *Phys. Rev. B*, 54(16):11169–11186, October 1996.

[117] G. Kresse and D. Joubert. From ultrasoft pseudopotentials to the projector augmented-wave method. *Phys. Rev. B*, 59(3):1758–1775, January 1999.

[118] Alexandre Tkatchenko and Matthias Scheffler. Accurate Molecular Van Der Waals Interactions from Ground-State Electron Density and Free-Atom Reference Data. *Phys. Rev. Lett.*, 102(7):073005, February 2009.

[119] H. Beck, C. Gehrmann, and D. A. Egger. Structure and binding in halide perovskites: Analysis of static and dynamic effects from dispersion-corrected density functional theory. *APL Mater.*, 7(2):021108, February 2019.

[120] Johan Klarbring. Low-energy paths for octahedral tilting in inorganic halide perovskites. *Phys. Rev. B*, 99(10):104105, March 2019.

[121] N. Zhang, M. Paściak, A. M. Glazer, J. Hlinka, M. Gutmann, H. A. Sparkes, T. R. Welberry, A. Majchrowski, K. Roleder, Y. Xie, and Z.-G. Ye. A neutron diffuse scattering study of $PbZrO_3$ and Zr-rich $PbZr_{1-x}TixO_3$. *J Appl Cryst*, 48(6):1637–1644, December 2015.

[122] Joshua Young and James M. Rondinelli. Octahedral Rotation Preferences in Perovskite Iodides and Bromides. *J. Phys. Chem. Lett.*, 7(5):918–922, 2016.

[123] Hyojung Kim, Ji Su Han, Jaeho Choi, Soo Young Kim, and Ho Won Jang. Halide Perovskites for Applications beyond Photovoltaics. *Small Methods*, 2(3):1700310, 2018.

[124] Brandon R. Sutherland and Edward H. Sargent. Perovskite photonic sources. *Nat. Photon*, 10(5):295–302, May 2016.

[125] Kebin Lin, Jun Xing, Li Na Quan, F. Pelayo García de Arquer, Xiwen Gong, Jianxun Lu, Liqiang Xie, Weijie Zhao, Di Zhang, Chuanzhong Yan, Wenqiang Li, Xinyi Liu, Yan Lu, Jeffrey Kirman, Edward H. Sargent, Qihua Xiong, and Zhanhua Wei. Perovskite light-emitting diodes with external quantum efficiency exceeding 20 per cent. *Nature*, 562(7726):245–248, October 2018.

[126] Guoxin Li, Yukun Wang, Lixiang Huang, and Wenhong Sun. Research Progress of High-Sensitivity Perovskite Photodetectors: A Review of Photodetectors: Noise, Structure, and Materials. *ACS Appl. Electron. Mater.*, 4(4):1485–1505, April 2022.

[127] Qing Zhang, Qiuyu Shang, Rui Su, T. Thu Ha Do, and Qihua Xiong. Halide Perovskite Semiconductor Lasers: Materials, Cavity Design, and Low Threshold. *Nano Lett.*, 21(5):1903–1914, March 2021.

[128] Giles E. Eperon, Samuel D. Stranks, Christopher Menelaou, Michael B. Johnston, Laura M. Herz, and Henry J. Snaith. Formamidinium lead trihalide: A broadly tunable perovskite for efficient planar heterojunction solar cells. *Energy Environ. Sci.*, 7(3):982–988, February 2014.

[129] Yaoyao Li, Yao Lu, Xiaomin Huo, Dong Wei, Juan Meng, Jie Dong, Bo Qiao, Suling Zhao, Zheng Xu, and Dandan Song. Bandgap tuning strategy by cations and halide ions of lead halide perovskites learned from machine learning. *RSC Adv.*, 11(26):15688–15694, 2021.

[130] Stefaan De Wolf, Jakub Holovsky, Soo-Jin Moon, Philipp Löper, Bjoern Niesen, Martin Ledinsky, Franz-Josef Haug, Jun-Ho Yum, and Christophe Ballif. Organometallic Halide Perovskites: Sharp Optical Absorption Edge and Its Relation to Photovoltaic Performance. *J. Phys. Chem. Lett.*, 5(6):1035–1039, March 2014.

[131] Chuanjiang Qin, Toshinori Matsushima, William J. Potscavage, Atula S. D. Sandanayaka, Matthew R. Leyden, Fatima Bencheikh, Kenichi Goushi, Fabrice Mathevet, Benoît Heinrich, Go Yumoto, Yoshihiko Kanemitsu, and Chihaya Adachi. Triplet management for efficient perovskite light-emitting diodes. *Nat. Photonics*, 14(2):70–75, February 2020.

[132] Samuel D. Stranks, Giles E. Eperon, Giulia Grancini, Christopher Menelaou, Marcelo J. P. Alcocer, Tomas Leijtens, Laura M. Herz, Annamaria Petrozza, and Henry J. Snaith. Electron-Hole Diffusion Lengths Exceeding 1 Micrometer in an Organometal Trihalide Perovskite Absorber. *Science*, 342(6156):341–344, October 2013.

[133] Laura M. Herz. Charge-Carrier Mobilities in Metal Halide Perovskites: Fundamental Mechanisms and Limits. *ACS Energy Lett.*, 2(7):1539–1548, July 2017.

[134] In Chung, Jung-Hwan Song, Jino Im, John Androulakis, Christos D. Malliakas, Hao Li, Arthur J. Freeman, John T. Kenney, and Mercouri G. Kanatzidis. $CsSnI_3$: Semiconductor or Metal? High Electrical Conductivity and Strong Near-Infrared Photoluminescence from a Single Material. High Hole Mobility and Phase-Transitions. *J. Am. Chem. Soc.*, 134(20):8579–8587, May 2012.

[135] Yu Bi, Eline M. Hutter, Yanjun Fang, Qingfeng Dong, Jinsong Huang, and Tom J. Savenije. Charge Carrier Lifetimes Exceeding 15 Ms in Methylammonium Lead Iodide Single Crystals. *J. Phys. Chem. Lett.*, 7(5):923–928, March 2016.

[136] Xihan Chen, Haipeng Lu, Ye Yang, and Matthew C. Beard. Excitonic Effects in Methylammonium Lead Halide Perovskites. *J. Phys. Chem. Lett.*, 9(10):2595–2603, May 2018.

[137] Laura M. Herz. How Lattice Dynamics Moderate the Electronic Properties of Metal-Halide Perovskites. *J. Phys. Chem. Lett.*, 9(23):6853–6863, December 2018.

[138] Kyle T. Munson, John R. Swartzfager, and John B. Asbury. Lattice Anharmonicity: A Double-Edged Sword for 3D Perovskite-Based Optoelectronics. *ACS Energy Lett.*, 4(8):1888–1897, August 2019.

[139] Kyle T. Munson, Grayson S. Doucette, Eric R. Kennehan, John R. Swartzfager, and John B. Asbury. Vibrational Probe of the Structural Origins of Slow Recombination in Halide Perovskites. *J. Phys. Chem. C*, 123(12):7061–7073, March 2019.

[140] Peter Würfel and Uli Würfel. *Physics of Solar Cells: From Basic Principles to Advanced Concepts*. Physics Textbook. Wiley-VCH, Weinheim, 2nd, updated and expanded ed edition, 2009.

[141] Wissam A. Saidi and Ali Kachmar. Effects of Electron–Phonon Coupling on Electronic Properties of Methylammonium Lead Iodide Perovskites. *J. Phys. Chem. Lett.*, 9(24):7090–7097, December 2018.

[142] Adrián Francisco-López, Bethan Charles, Oliver J. Weber, M. Isabel Alonso, Miquel Garriga, Mariano Campoy-Quiles, Mark T. Weller, and Alejandro R. Goñi. Equal Footing of Thermal Expansion and Electron–Phonon Interaction in the Temperature Dependence of Lead Halide Perovskite Band Gaps. *J. Phys. Chem. Lett.*, 10(11):2971–2977, June 2019.

[143] Ling-yi Huang and Walter R. L. Lambrecht. Electronic band structure, phonons, and exciton binding energies of halide perovskites $CsSnCl_3$, $CsSnBr_3$, and $CsSnI_3$. *Phys. Rev. B*, 88(16):165203, October 2013.

[144] Chonglong Yu, Zhuo Chen, Jian J. Wang, William Pfenninger, Nemanja Vockic, John T. Kenney, and Kai Shum. Temperature dependence of the band gap of perovskite semiconductor compound $CsSnI_3$. *J. Appl. Phys.*, 110(6):063526, September 2011.

[145] Gurivi Reddy Yettapu, Debnath Talukdar, Sohini Sarkar, Abhishek Swarnkar, Angshuman Nag, Prasenjit Ghosh, and Pankaj Mandal. Terahertz Conductivity within Colloidal $CsPbBr_3$ Perovskite Nanocrystals: Remarkably High Carrier Mobilities and Large Diffusion Lengths. *Nano Lett.*, 16(8):4838–4848, August 2016.

[146] Giovanni Mannino, Ioannis Deretzis, Emanuele Smecca, Antonino La Magna, Alessandra Alberti, Davide Ceratti, and David Cahen. Temperature-Dependent Optical Band Gap in $CsPbBr_3$, $MAPbBr_3$, and $FAPbBr_3$ Single Crystals. *J. Phys. Chem. Lett.*, 11(7):2490–2496, April 2020.

[147] Byungkyun Kang and Koushik Biswas. Exploring Polaronic, Excitonic Structures and Luminescence in Cs_4PbBr_6/$CsPbBr_3$. *J. Phys. Chem. Lett.*, 9(4):830–836, February 2018.

[148] G. Murtaza and Iftikhar Ahmad. First principle study of the structural and optoelectronic properties of cubic perovskites $CsPbM_3$ (M=Cl, Br, I). *Physica B: Condensed Matter*, 406(17):3222–3229, September 2011.

[149] Tomáš Bučko, Sébastien Lebègue, János G. Ángyán, and Jürgen Hafner. Extending the applicability of the Tkatchenko-Scheffler dispersion correction via iterative Hirshfeld partitioning. *J. Chem. Phys.*, 141(3):034114, July 2014.

[150] Atsushi Togo and Isao Tanaka. First principles phonon calculations in materials science. *Scr. Mater.*, 108:1–5, November 2015.

[151] A. Poglitsch and D. Weber. Dynamic disorder in methylammoniumtrihalogenoplumbates (II) observed by millimeter-wave spectroscopy. *J. Chem. Phys.*, 87(11):6373–6378, December 1987.

[152] Yinsheng Guo, Omer Yaffe, Trevor D. Hull, Jonathan S. Owen, David R. Reichman, and Louis E. Brus. Dynamic emission Stokes shift and liquid-like dielectric solvation of band edge carriers in lead-halide perovskites. *Nat Commun*, 10(1):1175, March 2019.

[153] Adam D. Wright, Carla Verdi, Rebecca L. Milot, Giles E. Eperon, Miguel A. Pérez-Osorio, Henry J. Snaith, Feliciano Giustino, Michael B. Johnston, and Laura M. Herz. Electron–phonon coupling in hybrid lead halide perovskites. *Nat. Commun.*, 7(1):11755, May 2016.

[154] Jenya Tilchin, Dmitry N. Dirin, Georgy I. Maikov, Aldona Sashchiuk, Maksym V. Kovalenko, and Efrat Lifshitz. Hydrogen-like Wannier–Mott Excitons in Single Crystal of Methylammonium Lead Bromide Perovskite. *ACS Nano*, 10(6):6363–6371, June 2016.

[155] Edoardo Mosconi, Paolo Umari, and Filippo De Angelis. Electronic and optical properties of $MAPbX_3$ perovskites (X = I, Br, Cl): A unified DFT and GW theoretical analysis. *Phys. Chem. Chem. Phys.*, 18(39):27158–27164, October 2016.

[156] Jeremy L. Knutson, James D. Martin, and David B. Mitzi. Tuning the Band Gap in Hybrid Tin Iodide Perovskite Semiconductors Using Structural Templating. *Inorg. Chem.*, 44(13):4699–4705, June 2005.

[157] Anna Amat, Edoardo Mosconi, Enrico Ronca, Claudio Quarti, Paolo Umari, Md. K. Nazeeruddin, Michael Grätzel, and Filippo De Angelis. Cation-Induced Band-Gap Tuning in Organohalide Perovskites: Interplay of Spin–Orbit Coupling and Octahedra Tilting. *Nano Lett.*, 14(6):3608–3616, June 2014.

[158] Claudio Quarti, Edoardo Mosconi, James M. Ball, Valerio D'Innocenzo, Chen Tao, Sandeep Pathak, Henry J. Snaith, Annamaria Petrozza, and Filippo De Angelis. Structural and optical properties of methylammonium lead iodide across the tetragonal to cubic phase transition: Implications for perovskite solar cells. *Energy Environ. Sci.*, 9(1):155–163, 2016.

[159] Rituraj Sharma, Zhenbang Dai, Lingyuan Gao, Thomas M. Brenner, Lena Yadgarov, Jiahao Zhang, Yevgeny Rakita, Roman Korobko, Andrew M. Rappe, and Omer Yaffe. Elucidating the atomistic origin of anharmonicity in tetragonal $ch_3nh_3pbi_3$ with Raman scattering. *Phys. Rev. Mater.*, 4(9):092401, September 2020.

[160] Omer Yaffe, Alexey Chernikov, Zachariah M. Norman, Yu Zhong, Ajanthkrishna Velauthapillai, Arend van der Zande, Jonathan S. Owen, and Tony F. Heinz. Excitons in ultrathin organic-inorganic perovskite crystals. *Phys. Rev. B*, 92(4):045414, July 2015.

[161] Jonas D. Ziegler, Kai-Qiang Lin, Barbara Meisinger, Xiangzhou Zhu, Manuel Kober-Czerny, Pabitra K. Nayak, Cecilia Vona, Takashi Taniguchi, Kenji Watanabe, Claudia Draxl, Henry J. Snaith, John M. Lupton, David A. Egger, and Alexey Chernikov. Excitons at the Phase Transition of 2D Hybrid Perovskites. *ACS Photonics*, 9(11):3609–3616, November 2022.

[162] Teruya Ishihara, Jun Takahashi, and Takenari Goto. Optical properties due to electronic transitions in two-dimensional semiconductors ($CnH_{2n+1}NH_3)_2PbI_4$. *Phys. Rev. B*, 42(17):11099–11107, December 1990.

[163] Matan Menahem, Zhenbang Dai, Sigalit Aharon, Rituraj Sharma, Maor Asher, Yael Diskin-Posner, Roman Korobko, Andrew M. Rappe, and Omer Yaffe. Strongly Anharmonic Octahedral Tilting in Two-Dimensional Hybrid Halide Perovskites. *ACS Nano*, 15(6):10153–10162, June 2021.

[164] J. Harada, J. D. Axe, and G. Shirane. Neutron-Scattering Study of Soft Modes in cubic batio$_3$. *Phys. Rev. B*, 4(1):155–162, July 1971.

[165] Y Luspin, J L Servoin, and F Gervais. Soft mode spectroscopy in barium titanate. *J. Phys. C: Solid State Phys.*, 13(19):3761–3773, July 1980.

[166] M. Paściak, T. R. Welberry, J. Kulda, S. Leoni, and J. Hlinka. Dynamic Displacement Disorder of Cubic batio$_3$. *Phys. Rev. Lett.*, 120(16):167601, April 2018.

[167] A. C. Nunes, J. D. Axe, and G. Shirane. A neutron study of diffuse scattering in cubic $KNbO_3$. *Ferroelectrics*, 2(1):291–297, October 1971.

[168] M D Fontana, G Metrat, J L Servoin, and F Gervais. Infrared spectroscopy in knbo$_3$ through the successive ferroelectric phase transitions. *J. Phys. C: Solid State Phys.*, 17(3):483–514, January 1984.

[169] A. Heiming, W. Petry, J. Trampenau, M. Alba, C. Herzig, H. R. Schober, and G. Vogl. Phonon dispersion of the bcc phase of group-IV metals. II. bcc zirconium, a model case of dynamical precursors of martensitic transitions. *Phys. Rev. B*, 43(13):10948–10962, May 1991.

[170] W. Petry, A. Heiming, J. Trampenau, M. Alba, C. Herzig, H. R. Schober, and G. Vogl. Phonon dispersion of the bcc phase of group-IV metals. I. bcc titanium. *Phys. Rev. B*, 43(13):10933–10947, May 1991.

[171] Y. Fujii, S. Hoshino, Y. Yamada, and G. Shirane. Neutron-scattering study on phase transitions of CsPbcl$_3$. *Phys. Rev. B*, 9(10):4549–4559, May 1974.

[172] M. Songvilay, N. Giles-Donovan, M. Bari, Z.-G. Ye, J. L. Minns, M. A. Green, Guangyong Xu, P. M. Gehring, K. Schmalzl, W. D. Ratcliff, C. M. Brown, D. Chernyshov, W. Van Beek, S. Cochran, and C. Stock. Common acoustic phonon lifetimes in inorganic and hybrid lead halide perovskites. *Phys. Rev. Mater.*, 3(9):093602, September 2019.

[173] A. C. Ferreira, S. Paofai, A. Létoublon, J. Ollivier, S. Raymond, B. Hehlen, B. Rufflé, S. Cordier, C. Katan, J. Even, and P. Bourges. Direct evidence of weakly dispersed and strongly anharmonic optical phonons in hybrid perovskites. *Commun. Phys.*, 3(1):1–10, March 2020.

[174] C. Stock, M. Songvilay, P. M. Gehring, Guangyong Xu, and B. Roessli. Broadband critical dynamics in disordered lead-based perovskites. *J. Phys.: Condens. Matter*, 32(37):374012, June 2020.

[175] Nicholas J. Weadock, Peter M. Gehring, Aryeh Gold-Parker, Ian C. Smith, Hemamala I. Karunadasa, and Michael F. Toney. Test of the Dynamic-Domain and Critical Scattering Hypotheses in Cubic Methylammonium Lead Triiodide. *Phys. Rev. Lett.*, 125(7):075701, August 2020.

[176] Nicholas J. Weadock, Tyler C. Sterling, Julian A. Vigil, Aryeh Gold-Parker, Ian C. Smith, Ballal Ahammed, Matthew J. Krogstad, Feng Ye, David Voneshen, Peter M. Gehring, Andrew M. Rappe, Hans-Georg Steinrück, Elif Ertekin, Hemamala I. Karunadasa, Dmitry Reznik, and Michael F. Toney. The nature of dynamic local order in CH3NH3PbI$_3$ and CH3NH3PbBr$_3$. *Joule*, 7(5):1051–1066, May 2023.

[177] William J. Baldwin, Xia Liang, Johan Klarbring, Milos Dubajic, David Dell'Angelo, Christopher Sutton, Claudia Caddeo, Samuel D. Stranks, Alessandro Mattoni, Aron Walsh, and Gábor Csányi. Dynamic Local Structure in Caesium Lead Iodide: Spatial Correlation and Transient Domains. *Small*, 20(3):2303565, 2024.

[178] Jin-Jian Zhou, Olle Hellman, and Marco Bernardi. Electron-Phonon Scattering in the Presence of Soft Modes and Electron Mobility in SrTiO 3 Perovskite from First Principles. *Phys. Rev. Lett.*, 121(22):226603, November 2018.

[179] Dirk J. Kok, Klaus Irmscher, Martin Naumann, Christo Guguschev, Zbigniew Galazka, and Reinhard Uecker. Temperature-dependent optical absorption of SrTiO3. *Phys. Status Solidi A*, 212(9):1880–1887, 2015.

[180] Adi Cohen, Thomas M. Brenner, Johan Klarbring, Rituraj Sharma, Douglas H. Fabini, Roman Korobko, Pabitra K. Nayak, Olle Hellman, and Omer Yaffe. Diverging Expressions of Anharmonicity in Halide Perovskites. *Adv. Mater.*, 34(14):2107932, April 2022.

[181] D A Bruce and W G Stirling. The critical dynamics of $SrTiO_3$: A study of neutron- and Raman-determined soft-mode lineshapes. *J. Phys. C: Solid State Phys.*, 16(5):841–854, February 1983.

[182] S. M. Shapiro, J. D. Axe, G. Shirane, and T. Riste. Critical Neutron Scattering in $SrTiO_3$ and $KMnO_3$. *Phys. Rev. B*, 6(11):4332–4341, December 1972.

[183] G. Shirane and Y. Yamada. Lattice-Dynamical Study of the 110°K Phase Transition in $SrTiO_3$. *Phys. Rev.*, 177(2):858–863, January 1969.

[184] Jonathan Lahnsteiner and Menno Bokdam. Anharmonic lattice dynamics in large thermodynamic ensembles with machine-learning force fields: $CsPbBr_3$, a phonon liquid with Cs rattlers. *Phys. Rev. B*, 105(2):024302, January 2022.

[185] Sandip De, Albert P. Bartók, Gábor Csányi, and Michele Ceriotti. Comparing molecules and solids across structural and alchemical space. *Phys. Chem. Chem. Phys.*, 18(20):13754–13769, May 2016.

[186] Alex Rodriguez and Alessandro Laio. Clustering by fast search and find of density peaks. *Science*, 344(6191):1492–1496, June 2014.

[187] Andrew L. Ferguson, Athanassios Z. Panagiotopoulos, Pablo G. Debenedetti, and Ioannis G. Kevrekidis. Systematic determination of order parameters for chain dynamics using diffusion maps. *Proc. Natl. Acad. Sci.*, 107(31):13597–13602, August 2010.

[188] Chang Woo Myung, Jeonghun Yun, Geunsik Lee, and Kwang S. Kim. A New Perspective on the Role of A-Site Cations in Perovskite Solar Cells. *Adv. Energy Mater.*, 8(14):1702898, 2018.

[189] Paribesh Acharyya, Tanmoy Ghosh, Koushik Pal, Kaushik Kundu, Kewal Singh Rana, Juhi Pandey, Ajay Soni, Umesh V. Waghmare, and Kanishka Biswas. Intrinsically Ultralow Thermal Conductivity in Ruddlesden–Popper 2D Perovskite $Cs_2PbI_2Cl_2$: Localized Anharmonic Vibrations and Dynamic Octahedral Distortions. *J. Am. Chem. Soc.*, 142(36):15595–15603, September 2020.

[190] Antonios M. Alvertis and Edgar A. Engel. Importance of vibrational anharmonicity for electron-phonon coupling in molecular crystals. *Phys. Rev. B*, 105(18):L180301, May 2022.

[191] Niuchang Ouyang, Zezhu Zeng, Chen Wang, Qi Wang, and Yue Chen. Role of high-order lattice anharmonicity in the phonon thermal transport of silver halide AgX (X=Cl,Br,I). *Phys. Rev. B*, 108(17):174302, November 2023.

[192] Qingyong Ren, Mayanak K. Gupta, Min Jin, Jingxuan Ding, Jiangtao Wu, Zhiwei Chen, Siqi Lin, Oscar Fabelo, Jose Alberto Rodríguez-Velamazán, Maiko Kofu, Kenji Nakajima, Marcell Wolf, Fengfeng Zhu, Jianli Wang, Zhenxiang Cheng, Guohua Wang, Xin Tong, Yanzhong Pei, Olivier Delaire, and Jie Ma. Extreme phonon anharmonicity underpins superionic diffusion and ultralow thermal conductivity in argyrodite Ag_8SnSe_6. *Nat. Mater.*, 22(8):999–1006, August 2023.

[193] Sajan Kumar, Mayanak K. Gupta, Prabhatasree Goel, Ranjan Mittal, Sanghamitra Mukhopadhyay, Manh Duc Le, Rakesh Shukla, Srungarpu N. Achary, Avesh

K. Tyagi, and Samrath L. Chaplot. Soft anharmonic coupled vibrations of Li and SiO_4 enable Li-ion diffusion in amorphous $Li_2Si_2O_5$. *J. Mater. Chem. A*, 11(4):1712–1722, 2023.

[194] Mayanak Kumar Gupta, Sajan Kumar, Ranjan Mittal, and Samrath L. Chaplot. Soft-phonon anharmonicity, floppy modes, and Na diffusion in Na_3FY (Y= S, Se, Te): Ab initio and machine-learned molecular dynamics simulations. *Phys. Rev. B*, 106(1):014311, July 2022.

[195] Jingxuan Ding, Tyson Lanigan-Atkins, Mario Calderón-Cueva, Arnab Banerjee, Douglas L. Abernathy, Ayman Said, Alexandra Zevalkink, and Olivier Delaire. Soft anharmonic phonons and ultralow thermal conductivity in Mg_3(Sb, Bi)$_2$ thermoelectrics. *Sci. Adv.*, 7(21):eabg1449, May 2021.

[196] Yongheng Li, Junyan Liu, and Jiawang Hong. Anharmonicity-induced strong temperature-dependent thermal conductivity in $CuInX_2$ (X=Se, Te). *Phys. Rev. B*, 106(9):094317, September 2022.

[197] Tongcai Yue, Yinchang Zhao, Jun Ni, Sheng Meng, and Zhenhong Dai. Strong quartic anharmonicity, ultralow thermal conductivity, high band degeneracy and good thermoelectric performance in Na_2TlSb. *npj Comput Mater*, 9(1):1–9, February 2023.

[198] Gregory R. Medders and Francesco Paesani. Infrared and Raman Spectroscopy of Liquid Water through "First-Principles" Many-Body Molecular Dynamics. *J. Chem. Theory Comput.*, 11(3):1145–1154, March 2015.

[199] Anna Putrino and Michele Parrinello. Anharmonic Raman Spectra in High-Pressure Ice from Ab Initio Simulations. *Phys. Rev. Lett.*, 88(17):176401, April 2002.

[200] Martin Thomas, Martin Brehm, Reinhold Fligg, Peter Vöhringer, and Barbara Kirchner. Computing vibrational spectra from ab initio molecular dynamics. *Phys. Chem. Chem. Phys.*, 15(18):6608–6622, 2013.

[201] Andrea Damascelli. Probing the Electronic Structure of Complex Systems by ARPES. *Physica Scripta*, T109:61, 2004.

[202] T. Yildirim, O. Gülseren, J. W. Lynn, C. M. Brown, T. J. Udovic, Q. Huang, N. Rogado, K. A. Regan, M. A. Hayward, J. S. Slusky, T. He, M. K. Haas, P. Khalifah, K. Inumaru, and R. J. Cava. Giant Anharmonicity and Nonlinear Electron-Phonon Coupling in MgB_2: A Combined First-Principles Calculation and Neutron Scattering Study. *Phys. Rev. Lett.*, 87(3):037001, June 2001.